ROUGH CUTTING OF GERMANIUM WITH POLYCRYSTALLINE DIAMOND TOOLS

A THESIS SUBMITTED TO
THE GRADUATE SCHOOL OF NATURAL AND APPLIED SCIENCES
OF
MIDDLE EAST TECHNICAL UNIVERSITY

BY

ÇAĞLAR YERGÖK

IN PARTIAL FULFILLMENT OF THE REQUIREMENTS
FOR
THE DEGREE OF MASTER OF SCIENCE
IN
MECHANICAL ENGINEERING

JULY 2010

Approval of the thesis:

ROUGH CUTTING OF GERMANIUM WITH POLYCRYSTALLINE DIAMOND TOOLS

submitted by **ÇAĞLAR YERGÖK** in partial fulfillment of the requirements for the degree of **Master of Science in Mechanical Engineering Department, Middle East Technical University** by,

Prof. Dr. Canan Özgen ____________________
Dean, Graduate School of **Natural and Applied Sciences**

Prof. Dr. Suha Oral ____________________
Head of the Department, **Mechanical Engineering**

Prof. Dr. M. A. Sahir Arıkan ____________________
Supervisor, **Mechanical Engineering Dept., METU**

Examining Committee Members:

Prof. Dr. Mustafa İlhan Gökler ____________________
Mechanical Engineering Dept., METU

Prof. Dr. M. A. Sahir Arıkan ____________________
Mechanical Engineering Dept., METU

Prof. Dr. Levend Parnas ____________________
Mechanical Engineering Dept., METU

Asst. Prof. Dr. İlhan Konukseven ____________________
Mechanical Engineering Dept., METU

Prof. Dr. Can Çoğun ____________________
Mechanical Engineering Dept., Gazi University

Date: 06.07.2010

I hereby declare that all information in this document has been obtained and presented in accordance with academic rules and ethical conduct. I also declare that, as required by these rules and conduct, I have fully cited and referenced all material and results that are not original to this work.

Name, Last Name: Çağlar YERGÖK

Signature:

ABSTRACT

ROUGH CUTTING OF GERMANIUM WITH POLYCRYSTALLINE DIAMOND TOOLS

Yergök, Çağlar
Ms., Department of Mechanical Engineering
Supervisor: Prof. Dr. M. A. Sahir Arıkan
July 2010, 174 pages

Germanium is a brittle semi-metal, used for lenses and windows in Thermal Imaging Systems since it transmits infrared energy in the 2 µm - 12 µm wavelength range at peak. In this thesis study, polycrystalline diamond is used as cutting tool material to machine germanium. Diamond is the hardest, most abrasion-resistant material and polycrystalline diamond is produced by compacting small diamond particles under high pressure and temperature conditions, which results more homogeneous, improved strength and a durable material. However, slightly reduced hardness is obtained when compared with natural diamond.

Different from finish cutting, rough cutting, performed before finishing, is used to remove most of the work-piece material. During rough cutting, surface roughness is still an important concern, since it affects the finishing operations. Roughness of the surface of product is affected by a number of factors such as cutting speed, depth of cut, feed rate as cutting parameters, and also rake angle as tool geometry parameter.

In the thesis, the optimum cutting and tool geometry parameters are investigated by experimental studies for rough cutting of germanium with polycrystalline diamond tools. Single Point Diamond Turning Machine is used for rough cutting, and the roughness values of the optical surfaces are measured by White Light Interferometer. Experiments are designed by making use of "Full Factorial" and "Box-Behnken" design methods at different levels considering cutting parameters as cutting speed, depth of cut, feed rate and tool geometry parameter as rake angle.

Keywords: Ultra-precision Machining, Single Point Diamond Turning, Germanium, Polycrystalline Diamond Tool, Surface Roughness

ÖZ

POLİ-KRİSTAL ELMAS TAKIMLARLA GERMANYUMUN KABA İŞLENMESİ

Yergök, Çağlar
Yüksek Lisans, Makina Mühendisliği Bölümü
Tez Yöneticisi: Prof. Dr. M. A. Sahir Arıkan
Temmuz 2010, 174 sayfa

Germanyum gevrek, yarı-metal bir malzemedir, lens ve pencere şeklinde Termal Görüntüleme Sistemlerinde kullanılmaktadır. Germanyum, 2 µm - 12 µm dalga boyu aralığında yüksek kızılötesi enerji geçirgenliğine sahiptir. Bu tez çalışması sırasında germanyumun işlenmesinde, poli-kristal elmas takımlar kullanılmaktadır. Elmas, en sert, en yüksek aşınma direnci olan malzemedir. Poli-kristal elmas, küçük elmas parçacıkların yüksek basınç ve sıcaklık altında sıkıştırılmasıyla üretilir. Poli-kristal elmas doğal elmas ile karşılaştırıldığında daha homojendir, daha yüksek mukavemete sahip, dayanıklı bir malzemedir ancak sertliği daha düşüktür.

Bitiş kesiminden farklı olarak, kaba kesim en çok malzemeyi yüzeyden kaldırmak üzere yapılır. İş parçasının yüzey pürüzlülüğü, daha sonra gerçekleştirilecek yüzey işlemlerini etkilediği için, kaba kesimde de önemli bir parametredir. Ürünün yüzey pürüzlülüğü çok sayıda faktör tarafından belirlenir. Kesme parametreleri olarak kesme hızı, kesme derinliği, ilerleme hızı ve takım geometri parametresi olarak talaş açısı örnek verilebilir.

Bu tezde, poli-kristal elmas takımlarla germanyumun kaba işlenmesi için en iyi kesim ve kesici takım parametreleri deneysel çalışmalar yardımıyla araştırılmıştır. Elmas Uçlu Torna Tezgahında, poli-kristal elmas uçlarla germanyuma kaba işleme uygulanmıştır ve optik yüzeylerin pürüzlülük değerleri Beyaz Işık İnterferometre cihazında ölçülmüştür. Yapılan deneyler “Tam Faktör” ve “Box-Behnken” deneysel çalışma metotlarıyla değerlendirilmiştir. Deneysel çalışma metotları farklı seviyelerde, kesme parametreleri olarak kesme hızı, kesme derinliği, ilerleme hızı ve takım geometri parametresi olarak talaş açısı dikkate alınarak düzenlenmiştir.

Anahtar Kelimeler: Ultra Hassas İşleme, Elmas Uçlu Tornalama, Germanyum, Poli-kristal Elmas Takım, Yüzey Pürüzlülüğü

To My Family

ACKNOWLEDGEMENTS

The author wishes to express his sincere appreciation to his thesis supervisor Prof. Dr. M. A. Sahir ARIKAN for his guidance, advise, encouragements and helpful criticism throughout the throughout the research.

The author would like to thank ASELSAN, Inc. and his manager in ASELSAN, Mr. İhsan ÖZSOY, for his support and providing the facility in his study and let to use Single Point Diamond Turning Machine also by the author with encouragement. The author also has to thank to Mr. Tolga Ziya SANDER for his valuable and beneficial supports and advices in his study.

Also, the author wishes to express his sincere appreciation to technical assistance Mr. İlker SEZEN for his precious help with Single Point Diamond Turning Machine. Moreover, The author would like to thank Mr. A. E. Sinan ÖZHAN and Mrs. C. Duygu Öztürk SELÇUK for their help.

Additionally, the author would like to thank TÜBİTAK for the support during his study. Last, but certainly not least, the author wishes to offer his deepest thanks to his parent for their continuous help and understanding during the thesis study.

TABLE OF CONTENTS

LIST OF TABLES

LIST OF FIGURES

LIST OF SYMBOLS

A_l:	Absorption intensity of light
ANOVA:	Analysis of variance
α:	Clearance angle
CBN:	Cubic boron nitride
CVD:	Chemical vaporized deposition
d:	Diameter
d_c:	Critical depth of cut
doc:	Depth of cut
E:	Elastic modulus
f:	Feed rate
f_c:	Critical feed rate
ϕ:	Shear angle
γ:	Rake angle
γ_s:	Surface energy
h:	Undeformed chip thickness
H:	Hardness
I_l:	Intensity of light
K_c:	Fracture toughness
κ:	Cutting edge angle
MCD:	Mono-crystalline diamond

μ:	Mean value
n:	Rotational frequency
PCD:	Polycrystalline diamond
PV or R_z:	Peak to valley surface roughness
R:	Roughness
r:	Rake angle
r_ε:	Tool nose radius
R_a:	Average (Arithmetic) surface roughness
R_l:	Reflection intensity of light
rms or R_q:	Root mean square surface roughness
R_p:	Top peak height of surface roughness
R_v:	Bottom valley depth of surface roughness
S:	Spindle speed
σ:	Standard deviation
T_l:	Transmission intensity of light
Q:	Roughness sampling length
V_c:	Cutting speed
z(x):	Roughness curve

CHAPTER 1

INTRODUCTION

1.1 Motivation

Infrared radiation is emitted by all objects based on their temperatures. Humans and other living things or hot spots in mechanical and electrical systems are visible at cooler backgrounds with the help of thermal imaging systems which detects radiation in the infrared range of electromagnetic spectrum. There are a wide range of applications that these systems are used such as medical, predictive maintenance, security, military and other civil applications.

In medical area, thermal imaging systems are used to detect illnesses by monitoring physiological change and metabolic processes on the body. These systems are called Thermography or DITI (Digital Infrared Thermal Imaging) which measures the heat radiating from body as shown in Figure 1.1 and so, inflammation is detected. Also, in 1982 Food and Drug Administration (FDA) has approved to use thermography as a supplement to mammography to detect breast cancer [1].

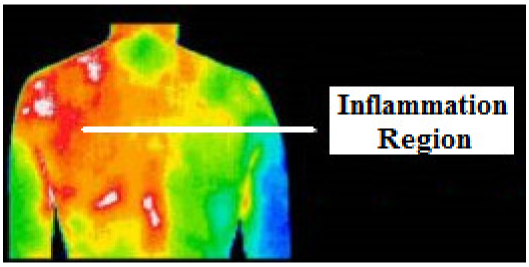

Figure 1.1 Inflammation Detection by Thermograhy [2]

In addition to illness detection, thermal imaging systems were started to be used in airports to measure body temperature of people as a result of pandemic diseases. For instance, in 2002 as a result of Severe Acute Respiratory Syndrome (SARS), elevated temperature of humans was determined by thermal imaging systems which has been accepted as an indicate of infection. Later, in 2009 same method is used to detect swine flu. The usage of thermal cameras in airports is shown in Figure 1.2.

Figure 1.2 Thermal Imaging System Usage in Airports [3]

Moreover, failure of mechanical and electrical items could be prevented with the help of thermal imaging systems. Thermal cameras are used to identify the temperature distribution in these systems and extreme heat points detected by thermal cameras are controlled since they can be a source of problem as shown in Figure 1.3. Hence, predictive maintenance with thermal cameras helps to detect these points and early intervention could be performed.

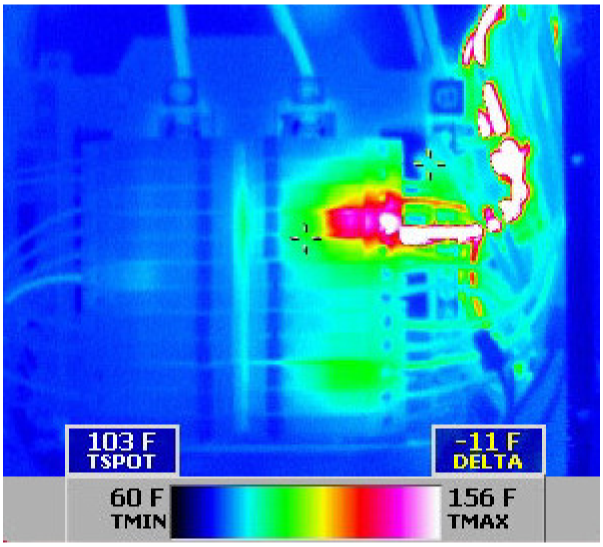

Figure 1.3 Predictive Maintenance by Thermal Imaging System [4]

In addition to these applications, thermal imaging systems are used in other civil applications such as hunting, automotive industry, etc. However, most of the usage of thermal imaging systems is related with military applications such as navigation, surveillance, searching, security, detection of enemy, etc. Some typical applications of these systems are shown in Figures 1.4, 1.5 and 1.6.

Figure 1.4 Thermal Imaging System ASIR (Courtesy of ASELSAN) [5]

Figure 1.5 Thermal Weapon Sight PYTON/BOA (Courtesy of ASELSAN) [5]

Figure 1.6 Airborne Thermal Imaging System ASELFLIR 200 (Courtesy of ASELSAN) [5]

Thermal Imaging Systems have four main parts as optics, infrared detector, signal processing unit and display. In optics, planar, spherical, aspheric and diffractive configurations made up of germanium, silicon, zinc sulfide and zinc selenide are most widely used ones because of their high transmissivity of infrared energy which is the primary target of the Thermal Imaging System to detect.

1.2 Machining, Finish and Rough Cutting

Machining is generating the required surface by relative motions between the work-piece and cutting tool [6]. Main machining processes can be specified as turning, drilling, milling, grinding, polishing, boring, reaming, shaping, planning, sawing, broaching, etc. In all these processes, cutting tool removes material from the surface of the work-piece in forms of chips. Typical orthogonal chip-removal process is shown in the Figure 1.7. The thickness of the material that will be removed on the cutting edge from the surface is called undeformed chip thickness

[6]. While the thickness of the chip, that has been already removed from machined surface, is called deformed chip thickness. They are not the same and the ratio of undeformed chip thickness to deformed chip thickness is less than unity. Moreover, the velocity of the tool during machining of work-piece surface is called cutting velocity.

There are three main angles formed between the cutting tool and the work-piece during machining, which are the rake angle, clearance angle and shear angle. Rake angle is the angle that the tool makes with the work-piece normal. As the rake angle increases in positive sense, smaller cutting forces are needed to machine work-piece surface and smaller deformations are observed on it. When machining is realized at large positive rake angles, friction and heat generation are reduced so that tool life is relatively higher. As the rake angle becomes negative, initial shock of the work-piece is compensated by the face of the tool instead of edge which prolongs the life of the tool and therefore higher speeds can be achieved [7]. Clearance angle is the angle between the cutting tool and the machined surface. Clearance angle prevents the tool from rubbing on the work-piece. During chip removal, deformation takes place within a plane called the shear plane. This plane forms an angle with the machined surface, which is called the shear angle as shown in Figure 1.7.

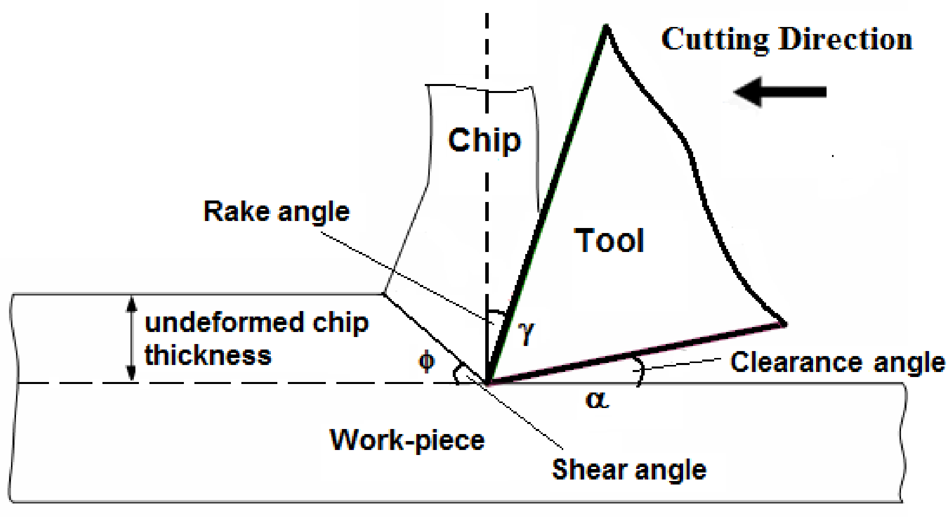

Figure 1.7 Single Point Tool Machining Process

There are two main machining modes, namely finish and rough cutting. First rough cutting operation is performed and then desired surface quality is achieved with finish cutting. The aim of rough cutting is to cut off maximum amount of material in minimum time without giving any damage to the operator, machine, work-piece or cutting tool. So, surface quality has second priority. Cutting velocity and material removal rate are high during rough cutting, resulting in subsurface damages.

In contrast, the primary goal of finish cutting operations is to obtain surfaces with high quality and parts with high dimensional accuracy. Also, material layers with subsurface damage and surface stress, generated during rough cutting are removed. Meanwhile, machining parameters such as cutting velocity, feed rate and depth of cut are given smaller values during finish cutting operations.

1.3 Ductile and Brittle Materials

Material properties affect machining conditions so, cutting and tool geometry parameters should be determined by considering the work-piece material. Ductility is the ability of material to deform under tensile force [8] and it is measured by tensile test as elongation or reduction in cross sectional area. Ductile materials generally produce continuous chips during machining and positive rake angle tools are used to machine them. Aluminum, gold and copper are typical ductile materials. The stress-strain curve of a typical ductile material is given in Figure 1.8.

Another type of material is the brittle material which has little tendency to deform before fracture when subjected to stress [9]. During machining, discontinuous chips are produced and it is more difficult to achieve high quality surfaces when compared with ductile materials. Cast iron, glass and ceramics are typical brittle materials. The stress-strain curve of a typical brittle material is also given in the Figure 1.8.

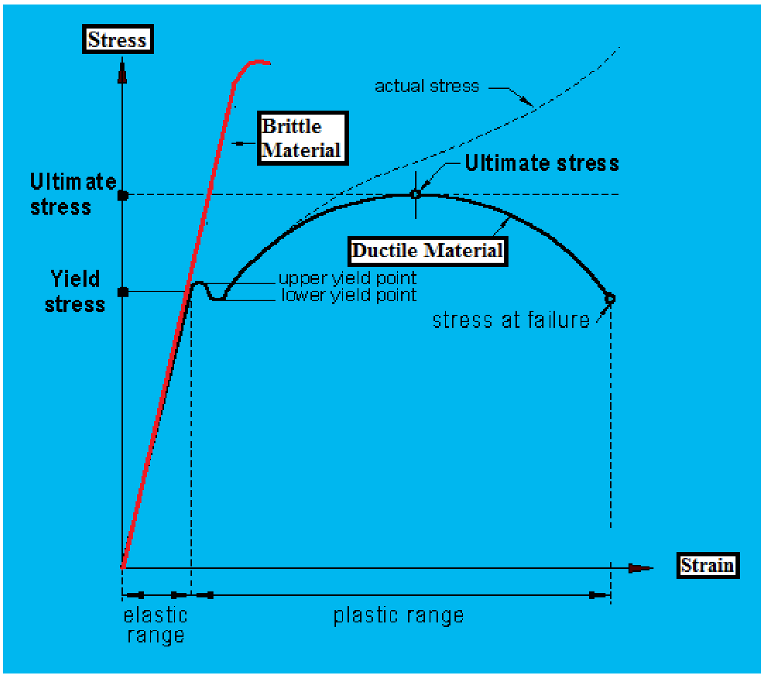

Figure 1.8 Stress-Strain Curve of Ductile and Brittle Materials (adapted from [10])

1.4 Ultra-precision Machining

The need of the growing industries increases the demand of reaching the highest dimensional accuracy values. Therefore, the limits of surface finish and dimensional tolerances are improving. Especially, the applications related with computer, optics, electronics and defense industries are vital motivations to this grow. In Figure 1.9, the growth of the machining is seen in the 20th and 21st centuries form the Taniguchi's Chart [11]. The extrapolated line of Ultra-Precision machining shows that beyond 2000s, Ultra-precision Machining will be accepted under nanometer level.

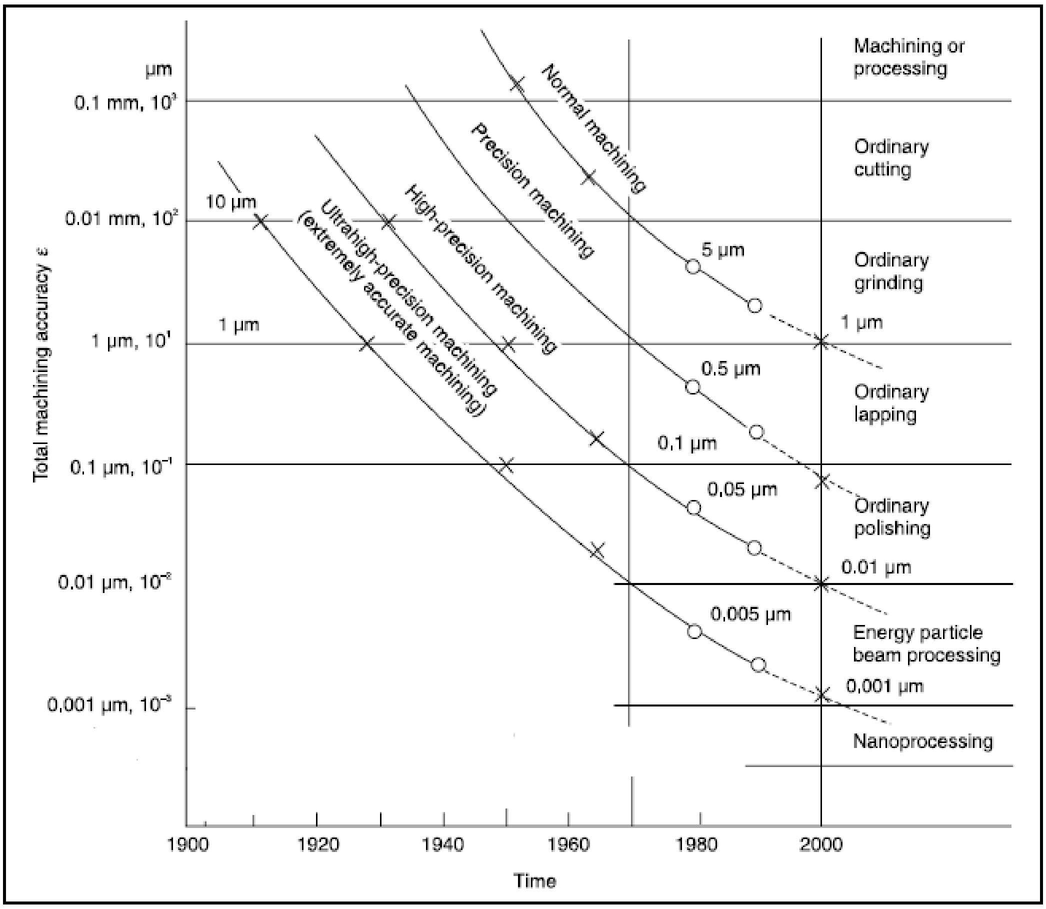

Figure 1.9 Taniguchi's Chart [11]

According to Taniguchi's Chart, there are four main machining accuracy levels. Ultrahigh-precision or Ultra-precision Machining is the highest accuracy level. Some examples of Ultra-precision Machining are lapping, polishing, single point diamond turning, elastic-emission machining and selective chemical-mechanical polishing, controlled etch machining and energy beam processes [11].

1.5 Aim and Scope of Thesis

Thermal imaging systems have an important place in military applications.

Producers of these systems have to make whole critical parts to decrease the cost and total production time. Optics are one of the vital parts of thermal imaging systems. Producing infrared optics with desired dimensional tolerance and surface quality is crucial. Therefore, related studies are continuously performed to decrease the cost considering that high production rate.

This study focuses on machining of germanium which is a widely used material in infrared optics. During rough cutting applications, generally maximum possible amount of material is removed where the surface quality has less priority. In this thesis during rough cutting of germanium, in order to decrease the cost, instead of mono-crystalline diamond tools, less expensive polycrystalline diamond tools are used in spite of their poorer properties.

During machining, single point diamond turning machine was used and the results were compared according to surface roughness. Surface roughness measurements were performed with a white light interferometer. Surface roughness depends on a number of factors such as cutting parameters, tool geometry, work-piece material properties and defects in the structure, machine vibrations, inaccuracy in the slide-ways of the spindle and tool holder, surface damage of chip and build-up edge formation [12]. It is not possible to evaluate all factors that affect surface roughness so, in this study, feed rate, depth of cut and spindle speed as cutting parameters and rake and clearance angle as tool geometry parameters were considered as main factors that affect surface roughness. For investigating the effect of defined parameters on machining of germanium design of experiment studies were performed. Design of experiment methods as 2 and 3 Level *Full Factorial Designs* and *Box-Behnken Design* were used to predict surface roughness of machined germanium surfaces by mathematical models. These models have helped to evaluate the results so, cutting and tool geometry parameters could be gathered at the best and the worst surface conditions.

Mathematical models have given the relationships between surface roughness of germanium machined by polycrystalline diamond tools and parameters which were determined as feed rate, depth of cut, spindle speed, rake and clearance angles. Surface roughness measurements have been evaluated as PV (Peak to Valley), R_a (Average Roughness) and rms (Root Mean Square) by white light interferometer. Therefore in the study, for these three evaluation methods, three different mathematical models have been found.

CHAPTER 2

LITERATURE SURVEY

2.1 Introduction

Single point diamond turning or ultra-precision diamond turning, one of the machining applications of ultra-precision machining, had been a result of demand in advance science and technology for energy, computer, electronics and defense applications. Actually, ultra-precision machining has been referred to highest dimensional accuracy and surface roughness that can be achieved at that time by Taniguchi [11].

Historically, diamond machining started by the development of numerically controlled, polar coordinate aspheric generating machine for the production of high quality camera lenses. That generating machine was developed by Taylor & Robson in 1950s. For about the same time period, a cartesian coordinate machine that uses a high speed diamond burr to generate aspheric curve on glass surfaces was developed by Bell and Howell [13].

Then, in late 1970s, one more innovative development was attained by Lawrance Livermore National Laboratory in California. Diamond turning machine, having a vertical spindle shown in Figure 2.1, was developed by that laboratory to manufacture large optics. Large optical components like mirrors for telescopes were machined using diamond tools and surface roughness values like 4 nm were achieved without subsequent polishing [11].

Further years, the development of diamond turning continued to satisfy the needs in various applications and today diamond tools with less than hundred nanometer waviness are used to machine optical surfaces. As a result of this, diamond turning achieves to produce optical components with sub-micrometer level dimensional accuracy and surface roughness in nanometer level and it is also used to machine infrared optical materials such as germanium and silicon.

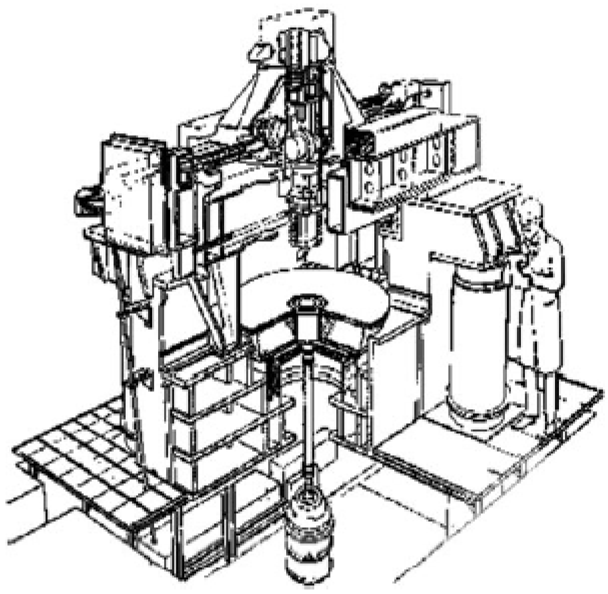

Figure 2.1 Diamond Turning Machine in Lawrance Livermore National Laboratory [11]

Studies were presented on ultra-precision diamond turning of optical materials as silicon and germanium, having similar crystal structures called diamond cubic crystal structure. In 1988, Blake and Scattergood had presented their study in which they machined silicon and germanium with a diamond turning machine. In that study, optical surfaces having nanometer level surface roughness values had been produced. During machining, the depth of cut was 0.12 to 125 μm, feed was 1.25 to 10 μm/min and rake and clearance angles of the tool were 0^o to -30^o and 6^o to 16^o respectively [14]. In 1988, in the study of Smith et al., germanium was also machined by Bryant Symon Diamond Turning Machine and according to that study, flat surfaces with 5.5 nm R_a roughness were obtained [15].

Furthermore, in 1989 Blake and Scattergood [16] had made a study about ductile regime machining of germanium and silicon. In that study, with a parallel axis ultra-precision lathe shown in Figure 2.2, the surfaces of germanium and silicon have been machined. Then, the results of that study were shared in 1990 and according to that, 0.8 nm rms roughness was achieved on diamond turned germanium surfaces, while surface finish values were 3 to 4 nm rms for silicon. The reason of the difference was mentioned as the increased tool wear. During machining, the depth of cut, feed rate and cutting speed were 0.12-125 μm, 1.25-10 μm/rev and 0.84-8.2 m/s respectively.

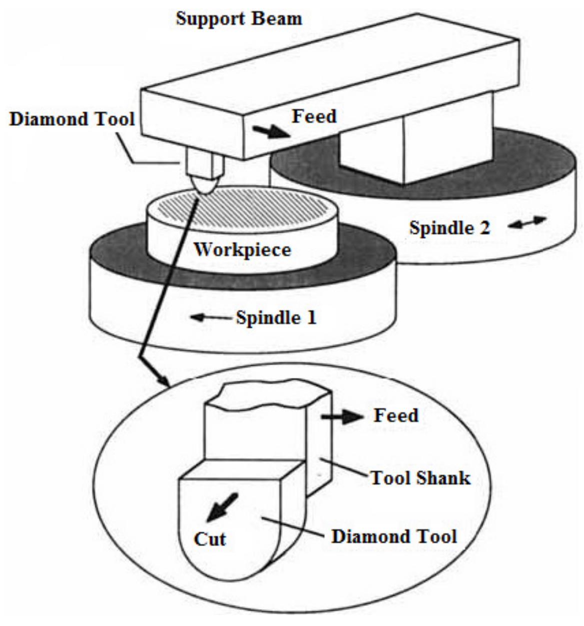

Figure 2.2 Parallel Axis Ultra-precision Diamond Turning Lathe [16]

Then, Yu and Yan obtained mirror surface with 6 nm Ra roughness on single crystal germanium with (111) plane in 1994. In their study, rake angle of the tool was -25^{o}, clearance angle was 6^{o} and nose radius was 0.8 mm. The feed rate, depth of cut and spindle speed were 1 mm/min, 2 mm and 1000 RPM, respectively as the machining conditions [17].

In 1997, Fang machined optical surfaces on silicon by diamond turning using Precitech Optimum 2800. During machining silicon surfaces, a mirror surface with 5.9 nm R_a roughness has been obtained with 4 mm/min feed rate, 1 mm depth of cut and 80 mm/min cutting speed. Moreover, optical surface with 1 nm R_a roughness has been obtained when feed rate was decreased to 0.4 mm/min [18]. In 2002, Chao machined silicon wafers with (111) and (100) orientations by using Rank Pnuemo ASG-2500 machine. Diamond tools with different geometries were used for facing operation. The machining conditions were such that cutting speed was from near 0 to 150 m/min, feed rate was up to 9 mm/min and spindle speed was around 1200 RPM. At the end of the study, optical surfaces with 5 nm R_a surface roughness were achieved [19].

Later, Jasinenevicius et. al [20] made a study about diamond turning of silicon with (100) planes in 2004. In that study, the depth of cut was determined as 5 μm and the surfaces were machined with 2.5 and 8 μm/min feed rates. The cutting tool had 0.65 mm nose radius, -25^{o} rake and 12^{o} clearance angle. In results, the surface roughness had been developed as 1.6 nm R_a for cutting with 2.5 μm/min feed rate and the material removal was fully ductile. When the feed rate has been increased to 8 μm/min, micro-cracks formed on the machined surface and brittle mode prevailed the machining process so, the surface roughness raised up to 91.25 nm R_a.

In 2008, Çalı [18] has made an experimental study about diamond turning of optical grade silicon. In that study, the surface roughness values of machined surfaces were evaluated with changing machining conditions. The machining conditions such as cutting speed, depth of cut and feed rate were determined as parameters and with 2 level full factorial design, a mathematical model was constructed between the surface roughness and these three parameters. In results, it was mentioned that 1 nm R_a roughness could be attained at machining conditions such as 90 m/min cutting speed, 1 μm depth of cut and 1 mm/min feed rate with a mono-crystalline diamond tool having -15^o rake angle.

2.2 Brittle and Ductile Modes of Machining

Germanium and silicon are brittle materials so, dislocation motion for these materials are difficult. During the machining of brittle materials like as ductile materials, low surface roughness has to be attained to produce precise surfaces. Brittle materials can be machined in ductile mode, brittle mode or in transition between them. If brittle mode of machining prevails, micro-cracks form on the surface and surface roughness increases.

Jasinevicius et. al [20] performed a study on machining of mono-crystalline silicon with (111) orientation by single point diamond turning machine. The cutting applications were performed under different conditions that result the ductile and brittle mode machining of silicon. When depth of cut was 5 μm, tool has 0.65 mm nose radius and -25^o rake angle, ductile mode machining resulted 1.6 nm R_a roughness where feed rate was 2.5 μm/rev. When the feed rate of the process was increased to 8 μm/rev, brittle mode of machining prevailed. So, the roughness of the machined surface increased up to 91.25 nm R_a and micro-cracks formed. Figure 2.3 shows the difference between the machined surfaces formed as a result of ductile and brittle mode machining. Three dimensional views were obtained by atomic force microscope. In (a), the surface is smooth and the cut grooves formed by tool can be seen. In that machining, surface was formed as a result of ductile mode machining. While, in (b), machined surface was prevailed by brittle mode machining. Surface was not smooth, pitting can be seen all over the surface and micro-cracks were formed on it.

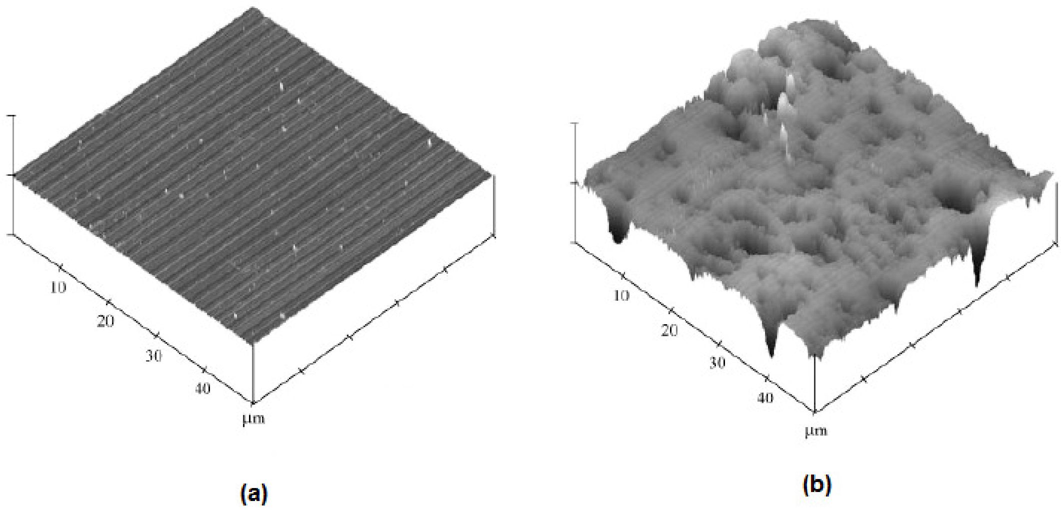

Figure 2.3 Diamond Turned Silicon Surfaces [20]

Yan et. al [21] studied the wear of diamond tools while machining single crystal silicon by ultra-precision diamond turning. Instead of round nosed tool, a straight nosed diamond tool was used with 6^{o} clearance angle. However, during machining, tool has been adjusted to achieve -20^{o} rake angle so, clearance angle became 26^{o}. The depth of cut was 1 to 2 µm and feed rate was 10 µm/rev during cutting applications. From the study, it was shown that machining altered from ductile mode to brittle mode as a result of tool wear. Figure 2.4 shows the R_z or PV surface roughness with cutting distance. As shown from the graph, until 3.81 km cutting distance, roughness was almost constant, and after 5.08 km roughness started to increase rapidly. This indicated that after 5.08 km cutting distance, brittle mode machining prevailed to cutting.

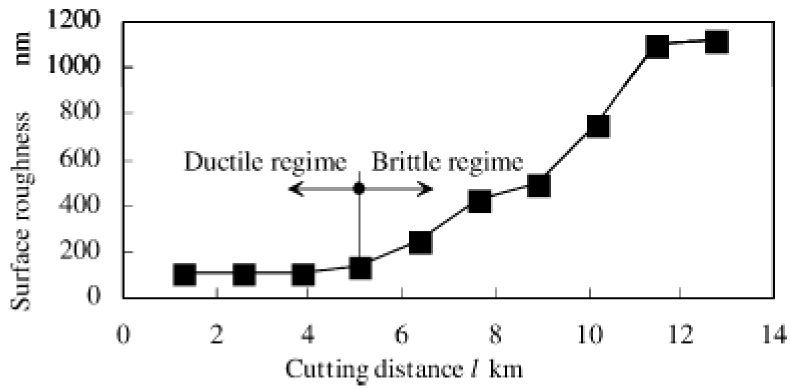

Figure 2.4 R_z or PV Surface Roughness Change with Cutting Distance [21]

Atkins and Mai [22] have made studies about ductile and brittle modes of deformation on brittle materials. It was seen that in the same material, both ductile and brittle modes of machining can be realized and the transition between them can be controlled by the machining conditions. Therefore, a brittle material can be machined in ductile mode by changing the machining conditions.

2.3 Critical Chip Thickness

Ductile mode machining is preferred to brittle mode since smoother surfaces can be machined by ductile mode. Shaw has been working on ultra-precision diamond grinding of brittle materials and in that study, the surface and subsurface damages formed during machining of brittle materials disappears at a critical value of undeformed chip thickness h [23]. This critical value has been termed as critical chip thickness d_c. Figure 2.5 shows micro cracks and surface damage formed at the region where undeformed chip thickness is above d_c.

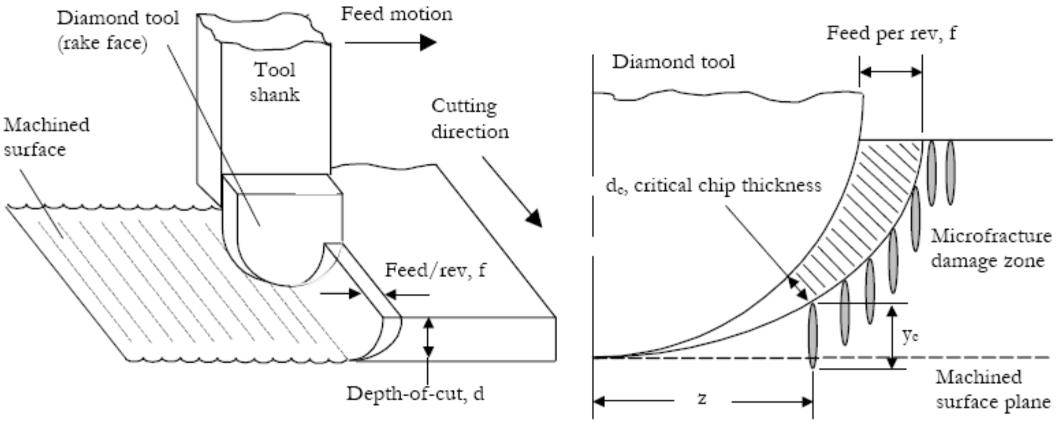

Figure 2.5 Critical Chip Thickness [24]

The critical chip thickness changes from material to material and below a limit, plastic deformation prevails instead of brittle fracture to material removal process. The machining of brittle materials by plastic deformation is termed ductile regime or mode as mentioned by O'Connor [23] during the study in which fly cutting experiments were made on silicon. So, as mentioned in that study when undeformed chip thickness was above the critical limit, fracture damage was left by tool as a result of brittle mode machining.

Blake [24] was one of the pioneers in diamond turning of semiconductors with Scattergood, have showed that germanium and silicon could be diamond turned and in their study, critical depth of cut phrase was used instead of critical chip thickness. In that study, an equation was defined for critical depth of cut as given in (2.1). A similar expression was mentioned by Tidwell that shows the direct proportionality between d_c and $(K_c/H)^2$ [25].

$$d = d_c \alpha (\frac{E}{H}) * (\frac{K_c}{H})^2 \tag{2.1}$$

Where;

d_c: Critical Depth of Cut

H: Hardness

K_c: Fracture Toughness = $2\gamma_s E$, γ_s Surface Energy

E: Elastic Modulus

Moreover, Blake [24] also mentioned about some possible effects that increase critical depth of cut. First, temperature rise in the zone of deformation was given since elevated temperature reduces the stress and thus hardness reduces and that results increase in critical depth of cut. Second, a high compressive hydrostatic stress forms in front of the cutting tool during machining like indenter so this inhibits crack formation. Also, Patten [25] emphasized that this high compressive hydrostatic stress results a phase transition from semiconducting to metallic on germanium and silicon and metallic phase of these materials behaves like ductile materials so during machining of these, plastic deformation occurs. Therefore, high compressive hydrostatic stress increases critical depth of cut. Third, specific tool geometry of single point diamond turning was given as an effect that increases critical depth of cut, since tool edge generates dislocation motion on parallel planes, needed for plastic deformation. Moreover, cutting fluid used in machining process can increase critical depth of cut, since fluid environment, formed by cutting fluid, may increase tendency for plastic flow at the near surface of the machined material. Lastly, phase transition was given as an effect that increases critical depth of cut. The reason was previously mentioned that metallic phase of materials germanium and silicon behaves like ductile materials.

Blake [24] also notified the influence of depth of cut and feed rate on critical chip thickness. Figure 2.6 shows the chip formed during machining and its change in shape with increased depth of cut at (a) and with increased feed rate at (b). Therefore, as depth of cut increases, the maximum undeformed chip thickness increases and a wider chip is formed. However, the relationship between chip thickness and depth that micro-cracks formed doesn't change. While, as feed rate increases, maximum undeformed chip thickness increases and the thickness of the chip ascends along all width. So, the critical chip thickness formed at higher depth from the uncut surface of part and thus pitting could be formed on the machined surface.

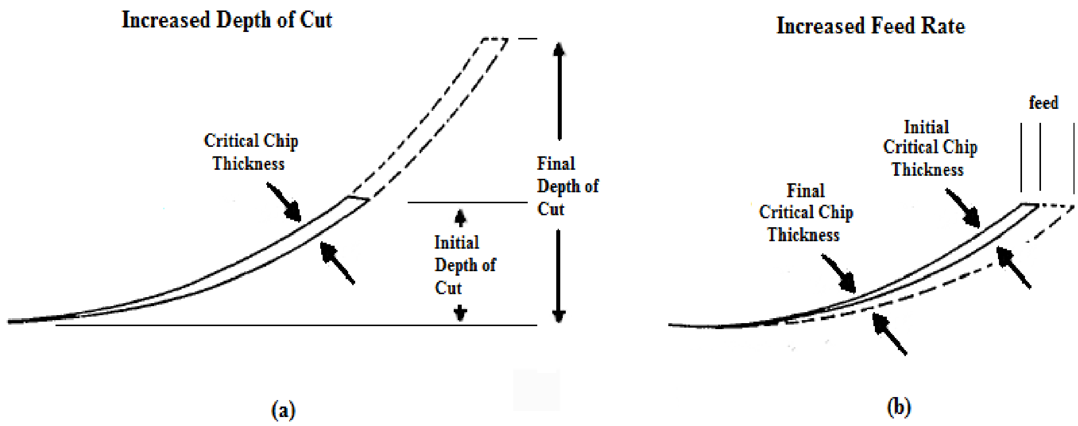

Figure 2.6 Shape Difference of Chip with Increased Depth of Cut and Feed Rate [24]

In another study, Ohta et. al [26] had machined single crystal germanium lenses with (111) planes by mono-crystalline diamond tools, having -25^{o} rake angle and 10^{o} clearance angle and the cuttings were performed at different feed rates and spindle speeds and also by different tools with different tool nose radius. In results as indicated, after tool passed the machined region, the residual tensile stress could cause crack initiation when the undeformed chip thickness was high enough.

Patten et. al [27] also presented a study about ductile machining of normally brittle materials such as silicon and silicon nitride. In that study, the key parameter for ductile machining of brittle materials was given as chip cross section (critical chip thickness or critical depth of cut). This critical chip thickness was given as a combination of feed, depth of cut, tool nose radius and rake angle of the tool. Large negative rake angle tool was emphasized to be advantageous to machine materials such as silicon, germanium and silicon nitride by the authors.

Jan et. al [28] presented a study about ductile regime turning of silicon wafers. However, in this study instead of round-nosed tool, a straight-nosed diamond tools was preferred since, the thickness of the chip, shown in Figure 2.7, doesn't change throughout the chip unlike the chip formed by round-nosed tool as shown in Figure 2.6. So, the cutting application became uniform.

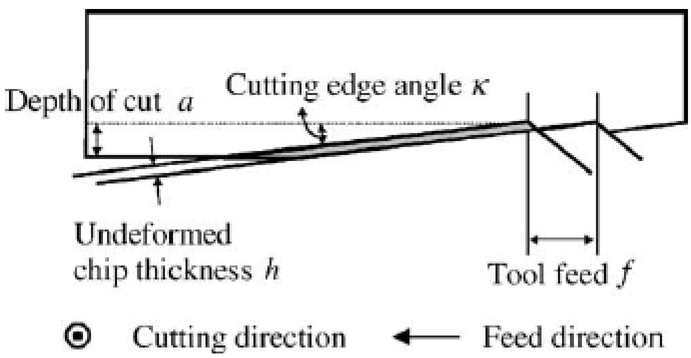

Figure 2.7 Schematic View of Machining with Straight-nosed Tool [21]

In that study, undeformed chip thickness h was determined by tool feed rate f and cutting edge angle κ as described in Equation (2.2).

$$h = f * \sin \kappa \tag{2.2}$$

So, critical chip thickness d_c became directly proportional with critical feed f_c, feed at the ductile to brittle transition. Also, cutting edge angle κ is inversely proportional to critical chip thickness d_c. The equation between, critical chip thickness, critical feed and cutting edge angle was given in Equation (2.3). In addition to this information, in that study it was mentioned that the surface of the silicon wafer was machined by a diamond tool with -40^{o} rake angle while feed was increasing continuously and the Nomarski micrograph of the machined surface was given. As shown in Figure 2.8, feed was increased from left to right and the critical feed f_c could be determined by observing pitting on the machined surface.

$$f_c = d_c / Sin\kappa \tag{2.3}$$

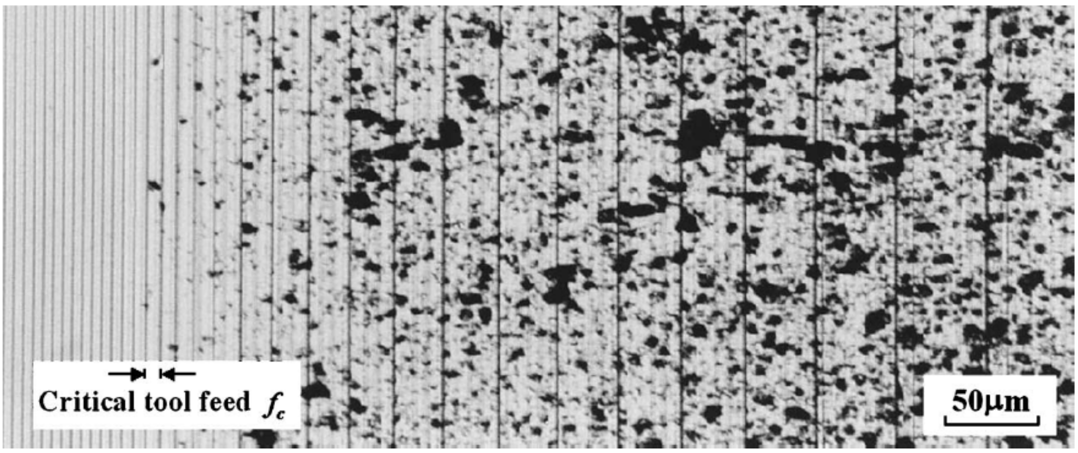

Figure 2.8 Nomarski Micrograph of Machined Surface of Silicon [28]

In that study, Yan et. al [28] also mentioned the relationship between critical chip thickness and rake angle of the tool. Two different silicon wafers with (111) and (100) orientations were machined and this experiment was made with different tools having rake angles such as 0^{o}, -20^{o} and -40^{o}. The effect of rake angle to critical chip thickness was given in Figure 2.9. So, it can be concluded that large negative rake angle increases the critical chip thickness.

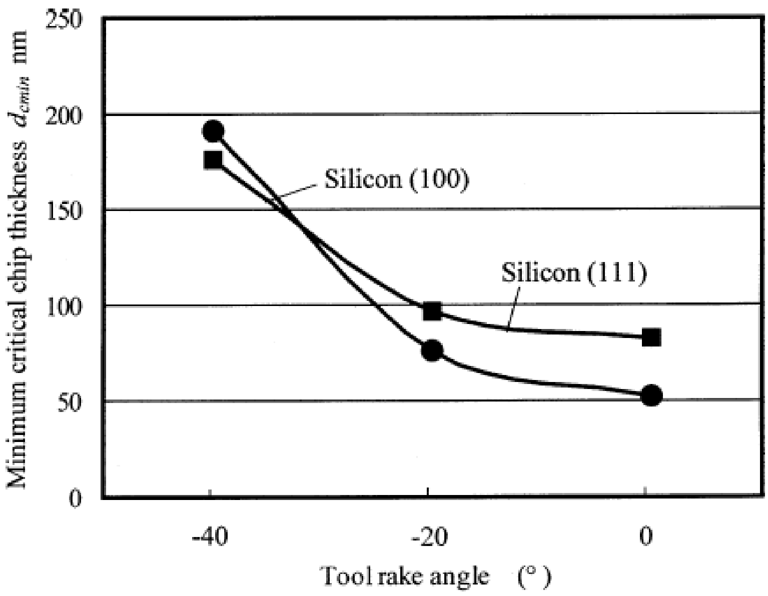

Figure 2.9 The Effect of Rake Angle on Critical Chip Thickness [28]

2.4 High Pressure Phase Transformation

Similar to silicon, germanium has diamond cubic crystal structure at atmospheric conditions up to melting point. This form of germanium is called semiconducting phase. Semiconducting phase of germanium transforms to metallic phase at high pressures. Under quasi-hydrostatic conditions, semiconducting to metallic phase with β-tin structure transformation starts at about 10 GPa pressure [29].

During the machining by single point diamond turning, the diamond tool acts as an indenter. This indenter results high hydrostatic pressure under the tip of the tool as shown in Figure 2.10 so, the phase transformation develops. This is called high pressure phase transformation. The studies about the phase change of semiconductors such as silicon and germanium is not new. In the study of Shimomura et. al [30], silicon and germanium have been studied and it was shown that amorphous silicon reversibly transforms to metallic phase with β-tin structure under high pressure. This transition is called Mott Transition.

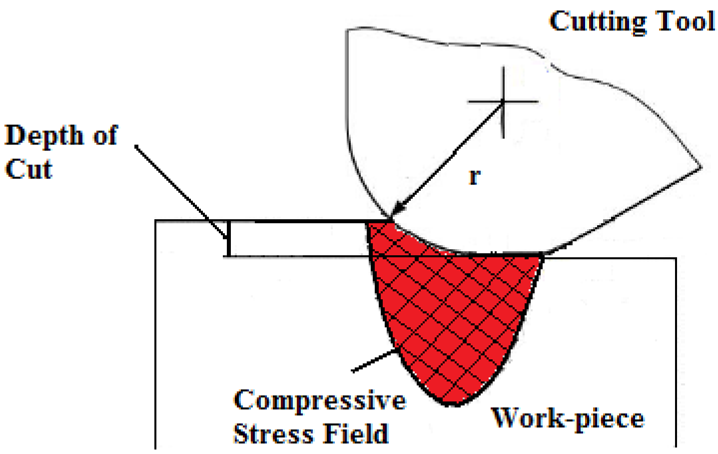

Figure 2.10 Compressive Stress Field at the Tip of the Tool

Furthermore, as indicated by Morris et.al [31], the high pressure over 10 GPa under cutting tool causes phase transformation for semiconductors like silicon and germanium from diamond cubic to metallic phase and the ductility of metallic phase provides the necessary plasticity to semiconductors for ductile mode machining. So, in some studies this phase transformation was also expressed as brittle to ductile transition. However, after the pressure releases as tool move away, metallic phase transforms to amorphous phase and this amorphous phase constitutes chips. In addition to chip, near surface of the machined work-piece transforms to amorphous phase shown by molecular dynamic simulations made by Boercker et. al [31]. Figure 2.11 shows the transformation and back transformation of phase of chip, near surface of machined work-piece and semiconducting material.

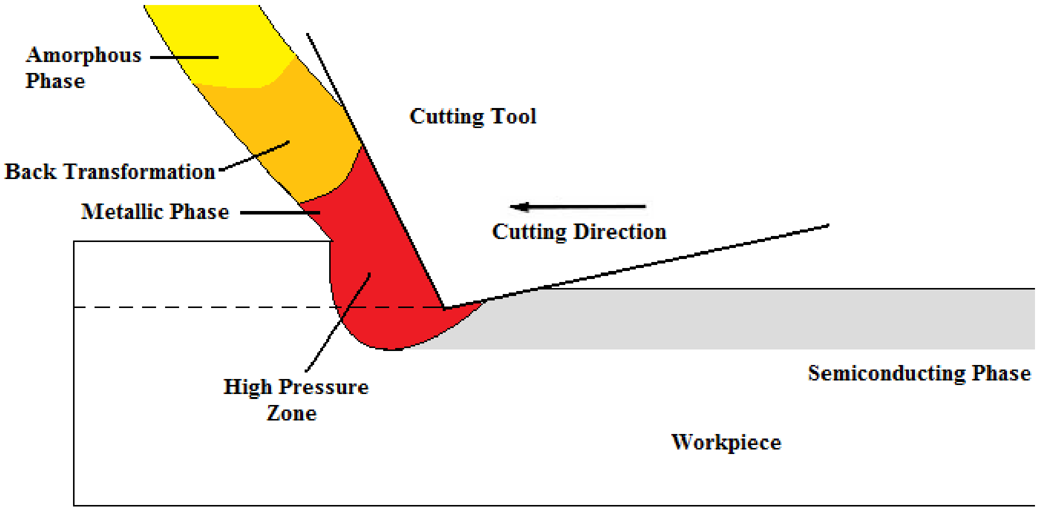

Figure 2.11 Phase Transformation and Back Transformation During Machining (adapted from [31])

Minomura and Drickamer [14] concluded that pressure-induced semiconductor-to-metal transition (Mott Transition) resulted a decrease at the electrical resistivity of germanium and silicon. In that study, it was mentioned that the electrical resistivity of germanium dropped five orders of magnitude to the metallic level at compression near 12 GPa. The same phenomena developed at about 20 GPa for silicon. Moreover, according to the study of Gridneva et. al, [14] the metallic layer of semiconductor, formed at high pressure under cutting tool, returned back to semiconducting phase when tool moved away and pressure fell down and the conductivity of silicon came back to semiconducting level when pressure removed. Also, in that study it was also mentioned that the metallic layer of work-piece under the indenter was about 50 nm thick.

In another study, Clarke et. al [14] approached a similar result with Morris et. al and Boercker et. al, silicon and germanium transformed from diamond cubic to β-tin under indentation because of the hydrostatic pressure and after unloading thermal energy has been insufficient to form re-crystallization to diamond cubic structure, therefore a meta-stable amorphous phase generated at regions where phase transformation had occurred. Thus, the phase transformations of silicon and germanium under indenter or cutting tool depends on the hydrostatic pressure and thermal energy formed between work-piece and tool. Table 2.1 shows the high pressure phases of silicon which gives idea about phase transformation of semiconductors during loading and unloading of hydrostatic pressure [14].

Table 2.1 High Pressure Phases for Silicon [11]

Designation	Structure	Pressure Region
I	Diamond Cubic	0-11
I'	Amorphous	11-0
II	Body Centered Tetragonal (β-Tin)	11-15
III	Body Centered Cubic (BC-8)	10-0
IV	Primitive Hexagonal	14-40
V	Hexagonal Closed-Packed	40

In addition to these studies, Morris et. al [25] expressed the semiconducting to metallic phase transformation of silicon, germanium, diamond and tin under high pressure corresponding to material hardness. The ductility of metallic phase of these materials was also mentioned and the plastic deformation was stated to develop during machining of germanium and silicon. However, high pressure had to be ensured to establish this transition. According to that study, the pressure to obtain phase transformation was 9 GPa for germanium, while 12 to 15 GPa for silicon.

Furthermore, during the studies of phase transformations, the thickness of amorphous layer, left on the machined surface after the tool or indenter had passed away, was discussed. The results of the amorphous layer have been changing from study to study. Puttick et. al mentioned 100-400 nm amorphous layer in grinded silicon with (111) plane, while Shibata found 100 and 500 nm thickness for 2 and 3 μm depth of cuts respectively for diamond turned silicon with (100) plane [32]. Whereas, the thickness of the amorphous layer for silicon was defined as 20 to 250 nm thick after diamond machining processes such as grinding, polishing and diamond turning in the study of Jasinevicius [33].

2.5 Machining by Polycrystalline Diamond (PCD) Tool

In the literature, studies have been shared related with the machining of various materials by polycrystalline diamond tools. For instance, in the study of Zhong et. al [34], aluminum based metal matrix composites reinforced by either silicon carbide or aluminum oxide were machined by diamond turning and grinding and comparison of these two machining methods have been compared. Aluminum based metal matrix composites reinforce with ceramic particles are widely used in automobile, aerospace and military industries because of their good damping properties, low density, high elastic modulus, high thermal conductivity, high specific strength and high wear resistance. However, these materials are machined with high cost due to their poor machinability [34,35].

In the study of Zhong et. al [34], rough cutting was performed by PCD tools and then Mono-crystalline Diamond (MCD) tools were used for finish cutting with constant depth of cuts in the range of 0 to 1.6 μm and cutting speed of 10 to 200 m/min in a single point diamond turning machine. As a result of the study, 17 nm R_a roughness was obtained during the machining of silicon carbide reinforced metal matrix composite and 0.2 μm was determined as critical depth of cut.

In another study, Sreejith [36] has realized machining of silicon nitride, having a hardness value of 18 GPa, by polycrystalline diamond tool with high speed lathe. Machining forces were analyzed with respect to cutting speed varied from 100 to 300 m/min, depth of cut from 5 to 25 μm and rake angle from 0 to -20°. In the study, ductile machining of silicon nitride was achieved by considering that cutting force was higher than thrust force by a considerable margin which indicated that material removal was in ductile manner without fracture. Also, it was mentioned that as depth of cut increased or more negative rake angle tools were used, machining forces were increased.

Moreover, Davim et. al [37] investigated machinability of glass fiber reinforced plastic in turning process by polycrystalline diamond and cemented carbide tools K15 in CNC lathe. Surface roughness and specific cutting pressure were defined as two machinability criteria of this composite material. PCD tool had 6^o rake angle and 11^o clearance angle. For the experiment, cutting speed, varied from 100 to 400 m/min, and feed rate, varied from 0.05 to 0.2 mm/rev, were defined as parameters and it was mentioned that R_a roughness increased with feed rate and decreased with cutting velocity for PCD tool. During the study, smaller roughness values were obtained by PCD tool and the obtained R_a roughness values were between 1.22 and 2.91 μm for PCD tool while they were between 1.22 and 4.01 for K15 carbide tool. After the machining experiments, analysis of variance study has been performed in the study to determine influence of parameters and feed rate was stated as highest physical and statistical influence parameter on surface roughness and specific cutting pressure while the effect of cutting velocity was mentioned as practically insignificant.

In a different study, Petropoulos et. al [38] have made statistical studies on peek composite which is replacing aluminum in some cases because of its performance at high temperatures. This material was machined by polycrystalline diamond and K15 cemented carbide tools. During the machining, 7^o rake angle and 11^o clearance angle tool have been used and 2 mm was determined as depth of cut. While cutting speed and rake angle were stated as two machining parameters. Cutting speed and feed rate were varied 50 to 200 mm/min and 0.05 to 0.2 mm/rev respectively. As a result of the study, it was specified that PCD tool provided smaller roughness values especially for feed rate less than 0.1 mm/rev. During the evaluation of parameters, analysis of variance study was used to determine the influence of parameters and as mentioned feed rate exerted strong effect on surface roughness while the effect of cutting speed was insignificant when compared by feed rate.

In the study of Morgan et. al [39], polycrystalline diamond tool was used to machine ultra-low expansion (ULE) glass Corning 7972 in three axis micro electro discharge machine. The machining parameters were 100 nm depth of cut, 1 μm/s feed rate and 3000 RPM spindle speed. As a result of study, 0.3 nm R_a roughness was obtained by PCD tool during which depth of cut was below brittle to ductile transition so only ductile cutting marks were formed. However, it must be specified that PCD tool had been shaped in three stages before the machining of ULE glass. First of tool, with wire electro discharge machining PCD tool was shaped to 1 mm cylindrical tool. After that, diameter of PCD reduced to 50 μm by wire electro discharge grinding and finally, geometric accuracy of cutting surface was obtained by micro electro discharge machining.

In another study, Sreejith et. al [40] have evaluated the performance of polycrystalline diamond tool during the face turning of carbon/phenolic ablative composite with CNC lathe. In the experimental study, spindle speed was defined as 6000 RPM and other cutting parameters as cutting speed, feed rate and depth of cut were varied between 100 to 400 m/min, 25 to 100 μm/rev and 1 to 1.5 mm, respectively. PCD tool used in the study had 0^o rake angle, 5^o clearance angle and 0.8 mm nose radius. As a result of study, it was mentioned that 300 mm/min was critical speed considering that specific cutting pressure and temperature increased in an accelerated speed. Also, as shown from the results as feed rate increased, temperature was also increased in a parallel attitude.

In the study of Nabhani [41], an annealed titanium alloy with Knoop Hardness of 4.17 GPa has been machined by polycrystalline diamond, cubic boron nitride and coated carbide (KC 850) tools in a CNC Lathe. Machining parameters were 75 m/min surface speed, 0.25 mm/rev feed rate and 1 mm depth of cut and all machining applications were performed without cutting fluid. In the experiment, wear of tools during machining was observed, and it was seen that adherent interfacial layer was formed on the top of rake face of PCD tool but not a significant crater has developed and this caused a difference between PCD tool and the other tools used in experiments. Therefore, it was stated that PCD tool was not failed even after 30 minutes machining while coated carbide tool and cubic boron nitride have failed in 9 and 11 minutes respectively. Moreover, in this study surface finish results of machined titanium alloy have been shared and as shown from Figure 2.12, PCD tool cut off the surface with lowest roughness and its performance remained same for a longer time when compared with others.

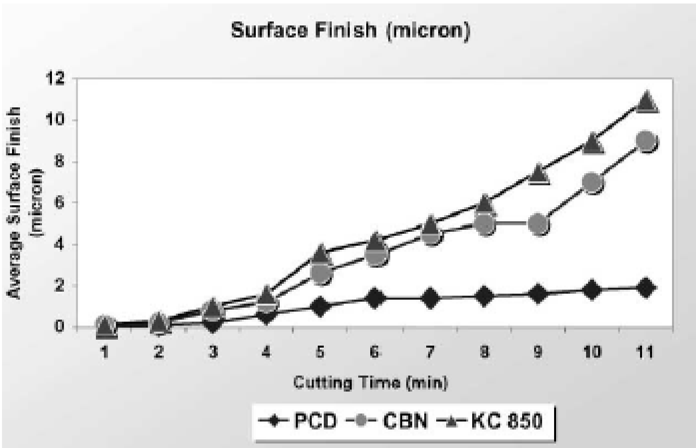

Figure 2.12 Surface Finish of Titanium Alloy with Cutting Time [41]

In another study, Cheng et. al [42] have machined tungsten carbide and silicon wafer by micro polycrystalline diamond ball end mill. In the study, ductile mode machining has been investigated with good surface finish and no pitting. During the machining, 0.1 mm diameter, -60^{o} rake angle PCD tool has been used and to define the ductile mode of machining, a scanning electron microscope (SEM) pictures have been used. First of all, tungsten carbide has been machined with 1 μm depth of cut and 0.1 μm/tooth feed rate and according to evaluation up to SEM picture, it was mentioned that ductile mode of machining has been achieved because no pitting or crack had developed at surface. Then, silicon wafer has been machined with first 0.1 μm depth of cut and 0.05 μm/tooth feed rate and then 0.5 μm depth of cut and 0.1 μm/tooth feed rate with cutting fluid in both cases. Therefore, from the SEM pictures, it was seen that no pitting or cracks formed in first case however, brittle mode of machining prevailed in the second machining applied on silicon wafer.

In the study of Belmonte et. al [43], sintered tungsten carbide-cobalt work-pieces had been machined by cubic boron nitride, chemical vapor deposition diamond and polycrystalline diamond tools. The machining application performed at fixed cutting conditions as 15 m/min cutting speed, 0.2 mm depth of cut and 0.03 mm/rev feed rate. In the study, one of the drawback of PCD tools were mentioned as the cobalt binder used during the sintering of crystal particles and this was specified as the reason of worse performance of PCD tool when compared with Chemical Vapor Deposition (CVD) diamond tool for the machining of tungsten carbide-cobalt work-piece. The softening effect of cobalt has been mentioned for PCD tools in the study. This was expected because work-piece material has also cobalt content so, material-tool adhesion occurred during machining. Therefore this resulted a bad machining performance for PCD tool. Thus, better surface roughness results have been obtained by cubic boron nitride and chemical vapor deposition diamond tools.

2.6 Rainbow Appearance of Diamond Turned Surfaces

Rainbow appearance, shown in Figure 2.13, is formed as a result of light scatter under white light. There are a number of reasons to this rainbow appearance. One of the reasons for this phenomenon is the chip left in the tool cutting edge during machining. Therefore, coolant performance for chip removal is an important process to prevent that diffraction. Moreover, work-piece material structure may result in this appearance. Materials with small crystals result a fine grid in surface finish and if the grid has right dimensions, diffraction is seen on the machined surface. The machining conditions such as cutting speed and feed rate have to be changed. Machined materials can cause this diffraction by impurities in them. Materials, that have iron and chromium impurity, have rainbow appearance after machined by diamond turning. Moreover, imbalance or bad clamping of insert, tool or tool holder can cause vibration that damage cutting edge of the diamond tool and may cause rainbow effect [44].

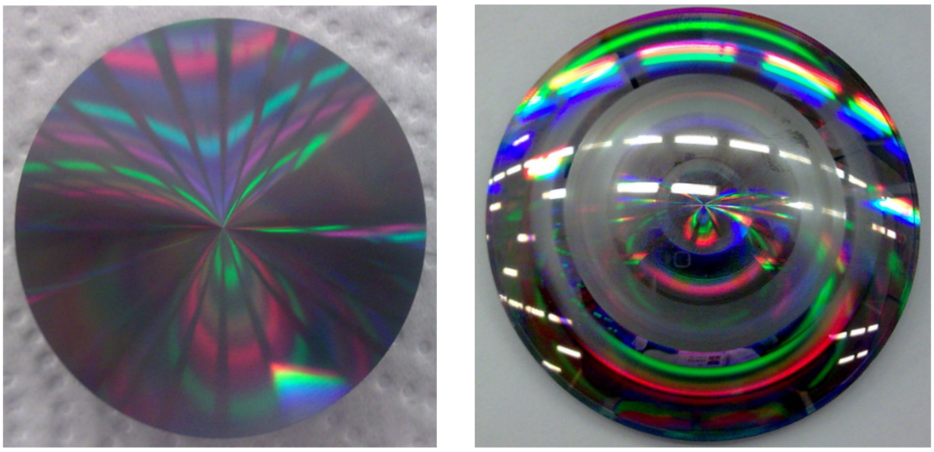

Figure 2.13 Rainbow Appearance of Diamond Turned Germanium Surfaces

The rainbow effect has been also investigated in different industries. For instance, machining of contact lenses, ultra-precision lathing systems are used. These systems are used to machine toric contact lenses. During machining of some contact lens materials, chemical erosion has been developed between silicone, contact lens material and carbon atoms of diamond so, tool get worn. Then, rainbow effect was seen on the surface which has been machined by worn tool [45].

Sohn et. al [46] made a study to develop a model to simulate the effects of vibration on surface finish of diamond turned materials. Therefore, in this study surface roughness of machined plated copper was tried to be decreased and a mathematical model between roughness and feed rate and tool nose radius was investigated. As a result of the study, vibration was mentioned to cause impact on optical surfaces by resulting coherent scatter. So, this scatter produced rainbow appearance on the diamond turned surfaces.

In another study, Blake [24] had mentioned about rainbow effect. In that study, rainbow effect was given as a result of ridges formed at the surface of machined silicon since ridges scatter white light. According to that study, ridges within the machining grooves were formed by nicks in the tool edge which is a result of tool wear.

CHAPTER 3

EXPERIMENTAL COMPONENTS

3.1 Introduction

This chapter includes the basic components of the thesis study. Single Point Diamond Turning as machining process, Germanium as optical material and Diamond Tool as cutting tool are introduced in this chapter. Also, 2 and 3 Level Full Factorial Design and Box-Behnken Design methods, used to determine the mathematical relationship between surface roughness of machined germanium surfaces and machining and tool geometry parameters, are mentioned. At the end, surface roughness and its measurement methods are expressed.

3.2 Single Point Diamond Turning

Single Point Diamond Turning is a typical ultra-precision machining process and this process is also used to machine infrared optical materials such as germanium, silicon, zinc selenide, zinc sulfide, gallium arsenide, calcium fluoride, arsenic trisulfide, amtir and some chalcogenide glasses [47]. Single Point Diamond Turing Machines are used to machine aspheric, diffractive and freeform surfaces as well as flat and spherical ones. Generating and polishing is another way of machining infrared lens materials, however with that way, diffractive and freeform surfaces could not be machined. So, Single Point Diamond Turing departs from other production ways with its ability to produce variety of configurations with the same tool and machine setup. However, mass production of planar, spherical and aspheric surfaces can be achieved in a longer time especially for large outer diameter optics when compared with generating and polishing.

As well as infrared optical materials, single point diamond turning is used to machine high-precision reflective surfaces, used as a mirror in optical systems. Some aluminum alloys are used as reflective materials in thermal imaging systems and they could be machined by diamond turning machines. Therefore, in addition to infrared optical materials, a variety of materials such as nickel, copper, aluminum, tin, zinc and magnesium could be machined by single point diamond turning machines. During the machining of infrared optical materials, submicron level dimensional accuracy or form tolerance, also nanometer level or even under 1 nanometer surface roughness values can be achieved by single point diamond turning.

The production of high-precision optical surfaces by single point diamond turning machines depends on a number of factors. Vibration isolation is an important concern for machining. So, there are three main precautions for vibration damping. At first, precision air bearing spindle allows vibration free rotation of chuck and work-piece. Second, these machines or lathes are built with high-quality granite block, having micrometer level surface finish quality. This gives rigidity and vibration damping to the machine. Third, granite block is placed on air suspension system, keeping the block horizontal and this system isolates the machine from vibrations [48].

Before the machining, optical part is attached to the chuck using negative air pressure or vacuum as shown in Figure 3.1 and usually centered manually using a dial indicator. The position of the work-piece is also critical to manufacture precise surfaces on optical parts. After the part is placed correctly, the rotating work-piece is machined with a diamond tool as shown on Figure 3.1. The properties of diamond tools will be mentioned in Section 3.4.

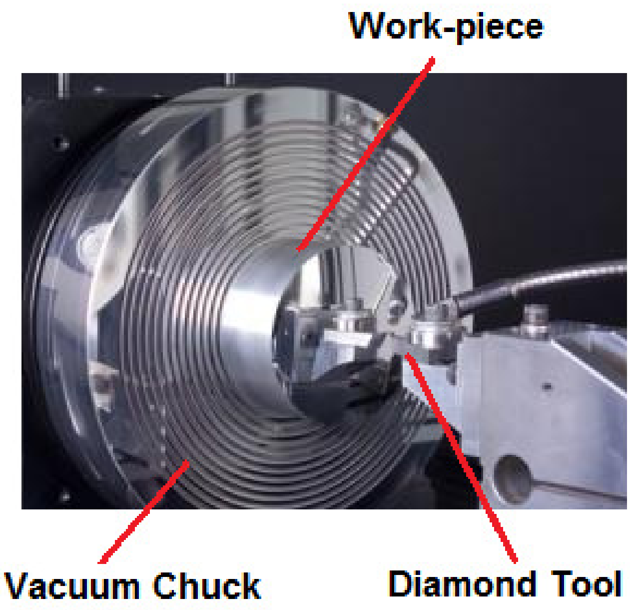

Figure 3.1 Diamond Tool and Machining [49]

In this thesis study, as a single point diamond turning machine, Precitech Freeform 700U four-axis diamond turning machine was used as shown on Figure 3.2 and technical specifications of the machine are given in Appendix A. These four axes are shown on Figure 3.3. During machining with this machine, there are three main machining configurations. During the machining of optical surfaces when B, X and Z axes are all active together, smoother surfaces can be machined because waviness of the cutter does not result unwanted form tolerance on the surface of work-piece since during this machining, always the same point of tool cuts off the surface. Also, C, X and Z axes can be controlled together to machine freeform surfaces. Moreover, only two axes as X and Z axes can be controlled together to machine flat, spherical, aspheric or diffractive optical surfaces. In this study, for rough cutting of germanium, two axes as X and Z were controlled which is sufficient for machining of flat and spherical surfaces.

Figure 3.2 Single Point Diamond Turning Machine [50]

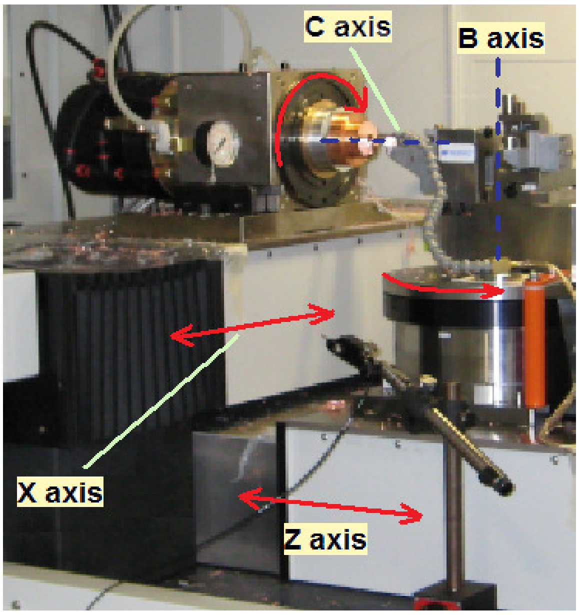

Figure 3.3 Four Axes of Diamond Turning Machine

3.3 Optical Materials in Thermal Imaging Systems and Germanium

In Thermal Imaging Systems, germanium and silicon are the most widely used materials because of their transmission of infrared energy. These materials are both IV A Group elements and they have a lot of similar properties. Germanium and silicon are both silvery gray, brittle and semi-metallic materials. Their crystal structure is called diamond cubic crystal structure like as diamond. In the Figure 3.4, diamond cubic crystal structure is shown. Atoms in this structure are tetrahedrally coordinated with their neighbor atoms [24]. The bonds are covalent and form fixed angles with each other.

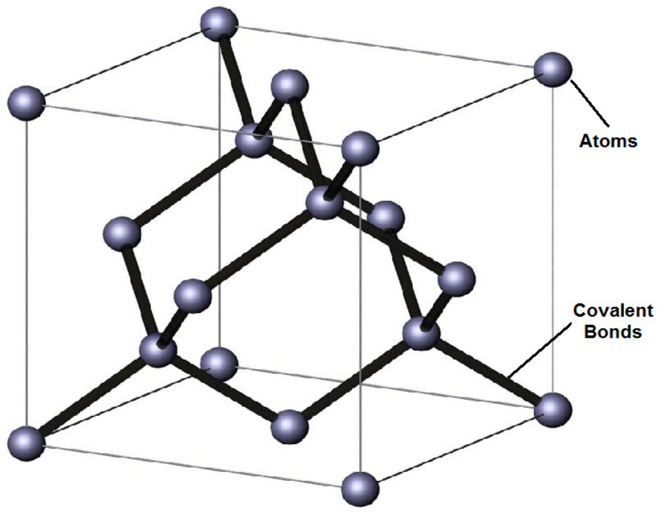

Figure 3.4 Diamond Cubic Crystal Structure [23]

Optical germanium wafers are grown by Czochralski Crystal Growth Method. In this study, germanium wafers with {111} planes were used which were grown by Czochralski Method and the cleavage plane is (111), while the predominant slip system is {111}[110] for germanium. The tensile and shear stresses act on cleavage and slipping planes that change during machining and the behavior of these planes determines whether brittle fracture or plastic deformation will occur [51].

Germanium is a semiconductor and it was discovered in 1886 by a German chemist. In Table 3.1, some basic properties of germanium can be seen. In Earth, germanium is obtained from zinc, sulfide ores and coal. However, the average germanium content in deposits are too low, generally range is from 0.001% to 0.1%. Germanium is used in a wide range of applications. In 2008, for about 25% of germanium has been consumed for infrared optics. Also, a bit less than 25% has been used for fiber optic systems, for about 30% has been used for polymerization catalysts, for about 10% has been used for solar electric applications and 10% for others [52].

Table 3.1 Properties of Germanium [53]

Properties	**Unit**	**Germanium**
Standard Atomic Weight	g/mol	72.64
Density	g/cm^3 (300 K)	53.234
Melting Point	^oC	937.4
Boiling Point	^oC	2830
Specific Heat Capacity	$J/mol{*}^oC$	0.3219
Modulus of Elasticity	GPa	130
Shear Modulus	GPa	50
Poisson's Ratio	-	0.3
Knoop Hardness	N/mm^2	7644

The transmissivity of germanium is high and homogeneous within 2 to 12 μm wavelength infrared band in electromagnetic spectrum as shown in Figure 3.5 and 3.6 and because of this property, it is widely used in thermal imaging systems. Moreover, germanium is highly preferred material in infrared optics because of its prominent chemical stability and corrosion resistance [52]. Also, it is more easily machined when compared with equivalent infrared optical materials such as silicon, that decreases the machining cost.

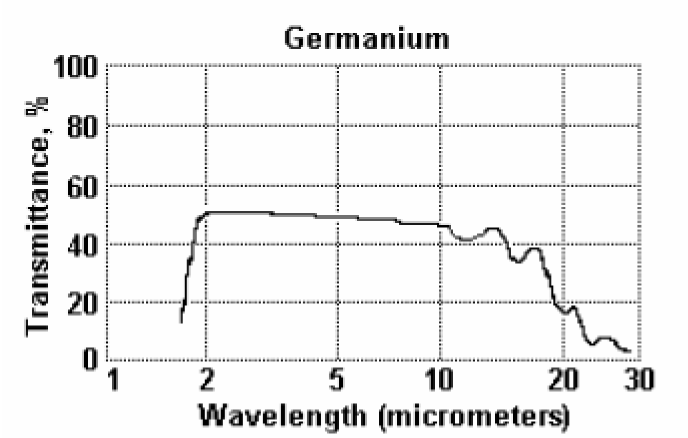

Figure 3.5 Transmittance of Germanium in Electromagnetic Spectrum [18]

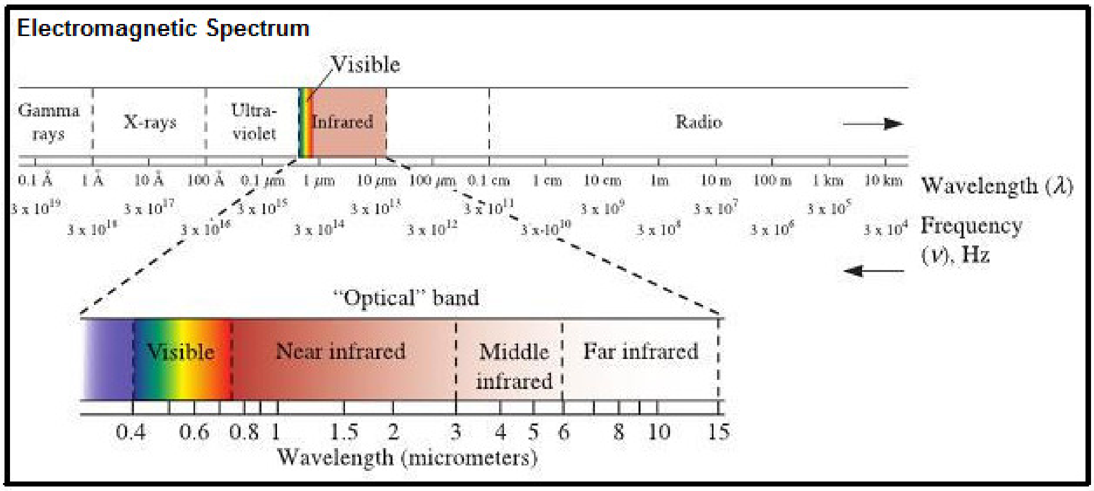

Figure 3.6 The Electromagnetic Spectrum [54]

During the manufacture of germanium lenses, there are two main methods as Czochralski Crystal Growth Method and Casting. Cast germanium is always polycrystalline. However, when compared, single crystals are preferable to multi crystals because of their uniformity, lower absorption and absence of impurities [55]. Single crystal germanium bar is obtained by using Czochralski Crystal Growth Method. Then, this bar is sliced up to germanium discs and by further machining, discs are machined to windows or lenses [52].

In this thesis, flat surface of 40 mm diameter mono-crystalline germanium disc and convex lens surface of 62 mm outer diameter and 5 mm center thickness mono-crystalline germanium lens have been machined. These parts are shown in Figures 3.7 and 3.8.

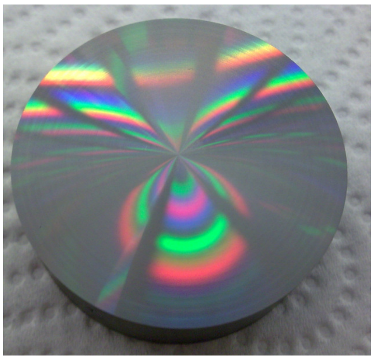

Figure 3.7 Mono-crystalline Germanium Disk

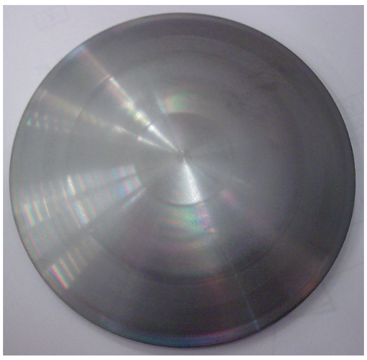

Figure 3.8 Mono-crystalline Germanium Lens

3.4 Diamond Tools

Natural diamond is used as cutting tool material since 1940s [11]. Diamond tools are widely used in machining since they produce very smooth surfaces. For the production of optical materials, diamond is a good choice because of its high hardness, stiffness, toughness, wear resistance and long tool life. Diamond tools are divided into three groups as mono-crystalline (single crystal) diamond, polycrystalline diamond and synthetic diamond tools.

Generally, diamond tools are considered as finish cutting tools since they produce smooth surfaces. For the production with high material removal rates, different kinds of tools are better to use since diamond tools are generally more expensive than the others. For diamond machining, machining parameters are generally different than other machining methods. For diamond turning operations, depth of cut varies in micrometer range while, feed rates are generally no more than a few hundreds of mm/min.

However, all materials cannot be machined by diamond tools like materials with unpaired d-shell electrons. Some examples to these materials are chromium, cobalt, iron, manganese, molybdenum, niobium, rhenium, rhodium, ruthenium, tantalum, tungsten, uranium, vanadium. Materials with no unpaired d-shell electrons are machined by diamond tools. Some examples to these materials are aluminum, beryllium, copper, germanium, gold, indium, lead, magnesium, nickel, plutonium, silicon, silver, tin, zinc [56].

Natural diamond develops slowly at temperatures from 900 to 1,300°C and pressures from 40 to 60 atm. Nowadays, mono-crystalline or single crystal diamond tools are most widely used cutting tools for ultra-precision diamond turning. Quality of diamond, crystal orientation and cutting edge geometry defines the diamond tool performance. (110) plane of diamond is in the direction of the maximum cutting force so in that plane, diamond is brazed onto a tool holder [11]. Figure 3.10 shows typical diamond tool.

Figure 3.9 Mono-crystalline Diamond Tools [44] (Contour Fine Tooling)

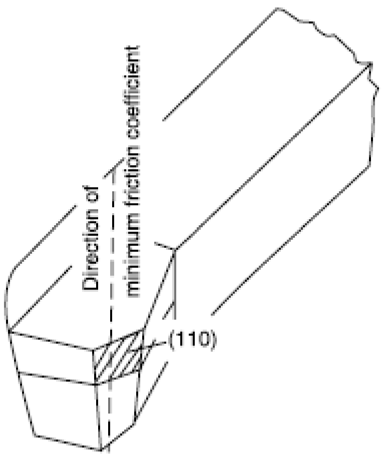

Figure 3.10 Typical Diamond Tool [11]

Polycrystalline diamond tools are formed from high number of individual diamond particles under high temperature about 3000 K and pressure about 125 kbars. When compared with mono-crystalline diamond tools, PCD tools have reduced hardness however they are more homogeneous and cheaper with improved strength and durability [6]. Polycrystalline diamond tools are generally used for machining of aluminum alloys, metal matrix composites, titanium alloys and plastics. Therefore, these tools are generally used to machine parts used in automotive, aerospace, electronics and optical industries.

Figure 3.11 Insert of Polycrystalline Diamond Tool (Kennametal Inc.)

Synthetic diamonds are also used for machining, formed by heating graphite under high temperature about 3000 K and high pressure about 125 kbars with nickel as a catalyst. These tools are generally used for machining moulds, laser mirrors, magneto-optical discs, optical lenses. Therefore, they have important applications in industrial fields such as the electronic and optical technology [11]. A typical synthetic diamond tool is shown in Figure 3.12.

Figure 3.12 Synthetic Diamond Tool [57] (Technodiamant Inc.)

The machining application in single point diamond turning is generally performed by mono-crystalline diamond tools. Mono-crystalline diamond tools can be divided into two main groups as controlled waviness and non-controlled waviness. The radius waviness is the deviation from true circle and it is measured from peak to valley as shown in Figure 3.13 [44]. As the waviness of the tool decrease, surfaces with better dimensional tolerance can be machined since the waviness of the tool results imperfections on the machined surface. The controlled waviness tools have nanometer level waviness values and they are more expensive than non-controlled waviness tools. Therefore, during rough cutting, non-controlled waviness tools are preferred to decrease the cost of manufacturing.

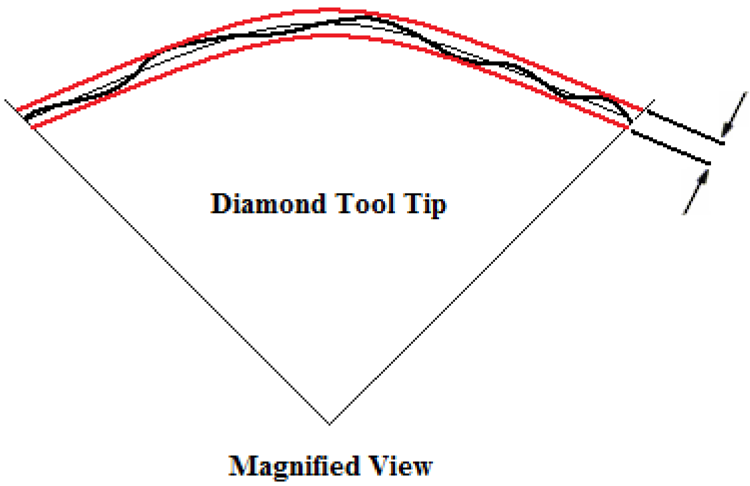

Figure 3.13 Waviness of the Mono-crystalline Diamond Tool

In this study, instead of non-controlled waviness tools, lower price polycrystalline diamond tools and inserts' usage were investigated to machine germanium by diamond turning. In addition to their price, polycrystalline diamond tools have one more critical advantage, they can be more easily provided from the market by much more number of suppliers.

3.5 Design of Experiment

Design of experiment is a method used to determine relationship between the output of the process and input parameters or variables. Design of experiment needs to gather information between output and input variables hence, experimental studies are performed. However, during the experiment, number of runs should be minimum to decrease the cost. Therefore, the choice of the method of experimental design is vital not to make high number of runs.

The choice of an experimental design depends on the objectives of the experiment and the number of factors or parameters to be investigated. Comparative, Screening and Response Surface are three main objectives of experimental designs. In Comparative Objective, the main purpose is to make conclusion about one priori important parameter. In Screening Objective, the main purpose is to represent the few important main effects from less important ones. In Response Surface Objective, the main purpose is to estimate optimal process settings and weak points. Also, Response Surface Objective makes process more insensitive against external and non-controllable influences [58]. Main design of experiment methods are given in Table 3.2.

Table 3.2 Design of Experiment Methods [58]

Number of Factors	Comparative Objective	Screening Objective	Response Surface Objective
1	1 Factor Completely Randomized Design	–	–
2 to 4	Randomized Block Design	Full or Fractional Factorial	Central Composite or Box-Behnken
5 or more	Randomized Block Design	Fractional Factorial or Plackett-Burman	Screen First to Reduce Number of Factors

In this thesis study, three different design of experiment methods were used to predict surface roughness of machined surfaces. So, the best and the worst surface conditions have been planned to be gathered for further operations. As a result of these methods, mathematical models were obtained which gave the relationships between surface roughness of germanium, machined by polycrystalline diamond tools and factors or parameters as feed rate, depth of cut, spindle speed, rake and clearance angles.

In this study, first of all Two-level Full Factorial Design, a screening objective design of experiment method, is performed on two different configurations as flat and spherical surfaces. Four parameters have been selected as spindle speed, depth of cut, feed rate and rake angle to define mathematical relationship between these parameters and surface roughness. Then, for comparison with Two-level Full Factorial Design, Three-level Full Factorial Design was performed on flat surface by considering three parameters as spindle speed, depth of cut and feed rate. At the end, for using a different objective, Box-Behnken Experimental Design Method has been applied on flat surface. After completing all these experimental studies, analysis of variance (ANOVA) application was performed to discern the importance of parameters that were investigated.

In Full Factorials Designs, the experiment is performed by a number of runs, defined according to level of the design and number of parameters. Two-level Full Factorial Design with three parameters has 8 runs. The runs are performed at highest and lowest values of the parameters, given in Figure 3.14. The highest points of parameters are shown as (+) and the lowest points of parameters are shown as (-). In Two-level Full Factorial Design with four parameters, one more parameter is added to the experimental study and 16 runs are performed. The runs for Two-level Full Factorial Design with four parameters are given in Table 3.3.

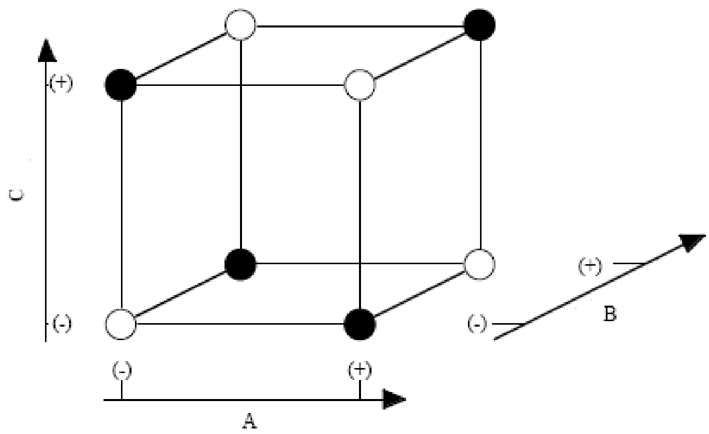

Figure 3.14 Graphical Representation of Two-level Full Factorial Design with Three Parameters [59]

Table 3.3 Runs for Two-level Full Factorial Design with Four Parameters

	Parameters			
Run	A	B	C	D
1	-	-	-	-
2	+	-	-	-
3	-	+	-	-
4	+	+	-	-
5	-	-	+	-
6	+	-	+	-
7	-	+	+	-
8	+	+	+	-
9	-	-	-	+
10	+	-	-	+
11	-	+	-	+
12	+	+	-	+
13	-	-	+	+
14	+	-	+	+
15	-	+	+	+
16	+	+	+	+

Three-level Full Factorial Design with three parameters has 27 runs. The runs are performed at the highest and the lowest values and at the middle point of the parameters, as given in Figure 3.15. The highest points of parameters are shown as (+), the lowest points of parameters are shown as (-) and middle points as (0). The runs for Three-level Full Factorial Design with three parameters are given in Table 3.4.

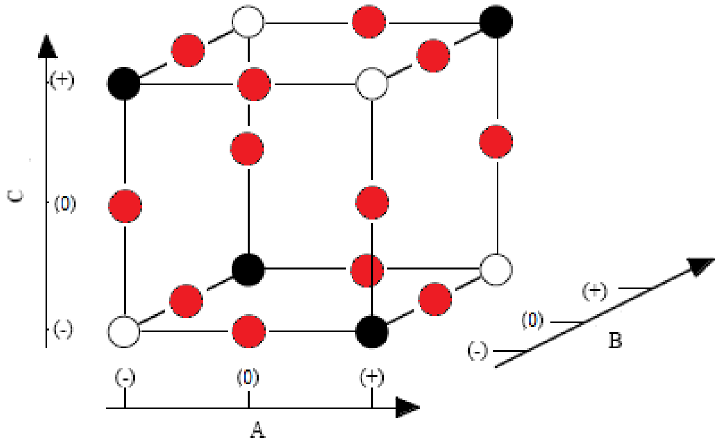

Figure 3.15 Graphical Representation of Three-level Full Factorial Design with Three Parameters

Table 3.4 Runs for Three-level Full Factorial Design with Three Parameters

	Parameters		
Run	A	B	C
1	0	+	+
2	+	0	-
3	0	0	+
4	+	0	+
5	+	-	0
6	0	-	+
7	-	+	-
8	-	-	+
9	-	+	+
10	0	-	0
11	-	0	+
12	-	+	0
13	0	0	-
14	-	-	0

	Parameters		
Run	A	B	C
15	0	+	-
16	0	-	-
17	+	-	-
18	-	0	-
19	-	-	-
20	0	0	0
21	0	+	0
22	+	+	+
23	+	+	-
24	-	0	0
25	+	+	0
26	+	-	+
27	+	0	0

Box-Behnken Design with three parameters has 13 runs. The runs are performed at the middle point of at least one parameter and the highest, the lowest values and the middle point of remaining two parameters, given in Figure 3.16. The highest points of parameters are shown as (+), the lowest points of parameters are shown as (-) and middle points as (0). The runs for Box-Behnken Design with three parameters are given in Table 3.5.

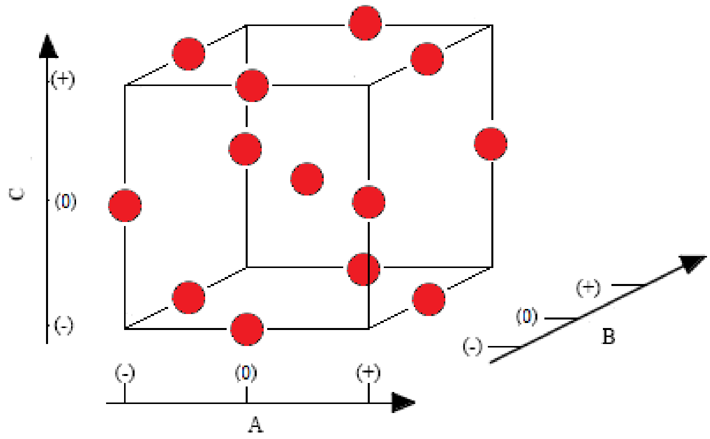

Figure 3.16 Graphical Representation of Box-Behnken Design with Three Parameters

Table 3.5 Runs for Box-Behnken Design with Three Parameters

	Parameters		
Run	A	B	C
1	-	-	0
2	-	+	0
3	+	-	0
4	+	+	0
5	0	-	-
6	0	-	+
7	0	+	-
8	0	+	+
9	-	0	-
10	+	0	-
11	-	0	+
12	+	0	+
13	0	0	0

Moreover, in this thesis the result of the mathematical models were used to make (ANOVA) studies and the critical parameters for the relationship between roughness and cutting and tool parameters were defined. The result of analysis of variance (ANOVA) studies of all the three designs as Two-level Full Factorial Design with four parameters, Three-level Full Factorial Design with three parameters and Box-Behnken Design with three parameters will be given in Chapter 5.

3.6 Surface Roughness

During the machining of work-pieces, no matter what kind of material, tool or machining processes are used, irregularities are formed on the cutting surface. The combination of imperfections on the surface are called surface texture. Excluding the flaws and lays, short and long spaced repeating irregularities forms surface profile. Short spaced repeating irregularities are called roughness and long spaced repeating irregularities are called waviness [60]. Figure 3.17 shows the texture, roughness and waviness of the machined surface.

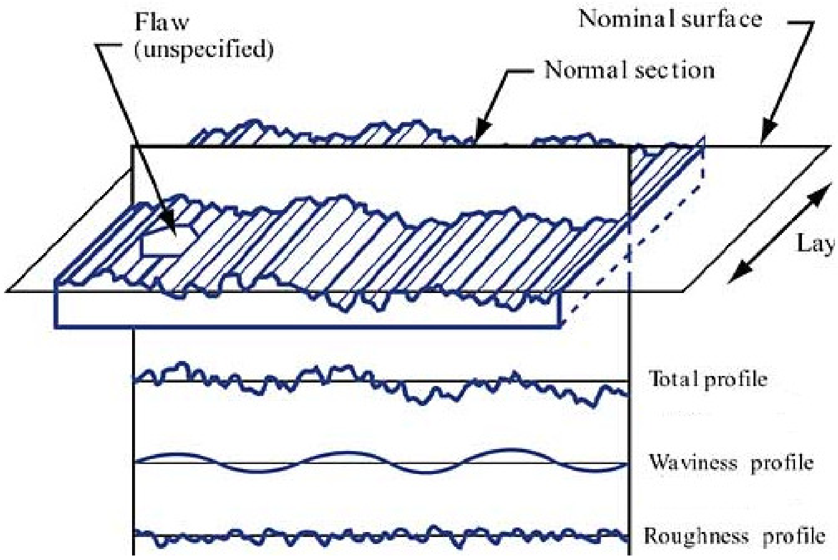

Figure 3.17 Surface Texture and Profile [61]

Surface roughness is composed of two components as ideal surface roughness and natural surface roughness [6]. Ideal surface roughness is the result of geometry of tool and feed, while natural surface roughness is the result of irregularities in the machining processes and these irregularities are generally the consequence of work-piece material properties and defects in the structure, machine vibrations, inaccuracy in the slide ways of the spindle and tool holder, surface damage of chip and build-up edge formation [7]. Ideal surface roughness is the best surface that can be achieved and Figure 3.18 shows the scheme of ideal surface roughness for a tool with rounded corner. For that tool, ideal surface roughness is expressed with following formulation (3.1) [6].

$$R_a = 0.0321 * f^2 / r_\varepsilon \tag{3.1}$$

Where;

R_a: Arithmetic Surface Roughness

f: Feed

r_ε: Tool Nose Radius

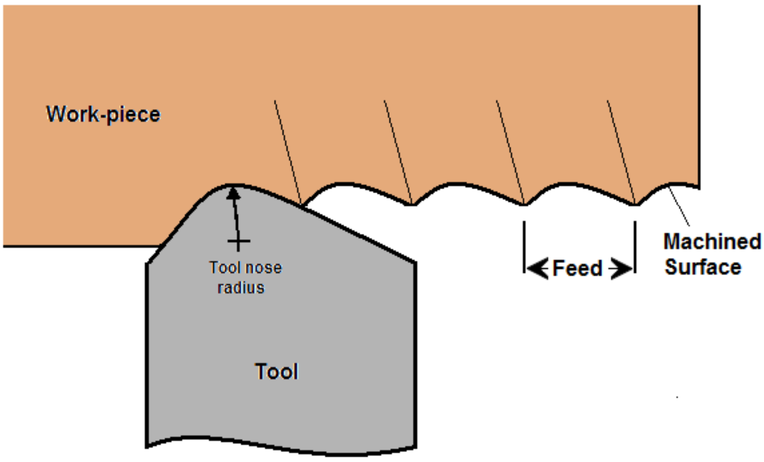

Figure 3.18 Ideal Surface Roughness for a Tool with Rounded Corner (adapted from [6])

However, normally it is impossible to reach ideal surface roughness, so tool geometry and feed are not the only parameters that affect the surface roughness. So, most of the actual roughness of the machined surfaces are as a result of natural surface roughness [6].

Surface measurements are performed by different methods. Contact and non-contact measurement methods are two main groups. Contact measurement methods are attained by stylus, which moves laterally across the machined surface for a specified distance with a specified contact force and the vertical motion of the probe defines the form of the surface. The radius of spherical stylus is up to micrometer range. However, in spite of that small tip radius of the stylus, it modifies results a bit as, it rounds sharp ends, smooth peaks and valleys. Also, it decreases or increases length at steps since it could not enter features smaller than its radius [62]. Some profilometers use contact measurement method to measure profile of the surface. One example to this is profilometer, used in this study and results will be shared in Section 6.3. Typical profilometers can measure small vertical irregularities up to nanometer range. Figure 3.19 shows a typical contact measurement and errors of it.

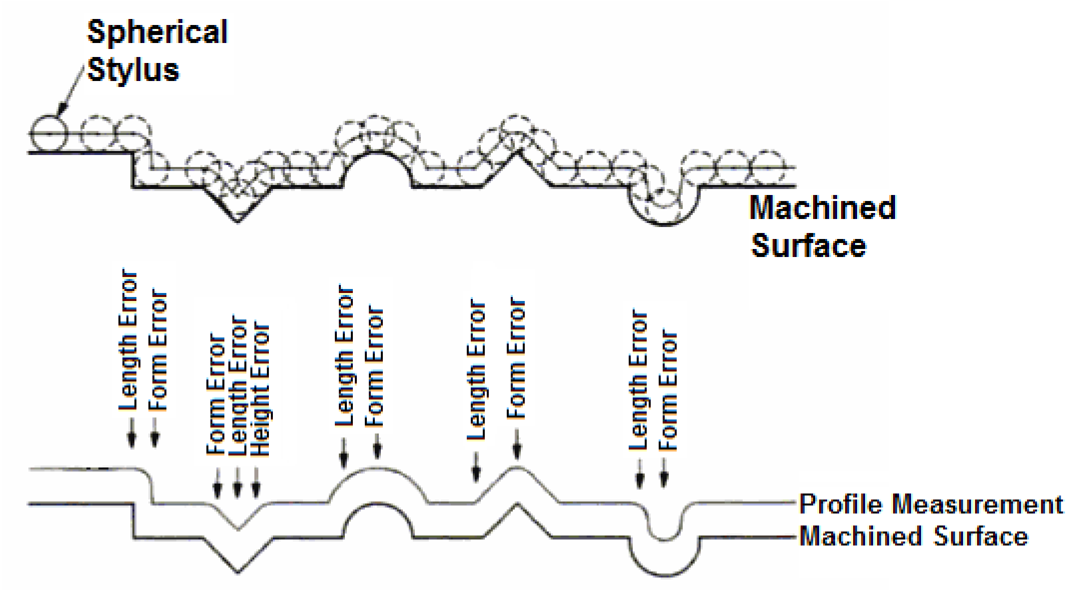

Figure 3.19 Typical Contact Measurement [62]

Non-contact measurement is another type of surface measurement method. Interferometry is a typical example of non-contact measurement method and this method depends on optical systems. Interferometry is a traditional technique in which a pattern of bright and dark lines result an optical difference between beams reflected from reference and measured surface. The light is separated inside the interferometry device by a beam-splitter. Then, one beam is guided to reference surface, while the other beam is oriented to the machined surface, tried to be measured. After the guided beams reflect from the surfaces, they interfere inside the optical system. The name of the interferometry comes from the interference of beams. The constructive and destructive interference of the beams produce the light and dark fringe pattern. Then, three dimensional interferogram of the surface is produced and this is transformed to three dimensional image providing surface structure analysis [63]. In Figure 3.20, schematic view of the optical system of white light interferometry is shown.

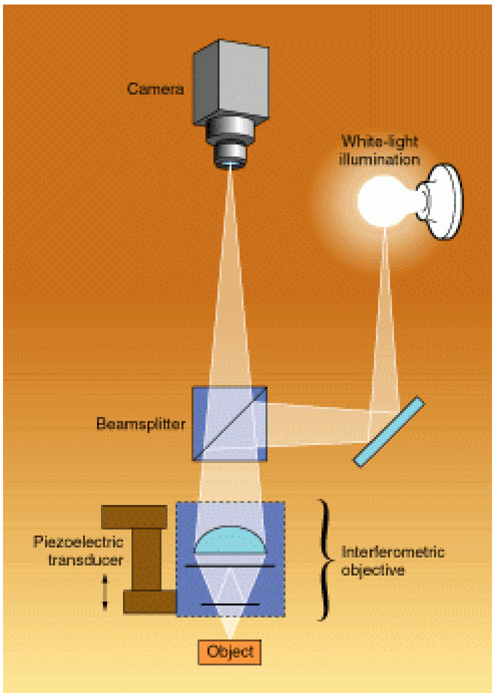

Figure 3.20 Schematic View of Optical System of White Light Interferometry [64]

In this thesis, Zygo NewView 5000, which is a white light interferometry device, was used to measure surface roughness and technical specifications are given in Appendix B. In the study, measurements were performed on 0.27 mm x 0.36 mm area. So, on that small area, the roughness values of the surfaces have been measured. Figure 3.21 shows the interferometry used for the measurement of machined germanium surfaces.

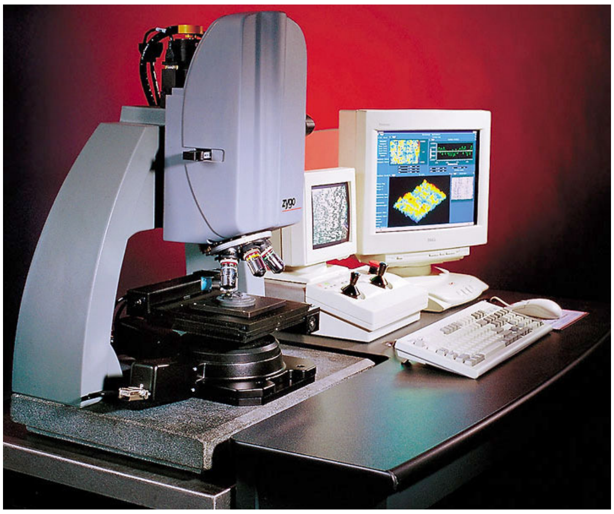

Figure 3.21 Zygo NewView 5000 White Light Interferometry [65]

The results of the surface roughness can be interpreted by a number of ways. R_z or PV, R_a and R_q or rms are the most common ones. During the measurements of surface roughness, to interpret the result of the interferometry first of all, the mean line of measurement is determined. The total area above the mean line is equal to the area below. In Figure 3.22, mean line, Q, which is the roughness sampling length, x axis, in the direction of mean line, and y axis, which shows the vertical deviations of the real surface, are shown [66].

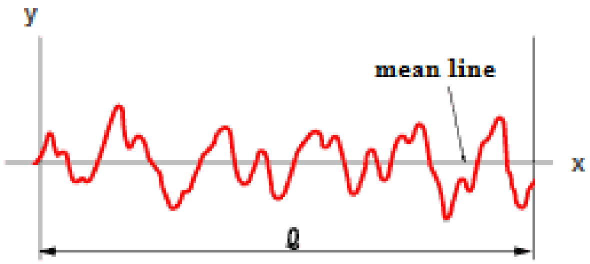

Figure 3.22 Surface Roughness Measurement [66]

R_z or PV is the sum of R_p and R_v where R_p is the top peak height and R_v is bottom valley depth on the surface. In Figure 3.23, R_z or PV (Peak to Valley) roughness of the surface is shown.

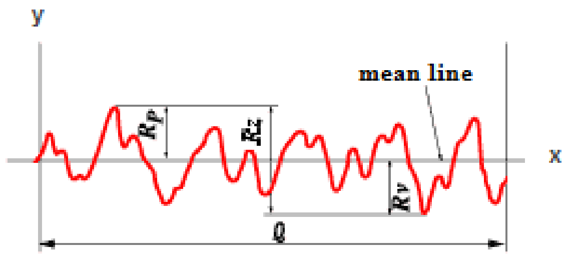

Figure 3.23 R_z or PV Roughness Measurement [66]

R_a is the arithmetic average of the absolute values and it is measured with the formulation (3.2). R_a is also defined as center line average. Figure 3.24 shows the R_a roughness measurement of the machined surface.

$$R_a = 1/Q\int^{Q}\{z(x)\}dx \tag{3.2}$$

Where;

R_a: Arithmetic Surface Roughness or Center Line Average

Q: roughness sampling length

z(x): roughness curve [67]

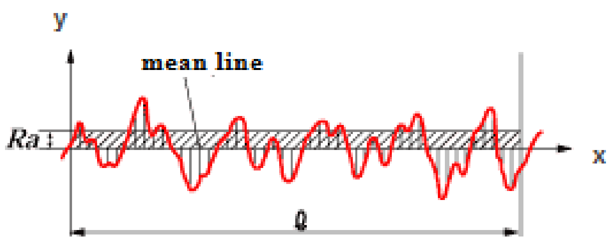

Figure 3.24 R_a Roughness Measurement [66]

R_q or rms is the root mean square measurement of the surface roughness and it is measured with the Equation (3.3). Figure 3.25 shows the R_q or rms roughness measurement of the machined surface.

$$R_q = \sqrt{1/Q\int^{Q}\{z^2(x)\}dx} \tag{3.3}$$

Where;

R_q: Root Mean Square Roughness

Q: length of the surface

z(x): roughness curve [67]

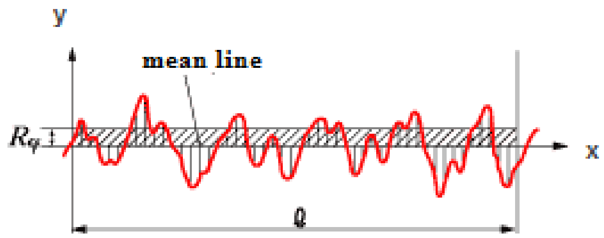

Figure 3.25 R_q or rms Roughness Measurement [66]

In this study, the surface roughness of the machined germanium surfaces were evaluated by R_z or PV, R_a and R_q or rms roughness types with Zygo NewView 5000 White Light Interferometry.

CHAPTER 4

EXPERIMENTAL SETUP

4.1 Introduction

In this experimental study, as a single point diamond turning machine, Precitech Freeform 700 U has been used as mentioned in Section 3.2. During machining applications, X and Z axes have been controlled by this CNC machine so both axes move under computer control. In this machine, spindle, on which the work-piece is mounted, is translated by X axis on slides and the tool holder is also translated by Z axis on slides, which is perpendicular to X axis. By the simultaneous control of these two axes, flat and spherical configurations, performed in this thesis study, could be machined.

The part and the cutter have to be settled appropriately to the machine to manufacture precise surfaces. For this thesis study, polycrystalline diamond inserts have been used during machining instead of non-controlled waviness mono-crystalline diamond tools. So, compatible tools were designed for PCD inserts and this situation changed the setup of tool and its position on the holder. Thus, this chapter will give information about the tool and its installation to the machine.

As much as the tool, the appropriate settlement of the work-piece is important to manufacture precise surfaces. This chapter will continue to give information about the work-piece setup for machining of germanium by single point diamond turning.

4.2 Polycrystalline Diamond Tool Setup

In this study, instead of mono-crystalline diamond tools, polycrystalline diamond tools were used as mentioned in Section 3.4. For rough cutting of germanium, polycrystalline diamond inserts were supplied. ISO-Code inserts are sorted out by their insert shape, clearance angle, tolerance class, insert feature, size, insert thickness, cutting corner, cutting edge, cutting direction and type designation. Therefore, DPGW11T304FST polycrystalline diamond inserts, used in experimental studies have rhomboid shape, 0^o rake angle, 11^o clearance angle and 0.4 mm cutting edge corner.

Figure 4.1 Polycrystalline Diamond Insert DPGW11T304FST (Kennametal Inc.)

Generally, polycrystalline diamond tools machine ductile materials like aluminum alloys for mechanical applications like in automotive industry in addition to metal matrix composites, titanium alloys, etc. as mentioned in Section 2.5 so inserts with positive rake angle are common in the market. However, in this thesis study, germanium, which is a brittle material, has been cut off and brittle materials are generally machined with negative rake angle tools and in the literature, tools having extremely negative rake angles were suggested for machining of germanium.

Therefore, the negative rake angle had to be obtained from the tool instead of insert since negative rake angle PCD insert could not be purchased from the market.

For rough cutting of germanium, -25^o and -45^o rake angles were selected by taking the previous studies into account. Since there is no negative rake angle insert, 0^o rake angle inserts have been purchased which are closest to negative rake angle. Then, since tools in the market, compatible with polycrystalline diamond inserts, could not also reach that extreme rake angles, instead of purchasing, two tools with -25^o and -45^o rake angles have been designed and manufactured. The technical drawing of the tools are shown in Appendix C. In Figure 4.2, two different tools, compatible with DPGW11T304FST polycrystalline diamond insert, are seen. These tools were manufactured from CPPU cold work tool steel, technical specifications of which are given in Appendix D. Tool, on the left, provided -25^o rake angle while tool, on the right, provided -45^o rake angle. Unfortunately, as tools have had more negative rake angles, they had more positive clearance angles. So, tool with -25^o rake angle has 36^o clearance angle and tool with -45^o rake angle has 56^o clearance angle as like in the study of Yan et. al [21].

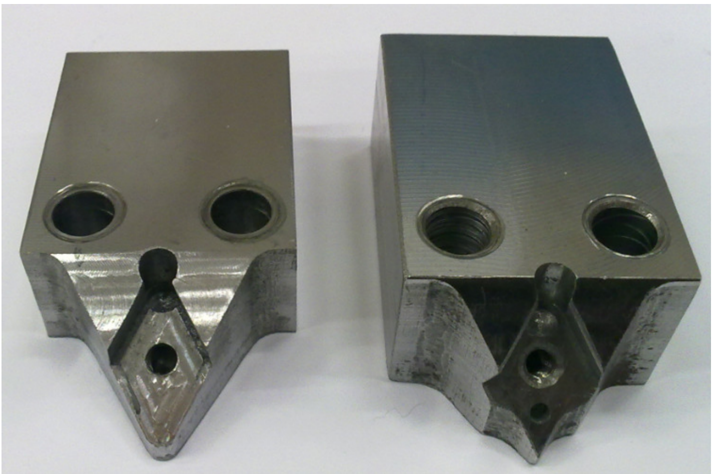

Figure 4.2 Tools with -25^o and -45^o Rake Angles

The manufactured tools had similar dimensions to perform same stiffness so not to change the cutting conditions for them. Also, during the design, the position of the tool at the tool holder of the single point diamond turning machine was taken into account. Two holes at the shank of the tool come up to holes on the tool holder. Actually, the tool holder of the machine is designed for mono-crystalline diamond tools and mono-crystalline diamond tool is placed on the tool holder by a part fixed to the tool holder by using these holes. Figure 4.3 shows the layout of mono-crystalline diamond tool to the holder.

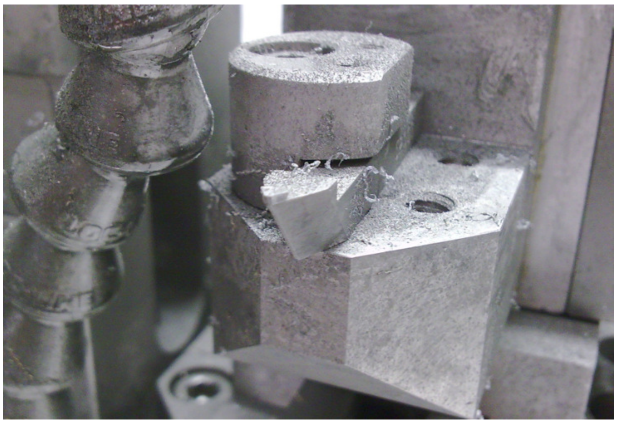

Figure 4.3 Layout of Mono-crystalline Diamond Tool on Tool Holder

The same holes on tool holder have been used for the tools designed for polycrystalline diamond inserts. The tool has been placed on tool holder from that holes and fixed to their place by screws before machining. Figure 4.4 shows the setup of the tool for PCD inserts to the machine, in (a) position of the tool on tool holder is seen and in (b) position of the tool in the machine can be seen.

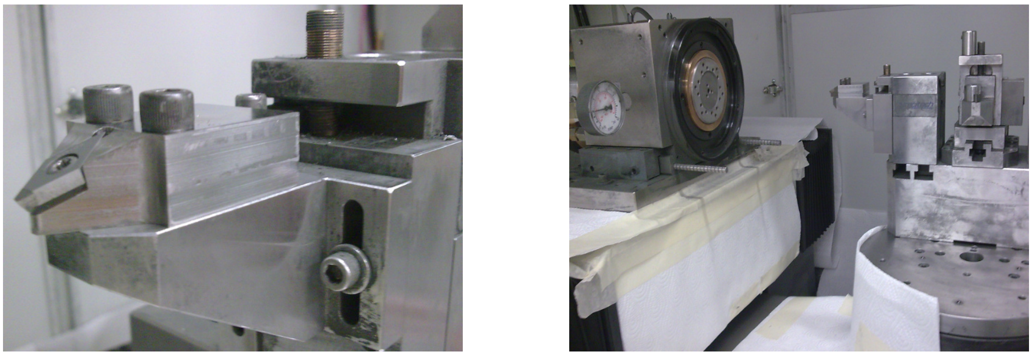

(a) (b)

Figure 4.4 Layout of Polycrystalline Diamond Tool on Machine

4.3 Work-piece Setup

As mentioned in Section 3.2, the work-piece is placed on the vacuum chunk by negative air pressure and held in its position during machining. However, the position of the work-piece is critical to manufacture precise surfaces. Therefore, the axis of the lens must be aligned with the axis of the spindle on which the chuck is located. This application is called centering.

In this thesis study, rough cutting application was performed so, 2.54 μm concentricity of axes has been accepted enough for machining application according to documents of machine manufacturer. Therefore, with the help of a dial indicator, which has be located on the machine base or Z axis slide, the concentricity of axes of work-piece and spindle had been measured before all machining processes.

Thus, the probe of the indicator has been touched on the outer diameter of the work-piece and part was rotated by hand for 360^{o} and deviation of the measurement was calculated. Then according to that, the work-piece was placed to its position by hitting slowly with a plastic stick or hammer on the highest point as shown in Figure 4.5. The measurement and placing by hitting procedure continues up to 2.54

µm concentricity difference of axes for a full turn of work-piece. After tool and work-piece setup applications, part program could be loaded and germanium work-pieces have been machined.

Figure 4.5 Centering Application of Work-piece

CHAPTER 5

RESULTS OF THE EXPERIMENTAL STUDY

5.1 Introduction

In this thesis study, rough cutting conditions of germanium were examined and these conditions were harsher when compared with finish cutting. The previous manufacturing information in ASELSAN Inc., recommendations from single point diamond turning machine manufacturers, diamond tool manufacturers and previous studies, mentioned in Chapter 2, have been guide for selection of parameters.

In addition to this knowledge, some trials were made by polycrystalline diamond tools on germanium before experimental studies and as a result of these, parameters have been selected for rough cutting conditions. Therefore, 0.4 mm nose radius polycrystalline diamond inserts were obtained and the cutting tools were provided with -25^{o} and -45^{o} rake angles. Spindle speed, depth of cut and feed rate were selected between 2000-5000 RPM, 40-200 μm and 5-20 mm/min respectively as machining conditions. Hence, spindle speed, feed rate and depth of cut had constant values at each runs. However, cutting speed was permanently changing depending on the diameter of the cutting point during run.

The experimental study of rough cutting of germanium with polycrystalline diamond tools have been started after the fulfillment of single point diamond turning machine setup including the setup of the tool and the work-piece. This study has included three main machining applications. In the first experiment, flat germanium disk had been machined and the roughness of the machined surfaces had been measured by white light interferometry device for a times determined according to experimental design and the mathematical model between surface roughness and experimental parameters as feed rate, depth of cut, spindle speed and rake angle had been obtained by 2 Level Full Factorial Design. After that, in the second experiment the same study has been performed for a convex lens to compare the results between flat disk and convex lens. Thus, the second machining set was generated.

In addition to these studies, in the third experimental set to improve the mathematical model, 3 Level Full Factorial Design has been used to obtain the relationship between surface roughness and the parameters for machining flat disk of germanium. However, this time three parameters were used to decrease the number of runs since the number has already been increased because of using 3 level model instead of 2. Therefore, the rake angle was eliminated from parameters list and thus cutting parameters as feed rate, depth of cut and spindle speed constituted that. Moreover, by selecting a number of results that have been obtained during experiment 3, Box-Behnken Design has been formed and a different mathematical model has been obtained. That model was also a 3 level model and it was used to compare all results that had been obtained by 2 and 3 Level Full Factorial Designs for flat surface.

Hence, this chapter will give information about the results of the surface roughness for the related cutting conditions and rake angle of the tool. Moreover, the mathematical models that have been obtained by design of experiment studies will be mentioned and finally the discussions of the obtained results will be given in the further sections of the chapter.

5.2 Results of the Initial Trials

In this experimental study, the most important thing was to identify that germanium could be machined by polycrystalline diamond tools. After that, the mathematical relationship between the surface roughness and the parameters has been tried to be identified. Therefore, the experimental studies have been started by the machining of flat surfaces on 40 mm diameter germanium disk. After machining, the roughness results were obtained from a white-light interferometry machine. A typical roughness measurement of germanium disk is shown in Figure 5.1.

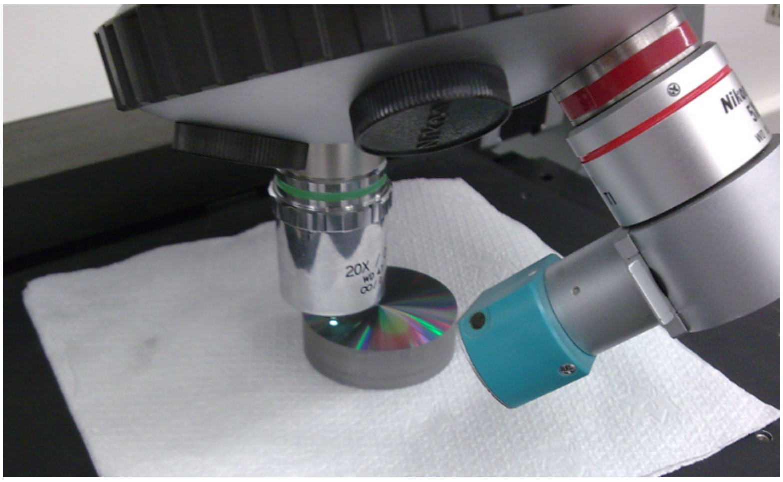

Figure 5.1 Surface Roughness Measurement with White-Light Interferometry

Actually, the generated germanium blanks that is purchased from manufacturers could be directly cut in finish cutting conditions without having rough cutting previously and the necessary roughness values could be gathered. The rough cutting applications are only done to give shape to work-piece material so, the surface roughness has second priority. Therefore, considering this knowledge the surface roughness values of the generated blanks were accepted the highest limit to the diamond turned germanium in rough cutting conditions. Surface roughness of a number of germanium blanks were measured and typical PV, rms and R_a roughness values have been measured 6-7 μm, 800-850 nm and 600-700 nm respectively.

First of all, a number of cutting applications were performed to define the machining characteristic between germanium and polycrystalline diamond tools. Thus, germanium disk has been machined both on finish and rough cutting conditions. Surface roughness of both conditions had given quite same results as machining with mono-crystalline diamond tools. At even high feed rates and depth of cuts, the surface roughness values were below the values of generated blanks.

For instance, surface had 4493.7 nm PV, 441.9 nm rms and 325.8 nm R_a roughness when machined with 30 mm/min feed rate, 20 μm depth of cut and 2000 RPM spindle speed using -25^o rake angle tool. In another example, 801.1 nm PV, 27.2 nm rms and 16.6 nm R_a roughness values were obtained with 5 mm/min feed rate, 250 μm depth of cut and 1500 RPM spindle speed using -25^o rake angle tool. Therefore, the results showed that germanium could be machined by polycrystalline diamonds for rough cutting applications instead of non-controlled waviness mono-crystalline diamond tools.

Hopeful results were also gathered when the surface was machined at finish cutting conditions. According to optical requirements specified in technical documents of ASELSAN Inc., rms surface finish of an optical surface must be less than 25.4 nm within its whole surface for germanium lenses. In these first trials, the average roughness (R_a) was measured between 2.5 to 3.8 nm at three different runs in finish cutting conditions such as 2.5 mm/min feed rate, 4 μm depth of cut and 2000 RPM spindle speed using -25^o rake angle tool.

5.3 Two Level Full Factorial Design for Flat Disk

In the experiment, the machining applications were performed by cutting fluid, Dovent IP 175/195. Polycrystalline diamond insert was DPGW11T304FST of Kennametal. Tools with two different rake angles were used and the adjusting of the rake angle of tools affected clearance angle so, tools with different clearance angles were obtained. The properties of cutting tools were given in Table 5.1.

Table 5.1 Cutting Tool Parameters for Experiment 1

Properties	Tool 1	Tool 2
Polycrystalline Diamond Insert	DPGW11T304FST	
Nose Radius (mm)	0.4	
Rake Angle (^{o})	-25	-45
Clearance Angle (^{o})	36	56

In the first experimental set, 2 Level Full Factorial Design with 4 parameters (2^4 Full Factorial Design) was used. Thus, flat germanium disk was machined at high and low level of four parameters. The parameters were chosen as feed rate, depth of cut, spindle speed and rake angle and as mentioned in Section 3.5, they form corners of rectangular prism. The high and low level of parameters were chosen at the rough cutting conditions. The selected cutting and tool geometry parameters and the order of runs are given in Table 5.2.

Table 5.2 Selected Parameters for Experiment 1

Run	Feed Rate (mm/min)	Depth of Cut (μm)	Spindle Speed (RPM)	Rake Angle (^{o})
1	5	40	2000	-25
2	20	40	2000	-25
3	5	200	2000	-25
4	20	200	2000	-25
5	5	40	5000	-25
6	20	40	5000	-25
7	5	200	5000	-25
8	20	200	5000	-25
9	5	40	2000	-45
10	20	40	2000	-45
11	5	200	2000	-45
12	20	200	2000	-45
13	5	40	5000	-45
14	20	40	5000	-45
15	5	200	5000	-45
16	20	200	5000	-45

Therefore, at these parameters 16 runs were realized. The machined surfaces were measured at Zygo NewView 5000 White Light Interferometry and the measurement point was taken as the middle of the radius so, it was 10 mm away from the center and the outer diameter as shown in Figure 5.2 and some measurement results on interferometry of this experiment are given in Appendix E. Thus, 16 runs, necessary for 2^4 Full Factorial Design, were completed. The surface roughness of machined surfaces can be seen in Table 5.3 and mathematical relationship between surfaces roughness and parameters has been formulated using the results in Table 5.3.

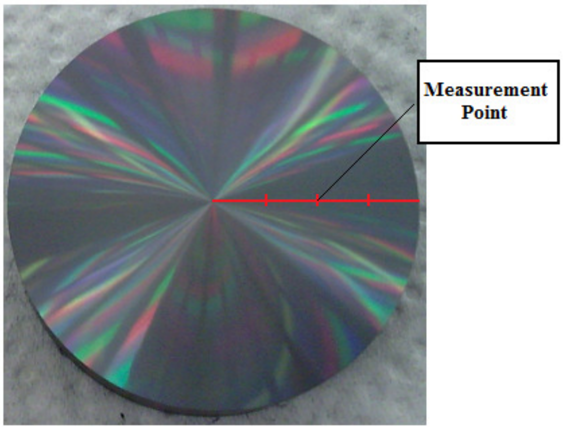

Figure 5.2 Measurement Point of Runs in Experiment 1

Table 5.3 Results of the Surface Roughness Measurements for Experiment 1

Run	Feed Rate (mm/min)	Depth of Cut (μm)	Spindle Speed (RPM)	Rake Angle (°)	Surface Roughness		
					PV (nm)	rms (nm)	R_a (nm)
1	5	40	2000	-25	955.2	92.5	70.6
2	20	40	2000	-25	2959.4	238.4	168.6
3	5	200	2000	-25	1150.5	114.8	88.5
4	20	200	2000	-25	2823.6	270.7	197.0
5	5	40	5000	-25	41.1	3.8	2.9
6	20	40	5000	-25	689.4	45.6	29.5
7	5	200	5000	-25	124.4	5.9	4.4
8	20	200	5000	-25	980.8	79.2	58.0
9	5	40	2000	-45	1831.7	141.5	111.0
10	20	40	2000	-45	5587.3	467.7	346.1
11	5	200	2000	-45	1846.0	166.5	129.5
12	20	200	2000	-45	3193.5	322.3	244.7
13	5	40	5000	-45	813.3	81.2	63.1
14	20	40	5000	-45	1532.4	183.6	146.2
15	5	200	5000	-45	819.5	87.9	69.3
16	20	200	5000	-45	832.1	89.0	70.1

The mathematical formulation, found by 2^4 Full Factorial Design, is in the form like in Equation (5.1) and as shown, there were 16 coefficients from a_0 to a_{1234} that had to be calculated and the equations for coefficients had been obtained from the book of Introduction to Design of Experiments with JMP Experiments by J. Goupy and L. Creighton [68]. However, only the equations for 2^2 Full Factorial Design are given in the book so, 2^4 Full Factorial Design equations had been acquired from the examples in the further chapters. The equations for 2^2 Full Factorial Design can be seen in Appendix F. Therefore, coefficients have been calculated according to equations and they are given in Table 5.4 for PV, rms and R_a roughness separately.

$$\begin{aligned} R &= a_0 + a_1 * f + a_2 * doc + a_3 * S + a_4 * r + a_{12} * f * doc + a_{13} * f * S \\ &+ a_{14} * f * r + a_{23} * doc * S + a_{24} * doc * r + a_{34} * S * r + a_{123} * f * doc * r \\ &+ a_{124} * f * doc * r + a_{134} * f * S * r + a_{1234} * f * doc * S * r \end{aligned} \tag{5.1}$$

Where;

R: Roughness

f: Feed rate

doc: Depth of cut

r: Rake angle

Table 5.4 Coefficients for Roughness Equation (5.1) for Experiment 1

Coefficient	PV	rms	R_a
a_0	1636.265	149.421	112.478
a_1	688.540	62.634	45.057
a_2	-164.967	-7.376	-4.778
a_3	-907.147	-77.398	-57.035
a_4	420.702	43.042	35.028
a_{12}	-202.352	-14.385	-10.288
a_{13}	-409.014	-35.325	-24.535
a_{14}	40.807	10.532	9.219
a_{23}	125.040	0.845	-0.203
a_{24}	-219.240	-18.677	-14.323
a_{34}	-150.511	-4.644	-3.303
a_{123}	140.059	5.659	3.373
a_{124}	-186.976	-19.573	-14.971
a_{134}	-137.429	-11.985	-8.763
a_{234}	85.637	3.204	1.845
a_{1234}	72.655	2.978	1.316

It must be noted that Equation (5.1) is in coded units. So, the highest points of parameters are +1 while the lowest points are -1 in the equation. A transformation must be done to enter the parameters as feed rate, depth of cut, spindle speed and rake angle in engineering units. After this transformation, the mathematic formulation became as in Equation (5.2) but the coefficients in Table 5.4 remained same.

$$
\begin{aligned}
R &= a_0 + a_1 * [(f - 12.5)/7.5] + a_2 * [(doc - 120)/80] \\
&+ a_3 * [(S - 3500)/1500] + a_4 * [(r - (-35))/-10] \\
&+ a_{12} * [(f - 12.5)/7.5] * [(doc - 120)/80] \\
&+ a_{13} * [(f - 12.5)/7.5] * [(S - 3500)/1500] \\
&+ a_{14} * [(f - 12.5)/7.5] * [(r - (-35))/-10] \\
&+ a_{23} * [(doc - 120)/80] * [(S - 3500)/1500] \\
&+ a_{24} * [(doc - 120)/80] * [(r - (-35))/-10] \\
&+ a_{34} * [(S - 3500)/1500] * [(r - (-35))/-10] \\
&+ a_{123} * [(f - 12.5)/7.5] * [(doc - 120)/80] * [(r - (-35))/-10] \\
&+ a_{124} * [(f - 12.5)/7.5] * [(doc - 120)/80] * [(r - (-35))/-10] \\
&+ a_{134} * [(f - 12.5)/7.5] * [(S - 3500)/1500] * [(r - (-35))/-10] \\
&+ a_{234} * [(doc - 120)/80] * [(S - 3500)/1500] * [(r - (-35))/-10] \\
&+ a_{1234} * [(f - 12.5)/7.5] * [(doc - 120)/80] * [(S - 3500)/1500] \\
&* [(r - (-35))/-10]
\end{aligned} \tag{5.2}
$$

Finally, the experimental study was finished by an ANOVA study to conclude the significance of each coefficient for the mathematical model. The procedure started with the elimination of some coefficients. Hence, coefficients a_{123}, a_{124}, a_{134}, a_{234} and a_{1234} were eliminated and the equations take the form in Equation (5.3). Surface roughness was estimated by these 11 coefficients and the results are given in Table 5.5, also difference between the real values and estimated values are given in Table 5.5.

$$
\begin{aligned}
R &= a_0 + a_1 * f + a_2 * doc + a_3 * S + a_4 * r + a_{12} * f * doc + a_{13} * f * S \\
&+ a_{14} * f * r + a_{23} * doc * S + a_{24} * doc * r + a_{34} * S * r
\end{aligned} \tag{5.3}
$$

Table 5.5 Estimated and Residual Values for Experiment 1

Run	Estimated			Residual		
	PV (nm)	rms (nm)	R_a (nm)	PV (nm)	rms (nm)	R_a (nm)
1	783.9	66.9	50.8	171.4	25.7	19.8
2	3302.1	270.5	192.1	-342.6	-32.1	-23.5
3	1047.0	116.5	90.8	103.5	-1.7	-2.3
4	2755.8	262.6	191.0	67.8	8.1	6.0
5	-161.5	-9.7	-7.2	202.6	13.5	10.1
6	720.7	52.6	36.0	-31.3	-7.1	-6.4
7	601.9	43.4	32.0	-477.4	-37.4	-27.6
8	674.6	48.2	34.1	306.2	31.0	23.9
9	2283.2	178.5	137.6	-451.5	-37.0	-26.6
10	4964.6	424.3	315.8	622.8	43.4	30.3
11	1669.4	153.5	120.4	176.6	13.0	9.1
12	3541.4	341.7	257.5	-347.9	-19.4	-12.7
13	735.8	83.4	66.4	77.5	-2.2	-3.4
14	1781.2	187.9	146.5	-248.8	-4.3	-0.3
15	622.2	61.8	48.4	197.3	26.1	20.9
16	858.1	108.7	87.3	-26.1	-19.7	-17.2

From the columns of residual values, sum of squares of errors were calculated by squared and summed of residuals and the results were divided by freedom, which is the number of eliminated coefficients and mean square of errors were obtained. Then, the square root of the mean square of errors have been found to calculate root mean square of errors and also standard deviation, the square root of mean square of root divided by total number of coefficients, has been found. The results were given in Table 5.6.

Table 5.6 Summary of Errors and Standard Deviation for Experiment 1

	PV	rms	R_a
Sum of Squares of Errors	1377214.474	9246.558	5078.865
Mean Square of Errors	275442.895	1849.312	1015.773
Root Mean Square of Errors	524.827	43.004	31.871
Standard Deviation	131.207	10.751	7.968

The ratio of coefficient to the standard deviation is t-ratio. Using t-Ratio and freedom, which is 5 in this model, p-Value can be found. p-Value is the probability that a coefficient is not significant [68]. Therefore, smaller the p-Value, more significant the coefficient can be concluded and by this, significance of the parameter can be found out. The acceptance probability for coefficients was set at p-Value less than 0.1 as mentioned in the book of Introduction to Design of Experiments with JMP Experiments by J. Goupy and L. Creighton. This means that the coefficient would be zero 10% of repeated experiments. So, coefficient would be significant 90% of experiments. Table 5.7 gave the results of t-Ratio and p-Values for three different surface roughness. Thus, as shown from the Table 5.7, a_0, a_1, a_3, a_4 and a_{13} are the most significant coefficients for the experimental study because of their low p-Value and this showed the significance of parameters feed rate, spindle speed and rake angle for the process.

Table 5.7 t-Ratio and p-Values for Experiment 1

	t-Ratio			p-Value		
Coefficient	PV	rms	R_a	PV	rms	R_a
a_0	12.471	13.898	14.117	**<0.00001**	**0.00004**	**0.00003**
a_1	5.248	5.826	5.655	**0.00333**	**0.00211**	**0.00240**
a_2	-1.257	-0.686	-0.600	0.26428	0.52322	0.57466
a_3	-6.914	-7.199	-7.158	**0.00097**	**0.00081**	**0.00083**
a_4	3.206	4.004	4.396	**0.02384**	**0.01028**	**0.00705**
a_{12}	-1.542	-1.338	-1.291	0.18370	0.23852	0.25317
a_{13}	-3.117	-3.286	-3.079	**0.02634**	**0.02181**	**0.02750**
a_{14}	0.311	0.980	1.157	0.76835	0.37209	0.29954
a_{23}	0.953	0.079	-0.025	0.38436	0.94010	0.98102
a_{24}	-1.671	-1.737	-1.798	0.15559	0.14290	0.13210
a_{34}	-1.147	-0.432	-0.415	0.30329	0.68374	0.69535

5.4 Two Level Full Factorial Design for Convex Lens

In this experiment with convex lens, the machining applications were performed in the same conditions as in the experimental design with flat disk. So, the cutting tool parameters and cutting fluid were same. In the second experimental set, again 2 Level Full Factorial Design with 4 parameters (2^4 Full Factorial Design) was used. Therefore, the selected machining and tool geometry parameters and the order of runs was same with the first experimental study for flat disk and this whole list is given in Table 5.2.

This experimental study was similar to first one. However, it was performed on convex lens to compare the results with flat disk. Hence, this became a good comparison for different surface configurations. Thus, 16 runs were performed and machined surfaces were measured at Zygo NewView 5000 Interferometry. The measurement point was taken as the middle point of the radius as shown in Figure

5.3 and some measurement results on interferometry of this experiment are given in Appendix E. The surface roughness values of machined surfaces can be seen in Table 5.8. Mathematical relationship between surfaces roughness and the parameters has been formulated using the results in Table 5.8.

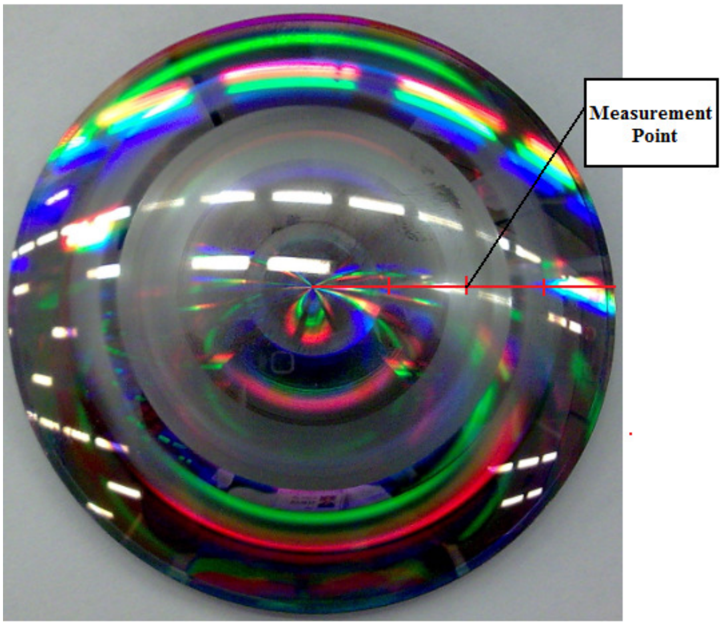

Figure 5.3 Measurement Point of Runs in Experiment 2

Table 5.8 Results of the Surface Roughness Measurements for Experiment 2

Run	Feed Rate (mm/min)	Depth of Cut (μm)	Spindle Speed (RPM)	Rake Angle (°)	Surface Roughness		
					PV (nm)	rms (nm)	R_a (nm)
1	5	40	2000	-25	1640.3	112.3	78.4
2	20	40	2000	-25	3353.7	345.1	270.1
3	5	200	2000	-25	3183.0	186.3	116.8
4	20	200	2000	-25	4150.6	317.8	249.9
5	5	40	5000	-25	944.8	49.8	30.4
6	20	40	5000	-25	841.8	80.6	61.7
7	5	200	5000	-25	240.2	8.7	6.3
8	20	200	5000	-25	3322.9	232.9	141.5
9	5	40	2000	-45	2971.5	186.9	119.9
10	20	40	2000	-45	6340.5	564.7	413.9
11	5	200	2000	-45	2830.4	193.0	124.8
12	20	200	2000	-45	6538.1	613.7	442.7
13	5	40	5000	-45	797.4	12.7	4.8
14	20	40	5000	-45	3500.2	210.4	111.1
15	5	200	5000	-45	322.7	13.6	8.5
16	20	200	5000	-45	2273.1	154.1	79.2

The mathematical formulation, found by 2^4 Full Factorial Design for convex lens, is in the form like in Equation (5.1). It is same equation that was obtained for the experimental study of flat disk. However, only the coefficients were different because of the different surface roughness values obtained for convex lens. As shown from the equation, there were 16 coefficients from a_0 to a_{1234} and they were calculated in the same method for Experiment 1 and were given in Table 5.9 for PV, rms and R_a roughness.

Table 5.9 Coefficients for Roughness Equation (5.1) for Experiment 2

Coefficient	PV	rms	R_a
a_0	2703.212	205.170	141.243
a_1	1086.920	109.740	80.010
a_2	154.431	9.850	4.961
a_3	-1172.814	-109.820	-85.814
a_4	493.539	38.474	21.871
a_{12}	126.617	4.863	2.102
a_{13}	-132.816	-35.615	-37.068
a_{14}	379.327	32.333	18.595
a_{23}	-145.097	-2.883	-1.528
a_{24}	-360.095	-9.890	-4.279
a_{34}	-300.571	-36.127	-26.386
a_{123}	177.529	12.158	6.447
a_{124}	-178.349	-6.644	-3.552
a_{134}	-170.143	-21.933	-17.271
a_{234}	-74.707	-10.933	-6.223
a_{1234}	-313.920	-24.674	-13.871

As mentioned in Section 5.3, Equation (5.1) is in coded units. So, the highest points of parameters are +1 while the lowest points are -1 in it. A transformation must be done to enter the parameters in engineering units. After the transformation, the mathematic formulation became as in Equation (5.2), However, the coefficients, given in Table 5.9, remained same.

Finally, the experimental work for convex lens was finished by an ANOVA study to conclude the significance of each coefficient for the mathematical relationship. The procedure, same as in the experimental study for flat disk, started with the elimination of some coefficients. Hence, coefficients a_{123}, a_{124}, a_{134}, a_{234} and a_{1234} were eliminated and the equation became as in Equation (5.3). Surface roughness was estimated by these 11 coefficients and the results were given in estimated column in Table 5.10, also difference between the real values and estimated values were given in residual column.

Table 5.10 Estimated and Residual Values for Experiment 2

Run	Estimated			Residual		
	PV (nm)	rms (nm)	R_a (nm)	PV (nm)	rms (nm)	R_a (nm)
1	1708.5	109.6	71.7	-68.3	2.7	6.7
2	3136.1	325.9	264.4	217.7	19.2	5.7
3	2774.5	145.1	89.0	408.5	41.2	27.8
4	4708.6	380.9	290.2	-557.9	-63.1	-40.3
5	519.8	39.2	30.0	424.9	10.6	0.4
6	1416.2	113.1	74.5	-574.4	-32.5	-12.8
7	1005.5	63.2	41.2	-765.2	-54.5	-34.9
8	2408.3	156.5	94.1	914.6	76.3	47.4
9	3258.3	213.9	139.5	-286.8	-27.0	-19.6
10	6203.1	559.6	406.7	137.4	5.1	7.2
11	2883.9	209.9	139.7	-53.5	-16.9	-14.9
12	6335.2	575.0	415.3	202.9	38.7	27.4
13	867.3	-1.0	-7.7	-69.9	13.7	12.5
14	3280.9	202.2	111.2	219.3	8.2	-0.1
15	-87.4	-16.5	-13.6	410.2	30.2	22.0
16	2832.7	206.1	113.7	-559.6	-52.0	-34.5

From the columns of residual values, sum of squares of errors, mean square of errors, root mean square of errors and standard deviation were calculated same as in Experiment 1. The table of results for three different roughness were given in Table 5.11.

Table 5.11 Summary of Errors and Standard Deviation for Experiment 2

	PV	rms	R_a
Sum of Squares of Errors	3142399.016	22421.662	9337.853
Mean Square of Errors	628479.803	4484.332	1867.571
Root Mean Square of Errors	792.767	66.965	43.215
Standard Deviation	198.192	16.741	10.804

The ratio of coefficient to the standard deviation is t-Ratio and by using t-Ratio and freedom, which is 5 for this model, p-value could be found out which gives idea about significance of parameters as mentioned in Section 5.3. Table 5.12 gives the results of t-Ratio and p-Value for three different roughness types. So, as shown from the Table 5.12 a_0, a_1, a_3 and a_4 are the most significant coefficients for surface roughness because of their low p-Value and this showed the significance of parameters feed rate, spindle speed and rake angle for the process.

Table 5.12 t-Ratio and p-Value for Experiment 2

	t-Ratio			p-Value		
Coefficient	PV	rms	R_a	PV	rms	R_a
a_0	13.639	12.255	13.073	**0.00004**	**0.00006**	**0.00005**
a_1	5.484	6.555	7.406	**0.00275**	**0.00124**	**0.00071**
a_2	0.779	0.588	0.459	0.47122	0.58209	0.66550
a_3	-5.918	-6.560	-7.943	**0.001963**	**0.00123**	**0.00051**
a_4	2.490	2.298	2.024	**0.05516**	**0.06995**	**0.09887**
a_{12}	0.639	0.290	0.195	0.55094	0.78346	0.85307
a_{13}	-0.670	-2.127	-3.431	0.53255	**0.08673**	**0.01862**
a_{14}	1.914	1.931	1.721	0.11380	0.11135	0.14587
a_{23}	-0.732	-0.172	-0.141	0.49702	0.87018	0.89338
a_{24}	-1.817	-0.591	-0.396	0.12891	0.58022	0.70844
a_{34}	-1.517	-2.158	-2.442	0.18972	**0.08340**	**0.05851**

5.5 Three Level Full Factorial Design for Flat Disk

Three level experimental designs were also performed in the study to compare the results with two level designs. Different from two level designs, in addition to highest and lowest levels of parameters, runs were also performed in the middle point of parameters and these results were used to obtain mathematical model. As mentioned in Section 5.1, instead of four, three parameters were selected as feed rate, depth of cut and spindle speed to decrease the number of cuts and as a result of this, 27 cuts have been realized.

In the third experiment, the machining applications were also performed by cutting fluid, Dovent IP 175/195. Polycrystalline diamond insert was DPGW11T304FST of Kennametal. Tool with -25^{o} rake angle was selected for machining since better results were obtained by that tool in previous studies. The clearance angle was again 36^o. The properties of cutting fluid and tool were given in Table 5.13.

Table 5.13 Cutting Tool Parameters for Experiment 3

Cutting Fluid	Dovent IP 175/195
Polycrystalline Diamond Insert	DPGW11T304FST
Nose Radius (mm)	0.4
Rake Angle (^{o})	-25
Clearance Angle (^{o})	36

The third experimental study was performed by 3 Level Full Factorial Design with 3 parameters (3^3 Full Factorial Design). Thus, flat germanium disk was machined at highest, lowest and center point of each three parameters. The highest and lowest points of the parameters, forming corners of rectangular prism as shown in Section 3.5, were chosen equal to first and second experimental study. The selected parameters and the order of runs are given in Table 5.14.

Table 5.14 Selected Parameters and Order of Runs for Experiment 3

Run	Feed Rate (mm/min)	Depth of Cut (μm)	Spindle Speed (RPM)
1	12.5	200	5000
2	20	120	2000
3	12.5	120	5000
4	20	120	5000
5	20	40	3500
6	12.5	40	5000
7	5	200	2000
8	5	40	5000
9	5	200	5000
10	12.5	40	3500
11	5	120	5000
12	5	200	3500
13	12.5	120	2000
14	5	40	3500
15	12.5	200	2000
16	12.5	40	2000
17	20	40	2000
18	5	120	2000
19	5	40	2000
20	12.5	120	3500
21	12.5	200	3500
22	20	200	5000
23	20	200	2000
24	5	120	3500
25	20	200	3500
26	20	40	5000
27	20	120	3500

Therefore, 27 runs were performed in the order given in Table 5.14 and then the machined surfaces were measured at Zygo NewView 5000 Interferometry as in previous experiments. However, different from previous experiments, the measurements were performed at 3 different points of work-piece. The machined work-piece had 40 mm outer diameter so, measurements were realized 5, 10 and 15 mm away from the center. The measurement points are shown in Figure 5.4 and some measurement results on interferometry of this experiment are given in Appendix E.

Measurement from three different points were used to determine the relationship between cutting speed and surface roughness and information about this will be represented in Section 6.2.5. The average surface roughness of three points on the machined surface can be seen in Table 5.15 and the whole list is given in Appendix G. The mathematical relationship between surface roughness and parameters were determined according to the average surface roughness values.

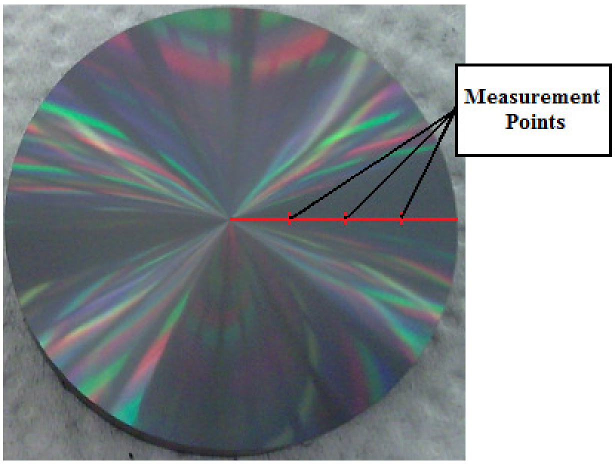

Figure 5.4 Measurement Point of Runs in Experiment 3

Table 5.15 Results of the Surface Roughness Measurements for Experiment 3

Run	Feed Rate (mm/min)	Depth of Cut (μm)	Spindle Speed (RPM)	PV (nm)	rms (nm)	R_a (nm)
1	12.5	200	5000	2010.3	91.8	50.7
2	20	120	2000	4182.3	321.7	221.5
3	12.5	120	5000	1452.6	104.6	75.8
4	20	120	5000	1812.0	122.1	74.2
5	20	40	3500	2932.1	217.2	144.8
6	12.5	40	5000	1416.3	109.6	77.5
7	5	200	2000	2593.5	145.3	97.3
8	5	40	5000	553.7	23.6	10.9
9	5	200	5000	532.0	19.6	8.8
10	12.5	40	3500	2693.3	147.7	92.3
11	5	120	5000	58.8	3.3	2.5
12	5	200	3500	273.7	8.4	4.1
13	12.5	120	2000	1761.6	128.9	87.9
14	5	40	3500	598.5	23.5	10.3
15	12.5	200	2000	2710.2	145.4	93.9
16	12.5	40	2000	2742.3	214.3	137.1
17	20	40	2000	4100.8	325.3	226.6
18	5	120	2000	848.5	21.9	9.5
19	5	40	2000	1551.8	50.9	17.7
20	12.5	120	3500	844.6	34.7	16.6
21	12.5	200	3500	1058.3	37.5	18.3
22	20	200	5000	1631.3	64.0	40.0
23	20	200	2000	4201.6	413.4	315.2
24	5	120	3500	288.2	8.2	4.5
25	20	200	3500	1888.1	145.7	109.4
26	20	40	5000	1346.9	88.7	65.7
27	20	120	3500	2019.8	141.3	105.1

The mathematical formulation, found by 3^3 Full Factorial Design, is in the form like in Equation (5.4). As shown from the equation, there were 17 coefficients from a_0 to a_{123} that had to be calculated and the equations for coefficients had been obtained from the software of JMP® 8. The coefficients have been calculated by the software and results are given in Table 5.16 for PV, rms and R_a roughness.

$$
\begin{aligned}
R = {} & a_0 + a_1 * f + a_2 * doc + a_3 * S + a_{12} * f * doc + a_{13} * f * S \\
& + a_{23} * doc * S + a_{11} * f * f + a_{22} * doc * doc + a_{33} * S * S \\
& + a_{112} * f * f * doc + a_{113} * f * f * S + a_{221} * S * S * f \\
& + a_{223} * doc * doc * S + a_{331} * S * S * f + a_{332} * S * S * doc \\
& + a_{123} * f * doc * S
\end{aligned}
\tag{5.4}
$$

Where;

R: Roughness

f: Feed rate

doc: Depth of cut

Table 5.16 Coefficients for Roughness Equation (5.4) for Experiment 3

Coefficient	PV	rms	R_a
a_0	1781.600	116.985	78.450
a_1	762.789	69.619	51.584
a_2	-47.031	-5.889	-2.053
a_3	-629.551	-51.707	-36.328
a_{12}	-75.228	-4.637	-2.443
a_{13}	-213.631	-34.107	-26.732
a_{23}	-14.098	-8.894	-9.982
a_{11}	-51.481	3.012	4.401
a_{22}	217.318	13.056	8.523
a_{33}	270.096	22.679	15.763
a_{112}	70.013	14.784	12.409
a_{113}	-220.497	-18.990	-14.613
a_{221}	-116.722	-3.863	-0.507
a_{223}	-111.350	-13.236	-9.658
a_{331}	-7.129	4.566	3.708
a_{332}	255.790	14.776	9.670
a_{123}	84.850	-0.980	-2.223

It must be noted that Equation (5.4) is in coded units. So, the highest points of parameters are +1, center points are 0 and the lowest points are -1 in the equation. Same transformation in previous experiments has been done to enter the parameters as feed rate, depth of cut and spindle speed in engineering units. After the transformation, the mathematic formulation became as in Equation (5.5) and the coefficients of Equation (5.4) remained same as in Table 5.16.

$$
\begin{aligned}
R &= a_0 + a_1 * [(f - 12.5)/7.5] + a_2 * [(doc - 120)/80] \\
&+ a_3 * [(S - 3500)/1500] + a_{12} * [(f - 12.5)/7.5] * [(doc - 120)/80] \\
&+ a_{13} * [(f - 12.5)/7.5] * [(S - 3500)/1500] \\
&+ a_{23} * [(doc - 120)/80] * [(S - 3500)/1500] \\
&+ a_{11} * [(f - 12.5)/7.5] * [(f - 12.5)/7.5] \\
&+ a_{22} * [(doc - 120)/80] * [(doc - 120)/80] \\
&+ a_{33} * [(S - 3500)/1500] * [(S - 3500)/1500] \\
&+ a_{112} * [(f - 12.5)/7.5] * [(f - 12.5)/7.5] * [(doc - 120)/80] \\
&+ a_{113} * [(f - 12.5)/7.5] * [(f - 12.5)/7.5] * [(S - 3500)/1500] \\
&+ a_{221} * [(S - 3500)/1500] * [(S - 3500)/1500] * [(f - 12.5)/7.5] \\
&+ a_{223} * [(doc - 120)/80] * [(doc - 120)/80] * [(S - 3500)/1500] \\
&+ a_{331} * [(S - 3500)/1500] * [(S - 3500)/1500] * [(f - 12.5)/7.5] \\
&+ a_{332} * [(S - 3500)/1500] * [(S - 3500)/1500] * [(doc - 120)/80] \\
&+ a_{123} * [(f - 12.5)/7.5] * [(doc - 120)/80] * [(S - 3500)/1500]
\end{aligned}
\tag{5.5}
$$

Lastly, the experimental study was finished by an ANOVA study as previous experiments to determine the significance of coefficients for the mathematical model. For the procedure, first of all two low value coefficients, a_{331} and a_{123}, were eliminated and the equation became as in Equation (5.6). Surface roughness was estimated by these 15 coefficients and this estimated and residual values were given in Table 5.17 in related columns.

$$
\begin{aligned}
R &= a_0 + a_1 * f + a_2 * doc + a_3 * S + a_{12} * f * doc + a_{13} * f * S \\
&+ a_{23} * doc * S + a_{11} * f * f + a_{22} * doc * doc + a_{33} * S * S \\
&+ a_{112} * f * f * doc + a_{113} * f * f * S + a_{221} * S * S * f \\
&+ a_{223} * doc * doc * S + a_{332} * S * S * doc
\end{aligned}
\tag{5.6}
$$

Table 5.17 Estimated and Residual Values for Experiment 3

	Estimated			Residual		
Run	PV (nm)	rms (nm)	R_a (nm)	PV (nm)	rms (nm)	R_a (nm)
1	1722.8	87.7	54.4	287.6	4.1	-3.7
2	3826.7	317.0	227.9	355.6	4.7	-6.4
3	1422.1	87.9	57.9	30.5	16.8	17.9
4	1699.3	107.4	72.5	112.6	14.7	1.6
5	2645.8	194.5	134.5	286.4	22.8	10.3
6	1333.5	87.7	59.1	82.9	21.9	18.4
7	2687.3	176.9	122.4	-93.8	-31.6	-25.1
8	483.8	20.6	9.7	69.9	2.9	1.2
9	116.6	59.5	34.7	-631.6	-39.9	-25.9
10	2045.9	135.8	89.0	647.4	11.9	3.3
11	601.0	36.4	22.8	-542.2	-33.1	-20.4
12	1399.6	80.7	53.1	-1125.8	-72.3	-49.0
13	2681.2	191.3	130.5	-919.6	-62.4	-42.6
14	1203.2	53.7	27.5	-604.7	-30.2	-17.2
15	3232.8	235.4	166.3	-522.6	-90.0	-72.4
16	2787.1	199.8	131.1	-44.8	14.5	6.0
17	3821.0	311.5	218.0	279.8	13.8	8.6
18	1873.8	109.6	71.2	-1025.3	-87.7	-61.7
19	1951.1	102.5	57.5	-399.4	-51.6	-39.8
20	1781.6	116.9	78.5	-937.0	-82.2	-61.9
21	1951.9	124.1	84.9	-893.6	-86.5	-66.6
22	1878.0	113.5	78.5	-246.8	-49.5	-38.5
23	4256.3	367.4	273.1	-54.6	46.0	42.1
24	967.3	50.3	31.3	-679.1	-42.1	-26.8
25	2541.3	203.0	150.4	-653.2	-57.3	-40.9
26	1499.1	93.2	63.3	-152.2	-4.5	2.5
27	2492.9	189.5	134.4	-473.2	-48.2	-29.3

As also mentioned in Section 5.3 and 5.4, sum of squares of errors, mean square of errors, root mean square of errors and standard deviation have been found to evaluate the coefficients. The table of results for three different roughness types are shown in Table 5.18.

Table 5.18 Summary of Errors and Standard Deviation for Experiment 3

	PV	rms	R_a
Sum of Squares of Errors	8355630.085	60469.964	32587.346
Mean Square of Errors	4177815.042	30234.982	16293.673
Root Mean Square of Errors	2043.970	173.882	127.647
Standard Deviation	11.303	3.297	2.825

As mentioned in previous Sections 5.3 and 5.4, t-Ratio was calculated and by using t-Ratio and freedom, which is 2 for this model, p-Value could be found out which gives idea about significance of the parameter. Table 5.19 gives the results of t-Ratio and p-Value for three different roughness types. So, as shown from the Table 5.19, a_0, a_1, a_3 and a_{13} are the most significant coefficients for surface roughness because of their low p-Value and this showed the significance of parameters feed rate and spindle speed for the process.

Table 5.19 t-Ratio and p-Value for Experiment 3

	t-Ratio			p-Value		
Coefficient	PV	rms	R_a	PV	rms	R_a
a_0	157.622	10.350	6.941	**0.00004**	**0.00921**	**0.02013**
a_1	67.488	6.160	4.564	**0.00022**	**0.02536**	**0.04481**
a_2	-4.161	-0.521	-0.182	**0.05319**	0.65431	0.87236
a_3	-55.700	-4.575	-3.214	**0.00032**	**0.04461**	**0.08469**
a_{12}	-6.656	-0.410	-0.216	**0.02184**	0.72155	0.84902
a_{13}	-18.901	-3.018	-2.365	**0.00279**	**0.09449**	0.14174
a_{23}	-1.247	-0.787	-0.883	0.33863	0.51373	0.47038
a_{11}	-4.555	0.267	0.389	**0.04497**	0.81448	0.73479
a_{22}	19.227	1.155	0.754	**0.00269**	0.36745	0.52953
a_{33}	23.897	2.006	1.395	**0.00175**	0.18269	0.29775
a_{112}	6.194	1.308	1.098	**0.02509**	0.32100	0.38674
a_{113}	-19.509	-1.680	-1.293	**0.00262**	0.23497	0.32523
a_{221}	-10.327	-0.342	-0.045	**0.00925**	0.76495	0.96820
a_{223}	-9.852	-1.171	-0.854	**0.01015**	0.36223	0.48307
a_{332}	22.631	1.307	0.856	**0.00195**	0.32128	0.48219

5.6 Three Level Box-Behnken Design for Flat Disk

In addition to Three Level Full Factorial Design, Three Level Box-Behnken Design was also performed in experimental study to compare the results of all designs realized on flat surface configuration. As mentioned in Section 5.5, instead of four, three parameters were selected as feed rate, depth of cut and spindle speed to decrease the number of cuts and therefore, 27 cuts were made for Three Level Full Factorial Design. Then, the results of 13 cuts of Experiment 3 were used for Box-Behnken Design. So, a different machining application was not performed. The order of runs and the result of measurements are shown in Table 5.20 for experimental study of Box-Behnken Design.

Table 5.20 Results of the Surface Roughness for Box-Behnken Design

Run	Run in 3^3 Full Factorial Design	Feed Rate (mm/min)	Depth of Cut (µm)	Spindle Speed (RPM)	PV (nm)	rms (nm)	R_a (nm)
1	14	5	40	3500	598.5	23.5	10.3
2	12	5	200	3500	273.7	8.4	4.1
3	5	20	40	3500	2932.1	217.2	144.8
4	25	20	200	3500	1888.1	145.7	109.4
5	16	12.5	40	2000	2742.3	214.3	137.1
6	6	12.5	40	5000	1416.3	109.6	77.5
7	15	12.5	200	2000	2710.2	145.4	93.9
8	1	12.5	200	5000	2010.3	91.8	50.7
9	18	5	120	2000	848.5	21.9	9.5
10	2	20	120	2000	4182.3	321.7	221.5
11	11	5	120	5000	58.8	3.3	2.5
12	4	20	120	5000	1812.0	122.1	74.2
13	20	12.5	120	3500	844.6	34.7	16.6

The mathematical formulation, found by Three Level Box-Behnken Design, is in the form like in Equation (5.7). There were 10 coefficients from a_0 to a_{33} that had to be calculated and equations for coefficients had been obtained from the software of JMP® 8 and results are given in Table 5.21 for PV, rms and R_a roughness types.

$$\begin{aligned} R &= a_0 + a_1 * f + a_2 * doc + a_3 * S + a_{12} * f * doc + a_{13} * f * S \\ &+ a_{23} * doc * S + a_{11} * f * f + a_{22} * doc * doc + a_{33} * S * S \end{aligned} \tag{5.7}$$

Where;

R: Roughness

f: Feed rate

doc: Depth of cut

Table 5.21 Coefficients for Roughness Equation (5.7) for Box-Behnken Design

Coefficient	PV	rms	R_a
a_0	844.620	34.653	16.579
a_1	1129.363	93.701	65.450
a_2	-100.868	-21.669	-13.944
a_3	-648.227	-47.071	-32.161
a_{12}	-179.818	-14.129	-7.321
a_{13}	-395.152	-45.250	-35.072
a_{23}	156.536	12.790	4.095
a_{11}	42.056	20.514	18.853
a_{22}	536.447	43.526	31.729
a_{33}	838.714	62.087	41.485

Same as with previous experimental studies, Equation (5.7) is in coded units and it is transformed to engineering units in Equation (5.8). Therefore, feed rate, depth of cut and spindle speed can be entered in engineering units to the mathematical formulation to estimate the surface roughness. However, this transformation did not change the coefficients given in Table 5.21.

$$
\begin{aligned}
R &= a_0 + a_1 * [(f - 12.5)/7.5] + a_2 * [(doc - 120)/80] \\
&+ a_3 * [(S - 3500)/1500] \\
&+ a_{12} * [(f - 12.5)/7.5] * [(doc - 120)/80] \\
&+ a_{13} * [(f - 12.5)/7.5] * [(S - 3500)/1500] \\
&+ a_{23} * [(doc - 120)/80] * [(S - 3500)/1500] \\
&+ a_{11} * [(f - 12.5)/7.5] * [(f - 12.5)/7.5] \\
&+ a_{22} * [(doc - 120)/80] * [(doc - 120)/80] \\
&+ a_{33} * [(S - 3500)/1500] * [(S - 3500)/1500]
\end{aligned}
\tag{5.8}
$$

Lastly, with an ANOVA study, the experimental study was completed similar to previous experiments to determine the significance of parameters for the mathematical model. To fulfill that task, first of all low value coefficients, which were a_{11} and a_{23}, had been eliminated from the mathematical formulation as shown in Equation (5.9) and surface roughness estimation has been performed by this equation. The estimated values and difference between the real and estimated values can be seen in related columns in Table 5.22.

$$
\begin{aligned}
R &= a_0 + a_1 * f + a_2 * doc + a_3 * S + a_{12} * f * doc + a_{13} * f * S \\
&+ a_{22} * doc * doc + a_{33} * S * S
\end{aligned}
\tag{5.9}
$$

Table 5.22 Estimated and Residual Values for Box-Behnken Design

	Estimated			Residual		
Run	PV (nm)	rms (nm)	R_a (nm)	PV (nm)	rms (nm)	R_a (nm)
1	172.8	-8.0	-10.5	425.8	31.5	20.8
2	330.7	-23.1	-23.8	-56.9	31.5	27.9
3	2791.1	207.7	135.0	141.0	9.6	9.8
4	2229.7	136.1	92.5	-341.6	9.6	16.9
5	2968.9	209.0	135.9	-226.6	5.3	1.2
6	1672.4	114.9	71.6	-256.1	-5.3	5.9
7	2767.1	165.7	108.0	-57.0	-20.3	-14.1
8	1470.7	71.5	43.7	539.7	20.3	7.0
9	807.0	4.9	-10.3	41.5	17.0	19.8
10	3856.1	282.8	190.7	326.2	38.9	30.8
11	300.9	1.2	-4.5	-242.1	2.1	6.9
12	1769.3	98.1	56.3	42.6	24.0	17.9
13	844.6	34.7	16.6	0.0	0.0	0.0

As mentioned in Section 5.3 and 5.4, sum of squares of errors, mean square of errors, root mean square of errors and standard deviation for Box-Behnken Design have been found for the calculation of p-Value to evaluate the coefficients. The table of results for three different roughness types were given in Table 5.23.

Table 5.23 Summary of Errors and Standard Deviation for Box-Behnken Design

	PV	rms	R_a
Sum of Squares of Errors	901064.984	5426.945	3583.139
Mean Square of Errors	450532.492	2713.472	1791.570
Root Mean Square of Errors	671.217	52.091	42.327
Standard Deviation	237.311	18.417	14.965

Like as the previous sections, t-Ratio was calculated and by using t-Ratio and freedom, which is 2 for this model, p-Value could be found out. Table 5.24 gives the results of t-Ratio and p-Value for three different roughness types. So, as shown from the Table 5.24, a_1 and a_{33} are the most significant coefficients for surface roughness because of their low p-Value and this showed the significance of parameters feed rate and spindle speed for the relationship between surface roughness and machining parameters.

Table 5.24 t-Ratio and p-Value for Box-Behnken Design

	t-Ratio			p-Value		
Coefficient	PV	rms	R_a	PV	rms	R_a
a_0	3.559	1.882	1.108	**0.07068**	0.20055	0.38327
a_1	4.759	5.088	4.374	**0.04143**	**0.03653**	**0.04850**
a_2	-0.425	-1.177	-0.932	0.71220	0.36030	0.44973
a_3	-2.732	-2.556	-2.149	0.11193	0.12500	0.16465
a_{12}	-0.758	-0.767	-0.489	0.52759	0.52325	0.67321
a_{13}	-1.665	-2.457	-2.344	0.23783	0.13331	0.14377
a_{22}	2.261	2.363	2.120	0.15219	0.14193	0.16811
a_{33}	3.534	3.371	2.772	**0.07158**	**0.07786**	0.10923

5.7 Comparison of Experimental Designs

As mentioned before in related sections, 2 Level Full Factorial Design was performed for flat disk and convex lens to make comparison of roughness between different surface configurations. It can be concluded that mostly flat configuration obtained lower surface roughness values when compared with convex one by evaluating the results in experimental studies. Actually, different configurations were not expected to have different surface finish values. This may be a result of higher lateral forces affected PCD insert during the machining of convex surface when compared with the flat one, however cutting forces are generally low during diamond turning. Also, vibrations on lens may be another result since lens with 12 scale factor have been machined so, vibrations can affect surface finish at a higher extent during the machining of convex lens. If lens with higher center thickness were used, it was expected to have lower surface finish difference between these configurations.

2 and 3 Level Full Factorial Designs and Box-Behnken Experimental Design have been performed for the machining of flat germanium disk and mathematical models have been obtained as a result of these experimental designs. The studies with flat disk were performed to make comparison between mathematical models and make best estimation of surface roughness at the selected machining parameters.

Five surface roughness results have been predicted by mathematical models for flat disk configuration. The parameters were generally selected between upper and lower limits excepting rake angle. In only 2 Level Full Factorial Design, rake angle had been a parameter so, always tool with -25^{o} rake angle was used for prediction to make comparison between design of experiments. The cutting parameters that the machining was performed, predicted and measured rms roughness values and errors in the predictions are shown in Table 5.25.

Table 5.25 Error of Mathematical Models of Experimental Designs

Prediction	f (mm/min)	doc (μm)	S (RPM)	r (°)	Measured rms Roughness (nm)	Design of Experiment	Predicted rms Roughness (nm)	Error (%)
1	15	150	4000	-25	57.5	2^4 Full Factorial	101.6	76.70
						3^3 Full Factorial	119.8	108.37
						Box-Behnken	52.2	9.30
2	15	250	2000	-25	216.2	2^4 Full Factorial	227.8	5.40
						3^3 Full Factorial	325.5	50.59
						Box-Behnken	243.7	12.74
3	17.5	100	3000	-25	137.7	2^4 Full Factorial	166.8	21.10
						3^3 Full Factorial	195.6	41.97
						Box-Behnken	157.4	14.30
4	10	60	2000	-25	115.6	2^4 Full Factorial	144.4	24.88
						3^3 Full Factorial	157.8	36.45
						Box-Behnken	146.6	26.78
5	12.5	40	2000	-25	206.7	2^4 Full Factorial	165.5	19.94
						3^3 Full Factorial	199.9	3.29
						Box-Behnken	221.8	7.32

According to the study shown in Table 5.25, Box-Behnken Experimental Design with three parameters has given the best predictions having less than 26.78 % error in five examples. While Three Level Full Factorial Design with three parameters has performed the worst predictions with even more than 100 % errors in one example. Actually, it was expected that Three Level Full Factorial Design executes more successful predictions than Two Level Full Factorial Design because of performing extra runs between parameter limits.

As mentioned in Section 5.2, it is enough to have surface roughness of generated blanks after rough cutting and in these five examples, rms roughness was far below

800-850 nm which is typical rms roughness of generated blanks purchased from suppliers. So, these surfaces were good enough for rough cutting. However, predictions of mathematical models were not successful enough. Actually, it was an expected result since roughness of surfaces, cut at same machining conditions, had changed in high altitude in different experimental designs which were performed with different PCD inserts having same geometry.

There were eight runs having same machining conditions in 2^4 and 3^3 Full Factorial Designs, the results of which were shared in Section 5.3 and 5.5. The change in rms roughness of surface machined with same machining conditions varies between 20.96% and 83.94% at these eight runs. That high altitude changes were also realized with the same insert. For instance, tenth run in 3^3 Full Factorial Design, which was executed at 12.5 mm/min feed rate, 40 µm depth of cut, 3500 RPM spindle speed with -25^o rake angle tool, was performed again after the experiment with same insert. Rms roughness was measured as 83.6 nm which was 43.43 % better than the previous. A number of cuttings have been performed between these two machining applications so insert got worn between these cuts. Therefore, it could be thought that this high difference can be as a result of worn tool. However, one more cutting were performed at the same machining conditions and rms roughness were measured as 113.5 nm which was % 26.36 worse than the previous one.

Flat germanium surface was cut off twice by MCD tool after cutting by PCD tool at the same machining conditions as 12.5 mm/min feed rate, 40 µm depth of cut, 3500 RPM spindle speed and the rms roughness of surface was measured 2.8 and 2.6 nm, respectively. So, the change has been 6.10 %. Therefore, high altitude change of roughness, between 20.96 to 83.94 %, was only related with PCD tool and this has made the predictions of surface roughness by mathematical models obtained by experimental designs really tough.

Hence, mathematical models have been modified to make worst case prediction by calculating the standard deviation of rms roughness of germanium surfaces machined by PCD tools. To achieve this, nine machining runs were performed at the same machining conditions for all experiments. For 2^4 Full Factorial Designs which had been performed for flat disk and convex lens, 3. run was selected with 5 mm/min feed rate, 200 μm depth of cut, 2000 RPM spindle speed with -25^o rake angle tool because roughness values measured at that run were close the average roughness of 16 runs. For 3^3 Full Factorial and Box-Behnken Designs, 20. run of 3^3 Full Factorial Design, which is 13. run of Box-Behnken Design, was selected with 12.5 mm/min feed rate, 120 μm depth of cut and 3500 RPM spindle speed machining parameters which are the center of parameter limits.

5.7.1 Worst Case Prediction of 2^4 Full Factorial Design for Flat Disk

Rms roughness of surfaces which have been re-machined with 5 mm/min feed rate, 200 μm depth of cut, 2000 RPM spindle speed with -25^o rake angle tool, same as 3. run of 2^4 Full Factorial Design, are shown in Table 5.26 and Figure 5.5 shows the distribution of rms roughness at these runs. According to results in Table 5.26, rms roughness has varied between 75.2 and 122.1 nm while 114.8 nm had been measured in Experiment 1. Therefore, the mean (μ) and standard deviation (σ) of these 10 runs including the run in Experiment 1 became 104.7 nm and 13.9 nm, respectively.

Therefore, the mathematical formulation of Experiment 1 has been modified by considering Gaussian distribution shown in Figure 5.6 and to encompass 99.73% of the distribution, μ+3σ has been accepted the highest limit of worst case which became 146.5 nm. So, the difference between worst case and the result in Experiment 1 became 27.61%. Therefore, Equation (5.2) has been modified by multiplying the formula with 1.2761 while the coefficients remained same and the result is shown in Equation (5.10). Hence, the predictions in Equation (5.10) are the worst case so, it can be mentioned that actual rms roughness will be always lower than the value estimated by that equation.

Table 5.26 Re-machining of 3. Run of 2^4 Full Factorial Design for Flat Disk

Run	f (mm/min)	doc (μm)	S (RPM)	r (°)	rms (nm)
Experiment	5	200	2000	-25	**114.8**
1	5	200	2000	-25	75.2
2	5	200	2000	-25	112.8
3	5	200	2000	-25	122.1
4	5	200	2000	-25	105.2
5	5	200	2000	-25	112.3
6	5	200	2000	-25	100.5
7	5	200	2000	-25	109.5
8	5	200	2000	-25	107.6
9	5	200	2000	-25	87.3

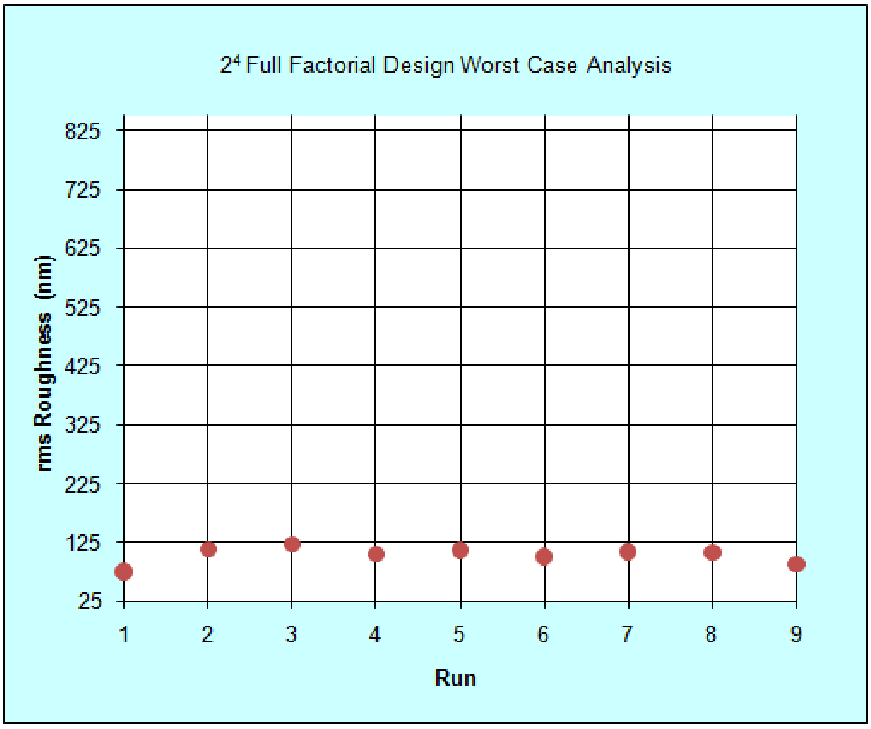

Figure 5.5 rms Roughness Distribution of 9 Runs in Experiment 1

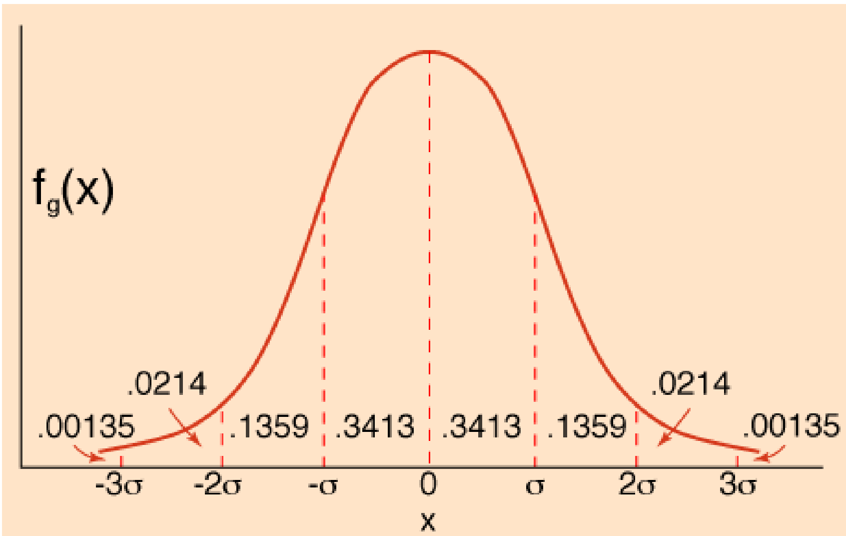

Figure 5.6 Gaussian Distribution [69]

$$
\begin{aligned}
R = 1.2761 * \{ & a_0 + a_1 * [(f - 12.5)/7.5] + a_2 * [(doc - 120)/80] \\
& + a_3 * [(S - 3500)/1500] + a_4 * [(r - (-35))/-10] \\
& + a_{12} * [(f - 12.5)/7.5] * [(doc - 120)/80] \\
& + a_{13} * [(f - 12.5)/7.5] * [(S - 3500)/1500] \\
& + a_{14} * [(f - 12.5)/7.5] * [(r - (-35))/-10] \\
& + a_{23} * [(doc - 120)/80] * [(S - 3500)/1500] \\
& + a_{24} * [(doc - 120)/80] * [(r - (-35))/-10] \\
& + a_{34} * [(S - 3500)/1500] * [(r - (-35))/-10] \\
& + a_{123} * [(f - 12.5)/7.5] * [(doc - 120)/80] * [(r - (-35))/-10] \\
& + a_{124} * [(f - 12.5)/7.5] * [(doc - 120)/80] * [(r - (-35))/-10] \\
& + a_{134} * [(f - 12.5)/7.5] * [(S - 3500)/1500] * [(r - (-35))/-10] \\
& + a_{234} * [(doc - 120)/80] * [(S - 3500)/1500] * [(r - (-35))/-10] \\
& + a_{1234} * [(f - 12.5)/7.5] * [(doc - 120)/80] * \\
& [(S - 3500)/1500] * [(r - (-35))/-10] \}
\end{aligned}
\tag{5.10}
$$

5.7.2 Worst Case Prediction of 2^4 Full Factorial Design for Convex Lens

Similar application has been performed for convex lens. Rms roughness of surfaces, which have been cut again in machining parameters same as 3. run of 2^4 Full Factorial Design, are shown in Table 5.27 and Figure 5.7 shows the distribution of rms roughness at 9 runs. According to results in Table 5.27, rms roughness has varied between 131.5 and 208.7 nm while 186.3 nm had been measured in Experiment 2. Therefore, μ and σ of these 10 runs including the run in Experiment 2 became 175.0 nm and 27.5 nm, respectively.

Therefore, the mathematical formulation of Experiment 2 has been modified by considering Gaussian distribution and to encompass 99.73% of the distribution, $\mu+3\sigma$ has been accepted the highest limit of worst case which became 257.5 nm in this case. So, the difference between worst case and the result in Experiment 2 became 38.21%. Therefore, Equation (5.2) has been modified by multiplying the formula with 1.3821 while the coefficients remained same and the result is shown in Equation (5.11). Hence, the predictions in Equation (5.11) are the worst case so, it can be mentioned that actual rms roughness will be always lower than the value estimated by that equation.

Table 5.27 Re-machining of 3. Run of 2^4 Full Factorial Design for Convex Lens

Run	f (mm/min)	doc (μm)	S (RPM)	r (^{o})	rms (nm)
Experiment	5	200	2000	-25	**186.3**
1	5	200	2000	-25	185.7
2	5	200	2000	-25	208.7
3	5	200	2000	-25	148.0
4	5	200	2000	-25	172.1
5	5	200	2000	-25	182.8
6	5	200	2000	-25	201.5
7	5	200	2000	-25	136.1
8	5	200	2000	-25	131.5
9	5	200	2000	-25	197.6

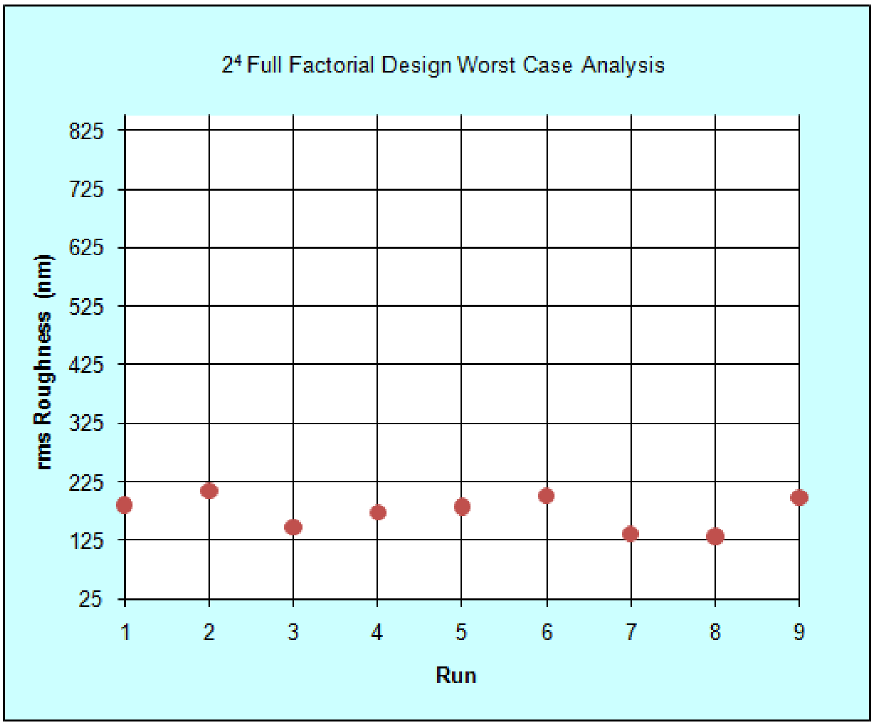

Figure 5.7 rms Roughness Distribution of 9 Runs in Experiment 2

$$
\begin{aligned}
R = 1.3821 * \{ & a_0 + a_1 * [(f - 12.5)/7.5] + a_2 * [(doc - 120)/80] \\
& + a_3 * [(S - 3500)/1500] + a_4 * [(r - (-35))/-10] \\
& + a_{12} * [(f - 12.5)/7.5] * [(doc - 120)/80] \\
& + a_{13} * [(f - 12.5)/7.5] * [(S - 3500)/1500] \\
& + a_{14} * [(f - 12.5)/7.5] * [(r - (-35))/-10] \\
& + a_{23} * [(doc - 120)/80] * [(S - 3500)/1500] \\
& + a_{24} * [(doc - 120)/80] * [(r - (-35))/-10] \\
& + a_{34} * [(S - 3500)/1500] * [(r - (-35))/-10] \\
& + a_{123} * [(f - 12.5)/7.5] * [(doc - 120)/80] * [(r - (-35))/-10] \\
& + a_{124} * [(f - 12.5)/7.5] * [(doc - 120)/80] * [(r - (-35))/-10] \\
& + a_{134} * [(f - 12.5)/7.5] * [(S - 3500)/1500] * [(r - (-35))/-10] \\
& + a_{234} * [(doc - 120)/80] * [(S - 3500)/1500] * [(r - (-35))/-10] \\
& + a_{1234} * [(f - 12.5)/7.5] * [(doc - 120)/80] * \\
& [(S - 3500)/1500] * [(r - (-35))/-10] \}
\end{aligned} \tag{5.11}
$$

5.7.3 Worst Case Prediction of 3^3 Full Factorial Design for Flat Disk

Similar application has been performed for 3^3 Full Factorial Design for flat disk. Rms roughness of surfaces, which have been cut in machining parameters same as 20. run of 3^3 Full Factorial Design, are shown in Table 5.28 and Figure 5.8 shows the distribution of rms roughness at 9 runs. According to results in Table 5.28, rms roughness has varied between 33.5 and 56.6 nm while 34.7 nm had been measured in Experiment 3. Therefore, μ and σ of these 10 runs including the run in Experiment 3 became 46.7 nm and 8.3 nm, respectively.

Therefore, the mathematical formulation of Experiment 3 has been modified by considering Gaussian distribution and to encompass 99.73% of the distribution, $\mu+3\sigma$ has been accepted the highest limit of worst case as in previous sections which became 71.7 nm in this case. So, the difference between worst case and the result in Experiment 3 became 107%. Therefore, Equation (5.5) has been modified by multiplying the formula with 2.07 while the coefficients remained same and the result is shown in Equation (5.12). Hence, the predictions in Equation (5.12) are the worst case so, it can be mentioned that actual rms roughness will be always lower than the value estimated by that equation.

Table 5.28 Re-machining of 20. Run of 3^3 Full Factorial Design for Flat Disk

Run	f (mm/min)	doc (µm)	S (RPM)	r (°)	rms (nm)
Experiment	12.5	120	3500	-25	**34.7**
1	12.5	120	3500	-25	56.0
2	12.5	120	3500	-25	45.3
3	12.5	120	3500	-25	47.5
4	12.5	120	3500	-25	55.7
5	12.5	120	3500	-25	33.5
6	12.5	120	3500	-25	56.6
7	12.5	120	3500	-25	50.2
8	12.5	120	3500	-25	41.6
9	12.5	120	3500	-25	46.0

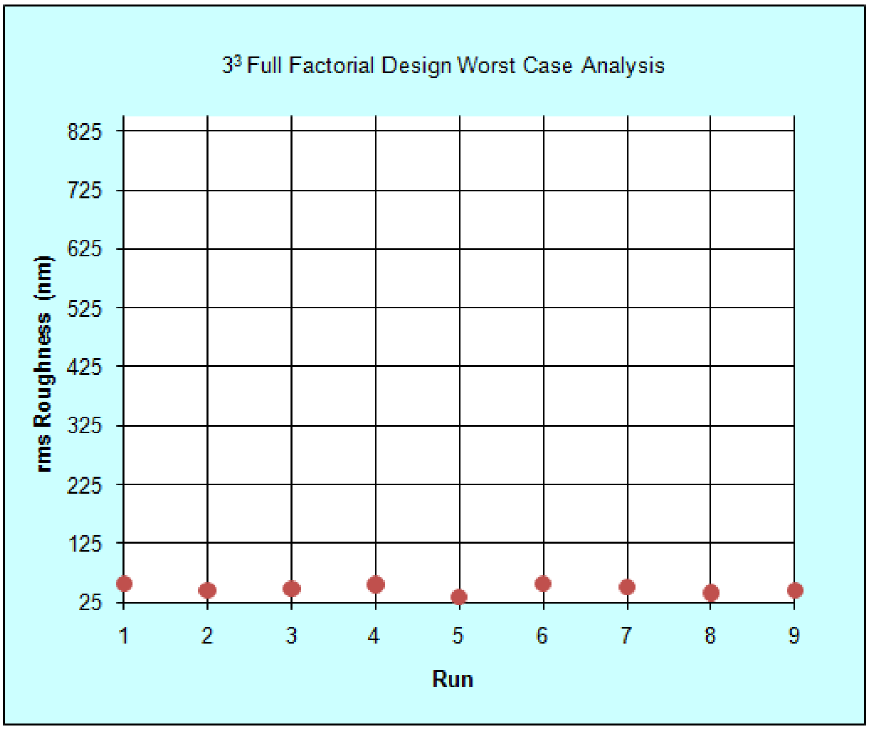

Figure 5.8 rms Roughness Distribution of 9 Runs in Experiment 3

$$
\begin{aligned}
R = 2.07 * \{ & a_0 + a_1 * [(f - 12.5)/7.5] + a_2 * [(doc - 120)/80] \\
& + a_3 * [(S - 3500)/1500] + a_{12} * [(f - 12.5)/7.5] * [(doc - 120)/80] \\
& + a_{13} * [(f - 12.5)/7.5] * [(S - 3500)/1500] \\
& + a_{23} * [(doc - 120)/80] * [(S - 3500)/1500] \\
& + a_{11} * [(f - 12.5)/7.5] * [(f - 12.5)/7.5] \\
& + a_{22} * [(doc - 120)/80] * [(doc - 120)/80] \\
& + a_{33} * [(S - 3500)/1500] * [(S - 3500)/1500] \\
& + a_{112} * [(f - 12.5)/7.5] * [(f - 12.5)/7.5] * [(doc - 120)/80] \\
& + a_{113} * [(f - 12.5)/7.5] * [(f - 12.5)/7.5] * [(S - 3500)/1500] \\
& + a_{221} * [(S - 3500)/1500] * [(S - 3500)/1500] * [(f - 12.5)/7.5] \\
& + a_{223} * [(doc - 120)/80] * [(doc - 120)/80] * [(S - 3500)/1500] \\
& + a_{331} * [(S - 3500)/1500] * [(S - 3500)/1500] * [(f - 12.5)/7.5] \\
& + a_{332} * [(S - 3500)/1500] * [(S - 3500)/1500] * [(doc - 120)/80] \\
& + a_{123} * [(f - 12.5)/7.5] * [(doc - 120)/80] * [(S - 3500)/1500] \}
\end{aligned}
\tag{5.12}
$$

5.7.4 Worst Case Prediction of Box-Behnken Design for Flat Disk

20. run of 3^3 Full Factorial Design was also 13. run of Box-Behnken Design so, re-machining results could be also used to modify the formula for the worst case prediction of Box-Behnken Design for flat disk. As mentioned in Section 5.7.3, rms roughness has varied between 33.5 and 56.6 nm while 34.7 nm rms roughness had been measured in Experiment 3 so, the difference between worst case according to Gaussian distribution and the result in Experiment 3 became 107%. Therefore, Equation (5.8) has been modified by multiplying the formula with 2.07 while the coefficients remained same and the result is shown in Equation (5.13). Hence, the predictions in Equation (5.13) are the worst case so, it can be mentioned that actual rms roughness will be always lower than the value estimated by that equation.

$$
\begin{aligned}
R = 2.07 * \{a_0 &+ a_1 * [(f - 12.5)/7.5] + a_2 * [(doc - 120)/80] \\
&+ a_3 * [(S - 3500)/1500] + a_{12} * [(f - 12.5)/7.5] * [(doc - 120)/80] \\
&+ a_{13} * [(f - 12.5)/7.5] * [(S - 3500)/1500] \\
&+ a_{23} * [(doc - 120)/80] * [(S - 3500)/1500] \\
&+ a_{11} * [(f - 12.5)/7.5] * [(f - 12.5)/7.5] \\
&+ a_{22} * [(doc - 120)/80] * [(doc - 120)/80] \\
&+ a_{33} * [(S - 3500)/1500] * [(S - 3500)/1500]\}
\end{aligned} \tag{5.13}
$$

CHAPTER 6

DISCUSSION AND CONCLUSION OF THE EXPERIMENTAL STUDY

6.1 Introduction

In addition to mathematical models and ANOVA studies, some conclusions were made about the relationship between various parameters and surface roughness by making use of the experimental results. Also, by making measurements on the machined surfaces at three different points in the experimental study with three parameters, the relationship between cutting speed and surface roughness were obtained. The transmission and reflection of the light from the machined surface were analyzed and results were given in this chapter. Moreover, wear of polycrystalline diamond tool and recommendations for future work were mentioned at the end of the chapter.

6.2 Influence of Cutting Parameters

In this section, the influence of cutting parameters namely feed rate, depth of cut, spindle speed and tool geometry parameters namely rake and clearance angles and cutting speed were evaluated against roughness of machined germanium surfaces.

During the studies, spindle speed, depth of cut and feed rate were selected between 2000-5000 RPM, 40-200 μm and 5-20 mm/min respectively as machining conditions and rake angle was between -25^o and -45^o as a tool geometry parameter. Therefore, conclusions made in Chapter 6 have been made at these circumstances.

6.2.1 Influence of Feed Rate

The experimental studies had shown that feed rate was really effective on the surface roughness. This has also been observed during ANOVA studies. Coefficient a_1 was always an effective parameter that shows the influence of feed rate on roughness of optical surfaces. As mentioned in Chapter 2, feed rate affects the critical chip thickness which is an important parameter for ductile to brittle transition. As evaluated before, critical chip thickness forms at a higher depth from the surface when feed rate increases, so pitting occurs on the machined surface and surface roughness increases [24].

For the three main experiments mentioned in Chapter 5, the change of rms roughness according to feed rate was analyzed while other parameters were kept constant. For 2^4 Full Factorial Design studies with flat disk and convex lens, surface roughness change at maximum and minimum limits of the feed rate was evaluated. As shown in Figures 6.1 and 6.2, run numbers at the right of the graphs show the order of machining where feed rate changed and the other parameters were constant. The same system was arranged for 3^3 Full Factorial Design, in which in addition to maximum and minimum limits of feed rate, center point of limits was analyzed and as shown in Figure 6.3, there were three runs that had constant parameters except feed rate and they were also mentioned at the right of the graph.

As seen in Figures 6.1 and 6.2, as feed rate increased from minimum to maximum limit, the roughness of the surface also increased. The same trend was seen in

Figure 6.3. Therefore, during rough cutting of germanium with polycrystalline diamond tools, surface roughness increased with the increase in feed rate in the circumstances selected in experimental studies.

However, some exceptions were also observed as shown in Figure 6.3, where the machining was also performed at the middle point of the maximum and minimum limits of feed rate. In one example, surface roughness was lower at 12.5 mm/min feed rate when compared to the one at 5 mm/min. Moreover, surface roughness was lower at 20 mm/min feed rate when compared to the one at 12.5 mm/min. However, these results were exceptions and they were a result of difference in surface roughness values realized in Section 5.7.

Figure 6.1 Change in Surface Roughness with Feed Rate in Experiment 1

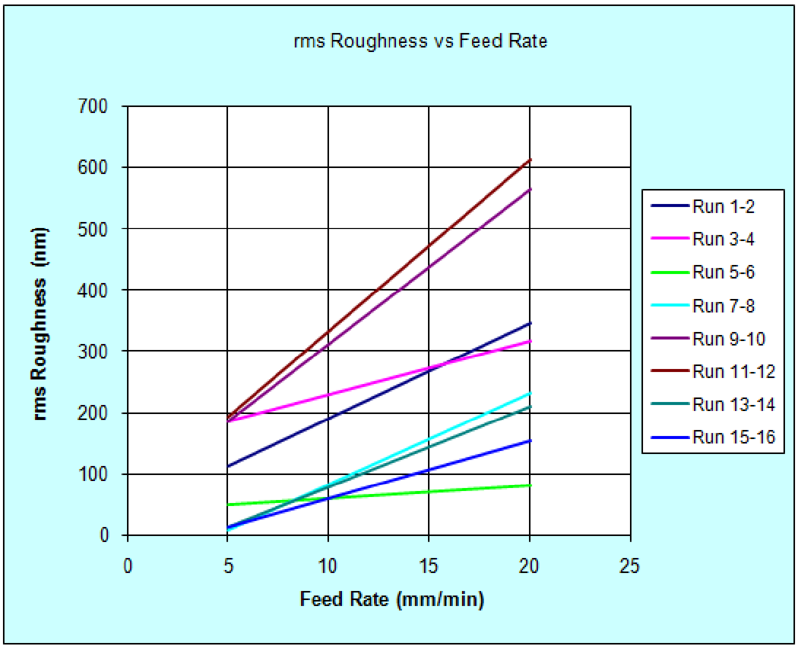

Figure 6.2 Change in Surface Roughness with Feed Rate in Experiment 2

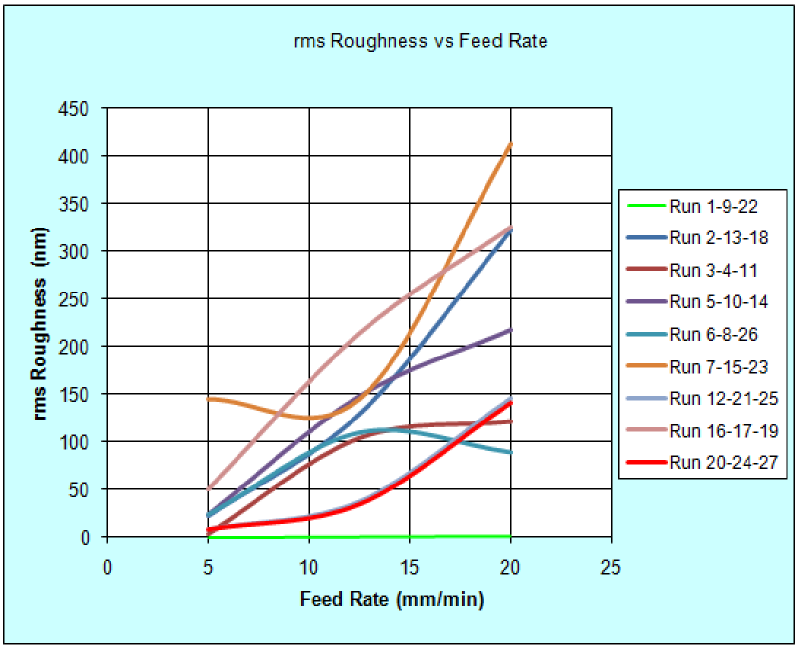

Figure 6.3 Change in Surface Roughness with Feed Rate in Experiment 3

6.2.2 Influence of Depth of Cut

Similar to the influence of feed rate, effect of depth of cut to surface roughness was analyzed. During the ANOVA studies, p-Value of coefficient a_2 was always big for all experimental studies when compared with the coefficients a_1, a_3 and a_4. This means the effect of depth of cut was less significant than the other parameters.

For the three main experiments mentioned in Chapter 5, the change of rms roughness according to depth of cut was analyzed when the other parameters were kept constant. For the 2^4 Full Factorial Design studies with flat disk and convex lens, at maximum and minimum limits of the depth of cut change were evaluated. Similar to Section 6.2 run numbers, at the right of Figures 6.4 and 6.5 shows the order of machining where depth of cut changed and the other parameters were constant. The same system was arranged for 3^3 Full Factorial Design, in which in addition to maximum and minimum limits of depth of cut, center point of limits were analyzed and as shown from Figure 6.6, there were three runs that had constant parameters except depth of cut and they were also mentioned on the right of the graph.

Figure 6.4 Change in Surface Roughness with Depth of Cut in Experiment 1

Figure 6.5 Change in Surface Roughness with Depth of Cut in Experiment 2

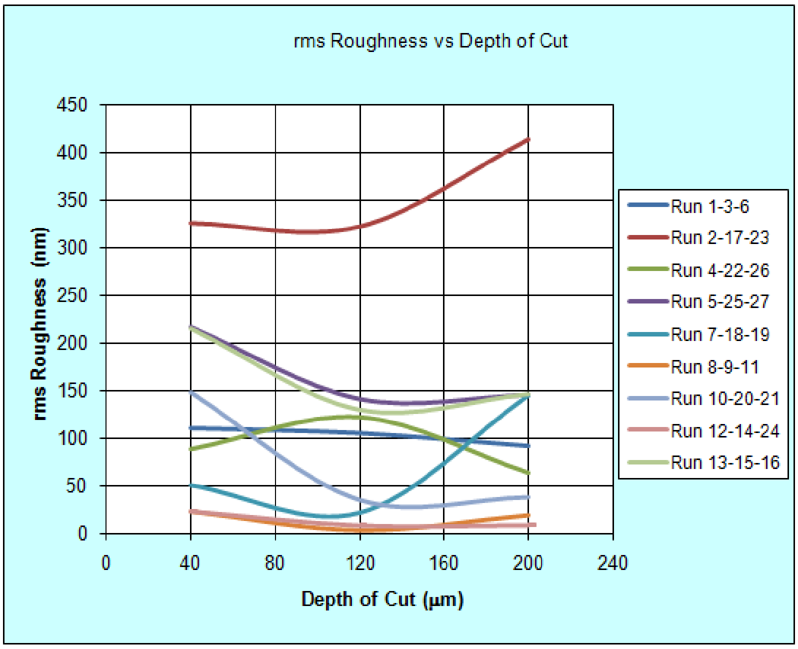

Figure 6.6 Change in Surface Roughness with Depth of Cut in Experiment 3

As shown in Figures 6.4, 6.5 and 6.6, surface roughness has not shown a definite characteristic with the change in depth of cut and generally negligible differences were observed at the circumstances selected in experimental studies. In some runs of experimental studies, surface roughness increased while depth of cut increased however, in some others the opposite has been experienced. The indefinite characteristic was also seen in 3^3 Full Factorial Design. The surface, which was machined in the middle point of limits of depth of cut, had sometimes maximum and sometimes minimum rms roughness. This negligible effect of depth of cut was expected since as obtained from ANOVA studies, depth of cut was not an effective parameter for surface roughness and the results were affected more by the parameters.

6.2.3 Influence of Spindle Speed

ANOVA studies performed at the end of experiments had shown that spindle speed was really effective on the surface roughness since coefficients a_3 and a_{13} have always had small p-Value. These results were also confirmed by the graphs, in which rms roughness values were analyzed according to spindle speed for constant feed rate, depth of cut and rake angle.

For the 2^4 Full Factorial Design studies with flat disk and convex lens, surface roughness was evaluated at the maximum and minimum limits of the spindle speed. As shown in Figures 6.7 and 6.8, run numbers at the right of the figures show the order of machining where spindle speed changed and the other parameters were constant. Therefore, the same system was arranged for 3^3 Full Factorial Design and in addition to maximum and minimum limits of spindle speed, machining was performed at the center point of these limits as shown in Figure 6.9.

As seen from Figure 6.7 and 6.8, as spindle speed increased from minimum to maximum limit, surface roughness decreased in the circumstances selected in experimental studies. This conclusion was also pointed out in the study of Çalı and it was mentioned that raising the spindle speed affected the roughness in a good manner [18]. Moreover, Figure 6.9 gave chance to compare surface roughness at center point of limits of spindle speed and it was shown that in some cases, rms roughness was lower at 3500 RPM spindle speed when compared to roughness at 5000 RPM. However, these results were exceptions and they were a result of difference in surface roughness values realized in Section 5.7.

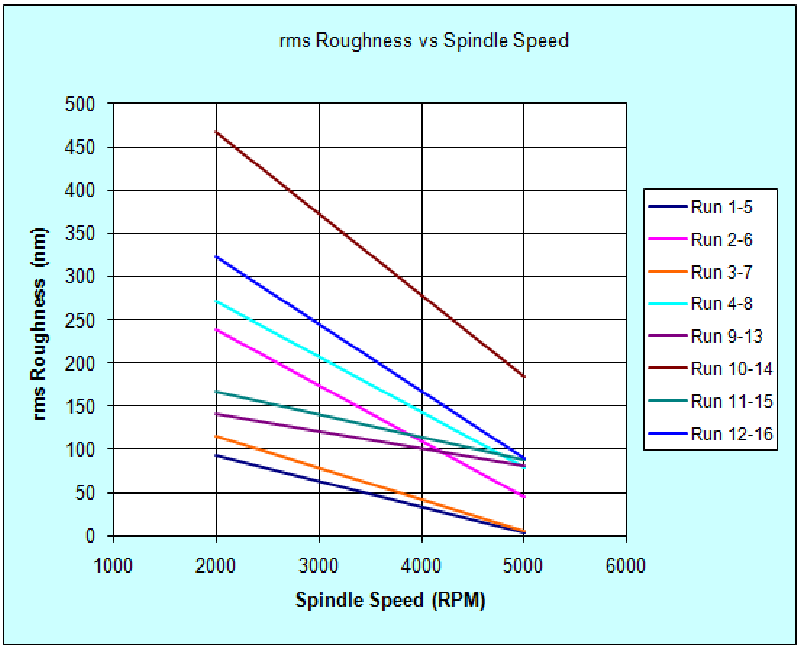

Figure 6.7 Change in Surface Roughness with Spindle Speed in Experiment 1

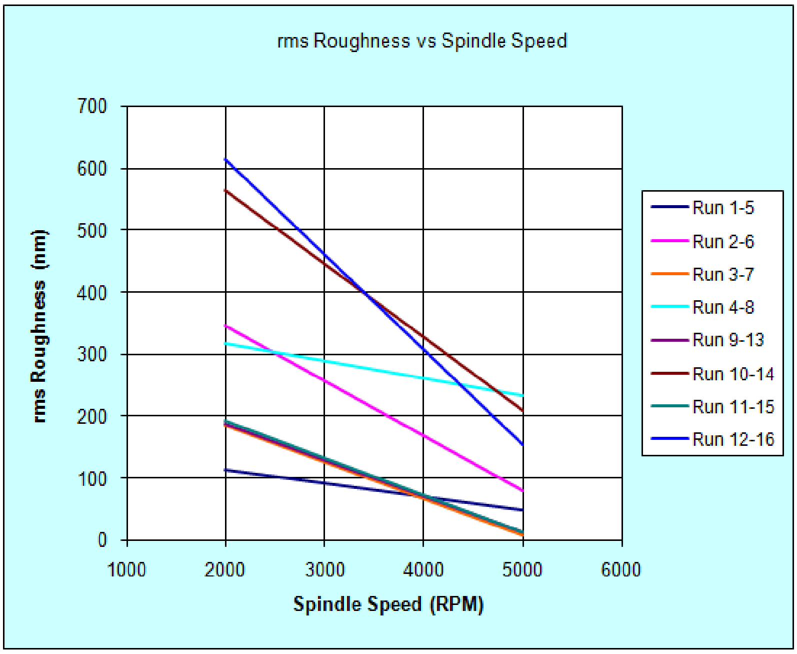

Figure 6.8 Change in Surface Roughness with Spindle Speed in Experiment 2

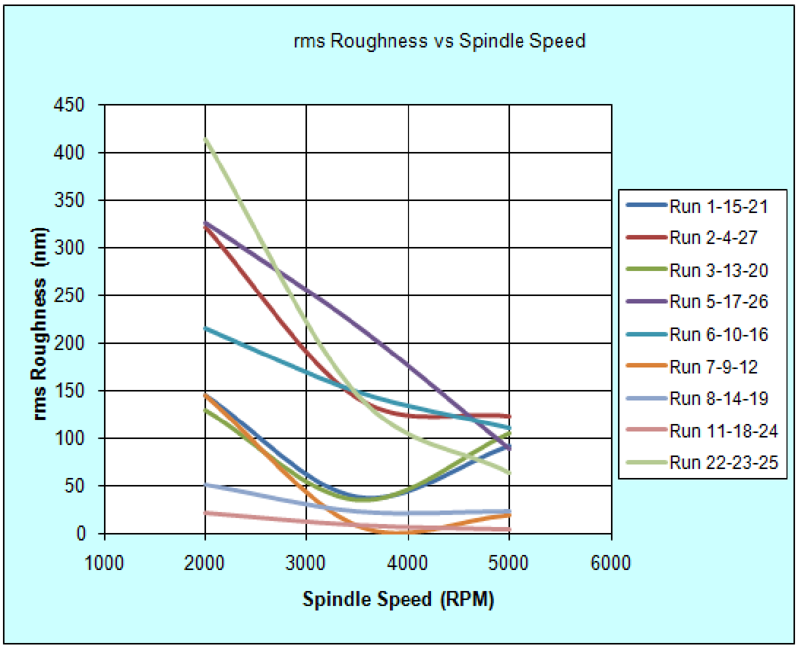

Figure 6.9 Change in Surface Roughness with Spindle Speed in Experiment 3

6.2.4 Influence of Rake and Clearance Angle

As mentioned before, effect of rake angle was evaluated for flat disk and convex lens in 2^4 Full Factorial Design studies and -25^o rake angle tool has 36^o clearance angle while -45^o rake angle tool has 56^o clearance angle. Therefore, the effect was not only related with rake angle, the effect of clearance angle was also included. ANOVA studies had shown that rake angle was really effective on the surface roughness since coefficient a_4 has always had small p-Value in experiments with flat disk and convex lens. These results were also confirmed from the graphs, in which rms roughness were analyzed according to the rake and clearance angles for constant feed rate, depth of cut and spindle speed. As shown in Figures 6.10 and 6.11, run numbers at the right of graph show the order of machining where rake and clearance angles changed and the other parameters were constant.

In most of the previous studies, large negative rake angle tools were mentioned to be preferable because they produce a compressive stress state in front of the tool edge so, that stress prevents creation and propagation of cracks. However, there is a trade off for each material to which extend that the negative rake angle could be increased since further increase results higher tool wear as mentioned in the study of Patten et. al [70]. In that study, single crystal silicon carbide was machined by mono-crystalline diamond tool in a diamond turning machine and -45^{o} rake angle tool was indicated as optimal tool for ductile machining conditions. Since, less-negative rake angle tools could not constitute high pressure for ductile machining while more-negative rake angle tools increased cutting forces which leads to tool wear. Meanwhile, in another study, Fang et. al [71] mentioned that a negative rake angle tool with large edge radius will have much more effective negative rake angle and this could harm the machined surface. Thus, in that study, 0^{o} rake angle tool was specified to produce better surface finish when compared with -25^{o} rake angle tool.

In experimental studies mentioned in Chapter 5, when rake angle was increased from -25^{o} to -45^{o}, the surface roughness increased in machined flat surfaces as shown in Figure 6.10. Therefore, with -25^{o} rake angle polycrystalline diamond tool, better surface finish values have been gathered for the machining of flat disk in the circumstances selected in the experimental studies. However, some exceptions have been obtained at rms roughness values for convex lens that more-negative rake angle tool resulted better surface finish as shown in Figure 6.11. However, generally surface roughness increased when rake angle was increased from -25^{o} to -45^{o}. Thus, these exceptions were a result of difference in surface roughness values realized in Section 5.7

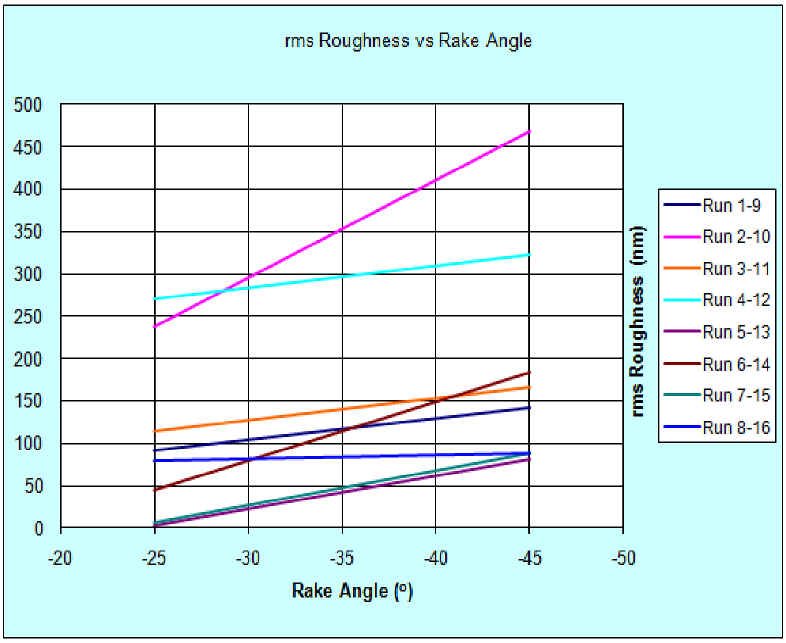

Figure 6.10 Change in Surface Roughness with Rake and Clearance Angle in Experiment 1

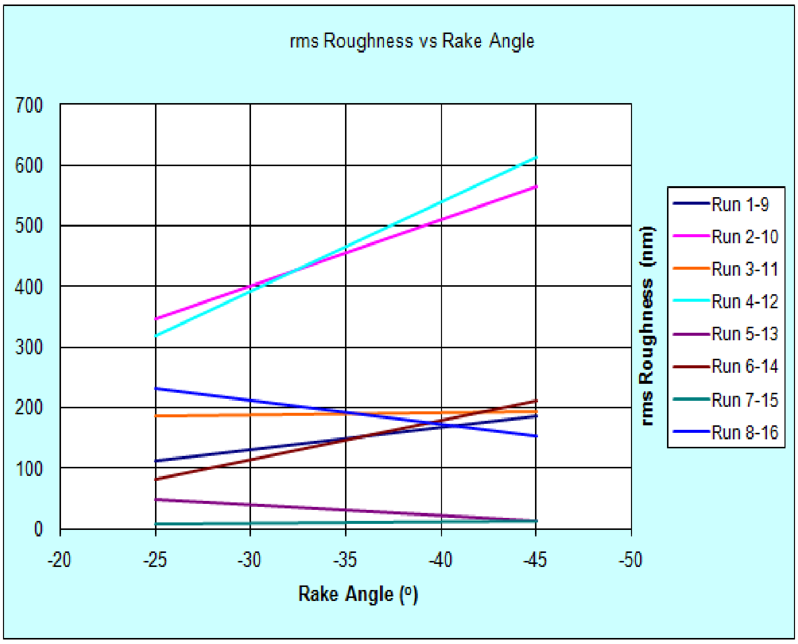

Figure 6.11 Change in Surface Roughness with Rake and Clearance Angle in Experiment 2

6.2.5 Influence of Cutting Speed

Cutting speed was not a parameter for experimental designs of rough cutting of germanium since machining applications were performed at constant spindle speeds. However, in Experiment 3 the measurements have been made at points 5, 10 and 15 mm away from the center of flat disk. At each of these points, cutting speed was different since cutting speed depends on and inversely proportional to spindle speed and diameter of machined point as given in Equation (6.1). Spindle speed was constant during whole machining applications but diameter of machined point was changing and that caused the difference of cutting speed at all machining points.

$$V_c = \pi * d * n \qquad (6.1)$$

Where;
V_c: Cutting Speed (mm/s)
d: diameter (mm)
n: rotational frequency of work-piece (rad/s)

Three graphs were evaluated which were sorted out according to spindle speed at Experiment 3. As shown from Figures 6.12, 6.13, and 6.14, generally curves were horizontal which indicated that cutting speed was not effective on surface roughness at constant spindle speeds in the circumstances selected in experimental studies. The same result was also obtained in previous studies. For instance, in the study of Çalı [18], it was specified that cutting speed was the least important effect for surface roughness. However, the general characteristic was for increasing cutting speed from lower radius point to higher radius point, improved surface finish. This improvement was also specified by Blake [24], it was represented that increased cutting speed improved surface finish on germanium work-pieces. This conclusion have been also gathered from the graphs in Figures 6.12, 6.13, and 6.14.

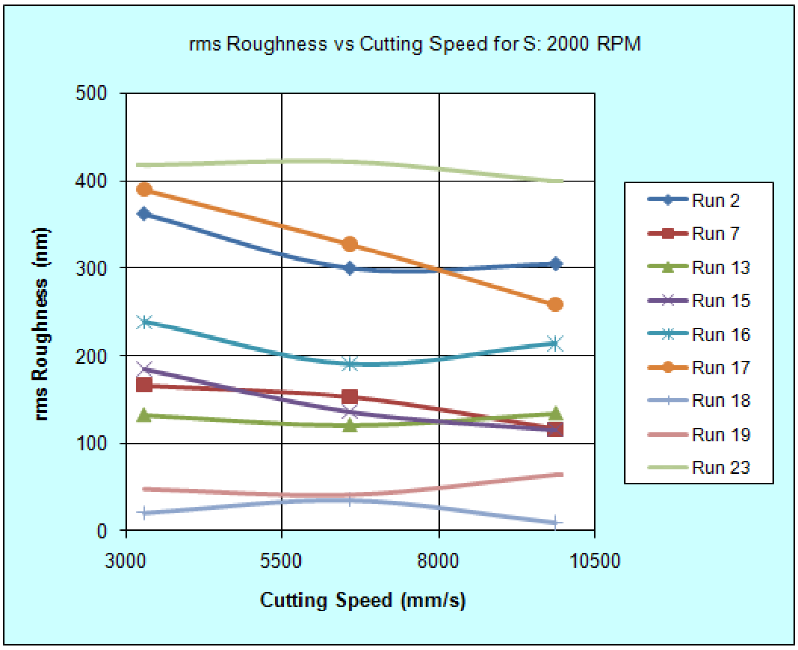

Figure 6.12 Change in Surface Roughness with Cutting Speed at 2000 RPM Spindle Speed

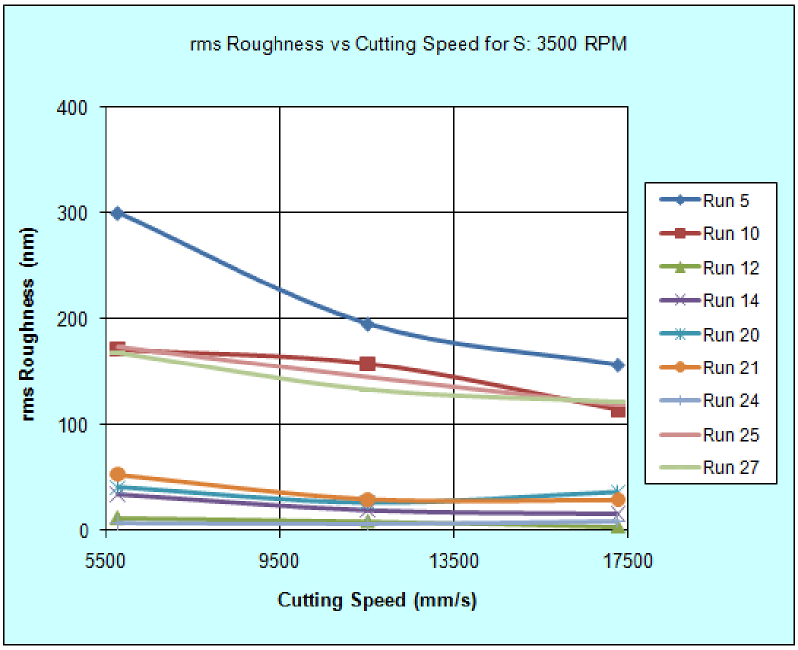

Figure 6.13 Change in Surface Roughness with Cutting Speed at 3500 RPM Spindle Speed

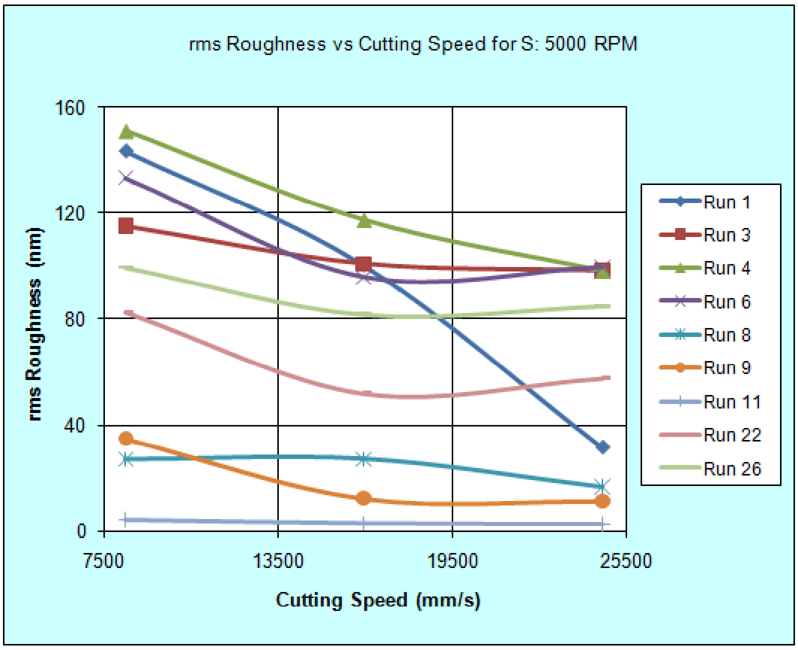

Figure 6.14 Change in Surface Roughness with Cutting Speed at 5000 RPM Spindle Speed

6.3 Other Characteristics of Machined Surfaces

Flat disk and convex lens germanium samples were machined in rough cutting conditions by polycrystalline diamond tools and for this study it was also critical to verify that surfaces, machined by PCD tools, could be machined directly in finish cutting conditions without any process change after rough cutting by PCD tools. Actually, as mentioned before, blanks could be machined in finish cutting conditions and necessary surface finish values could be gathered without any rough cutting application previously. Rough cutting is performed only to give necessary shape to blank, generated by the supplier of germanium.

Therefore, surface finish values as good as blank lenses were enough for rough cutting. The surface finish values of blank lenses were measured and as mentioned in Section 5.2, typical PV, rms and R_a roughness values were measured as 6-7 μm, 800-850 nm and 600-700 nm, respectively. For the conformation of rough cutting with polycrystalline diamond tool, a germanium blank was machined at 20 mm/min feed rate, 200 μm depth of cut and 2000 RPM spindle speed which was one of high rough cutting application and the roughness values of the machined surface, which is shown in Figure 6.15, have been measured as 4328.2 nm PV, 376.5 nm rms and 279.1 nm R_a roughness. After that, this surface has been machined at finish cutting condition with MCD tool and the roughness values of the machined surface, which is shown in Figure 6.16, have been measured as 10.9 nm PV, 1.9 nm rms and 1.5 nm R_a roughness. This result has confirmed that polycrystalline diamond tool was good enough for rough cutting applications since surface finish under 25.4 nm rms could be obtained after finish cutting of germanium surface.

Figure 6.15 Rough Cut Surface with PCD Tool

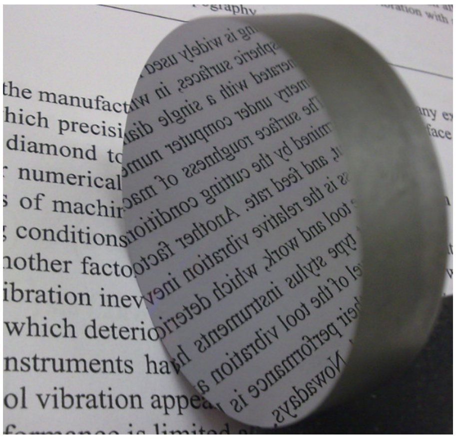

Figure 6.16 Finish Cut Surface with MCD Tool

Furthermore, the interaction of light and germanium surfaces, machined both by mono-crystalline and polycrystalline diamond tools, were observed because germanium surfaces had rainbow appearance at rough cutting conditions machined by PCD tools. This appearance was intense at extreme rough cutting conditions and also seen at machining conditions closer to finish cutting while this was not seen for surfaces machined by MCD tools at the same conditions. As mentioned in Section 2.6, rainbow appearance is formed as a result of light scatter. Therefore, by necessary measurements, this result was evaluated. The necessary measurements were performed by spectrophotometer which is a device consisting of two instruments. Spectrometer part produces light at a selected wavelength range and photometer part measures the intensity of light as transmission or reflection [72].

Actually, a matter responds to incident beam in three main ways. Light may be partly reflected, transmitted or absorbed as shown in Figure 6.17. These three main response appears at the same time but at different proportions. So, the total intensity of beam, which is the magnitude of light, equals to reflection, transmission and absorption intensity expressed in Equation (6.2) [54].

$$I_l = R_l + T_l + A_l \tag{6.2}$$

Where;
I_l: Intensity of light
R_l: Reflection intensity
T_l: Transmission intensity
A_l: Absorption intensity

However, reflections depends on the nature of the surface and reflection can be divided into two as direct (specular) and diffuse (scatter). In direct reflection, light reflected from surface at an angle equal to angle of incidence. While in diffuse reflection or scatter, light reflects equally in all directions and this formed even in shiny surfaces. Actually, reflections from surfaces are the combination of direct and diffuse reflection called mixed reflection [73].

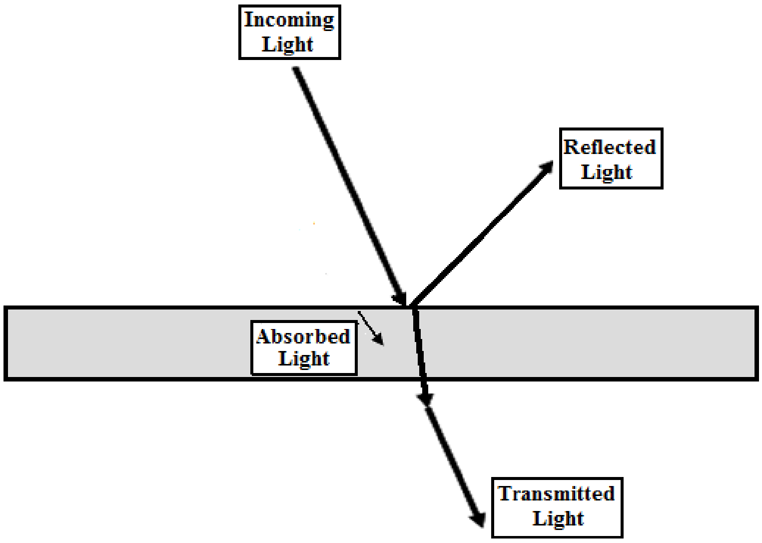

Figure 6.17 Three Main Response of Light on Surface

Therefore, to define the difference between machined surfaces, 5 mm thickness, 25 mm outer diameter, two same disk samples were machined at finish cutting conditions such as 2.5 mm/min feed rate, 4 µm depth of cut and 2000 RPM spindle speed, one by PCD and the other by MCD tool. Both surfaces had rms roughness below 2 nm so, the surface finish conditions were similar. To evaluate surfaces, reflection and transmission of light were measured by spectrophotometer from 1.5 to 13 µm wavelength which corresponds from near infrared to far infrared region.

As shown from Figure 6.18, reflection of light from surfaces were given. However, reflection, measured by spectrophotometer, was direct (specular) reflection so, it didn’t include scatter or diffuse reflection. Blue line indicated proportion of direct reflection of light from surface machined by PCD tool, while black line indicated the proportion of direct reflection of light from surface machined by MCD tool and as shown from graph, surface machined by MCD tool had higher direct reflection. In addition, Figure 6.19 shows the transmission of light from machined surfaces. In this graph, blue line corresponded to surface machined by PCD and red line corresponded to the surface, machined by MCD tool and as shown, surface machined by MCD tool had higher transmission.

Therefore, as a result of evaluation from these two graphs, the proportion of direct reflected and transmitted light was higher for surface machined by mono-crystalline diamond tool. The absorption of light for two surfaces were the same since samples that had same dimensions were used. So, it could be concluded that scattering of light from the surface machined by polycrystalline diamond tool was higher and this was the result of machining germanium with a different tool. This could not be a problem for rough cutting of germanium however, it could be a problem if PCD tools are used for finish cutting.

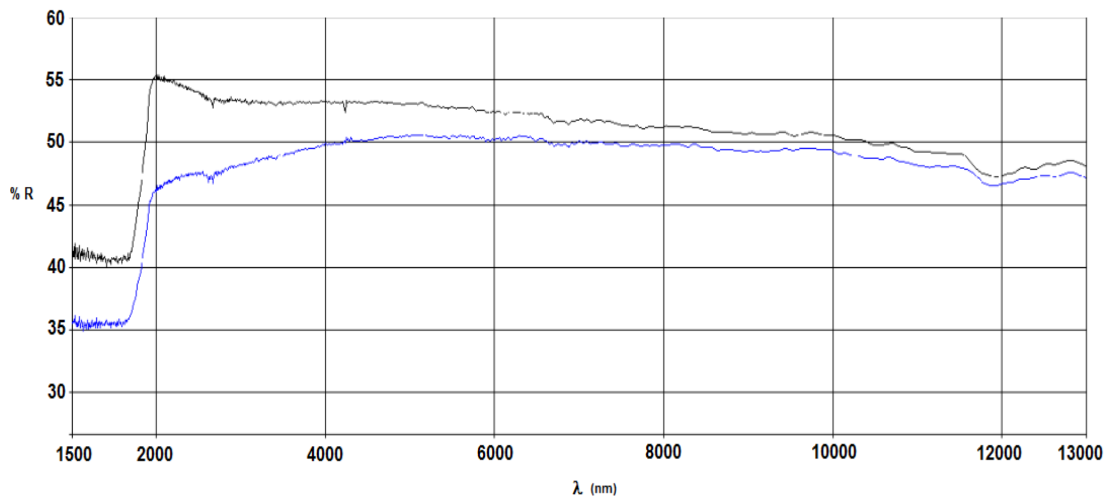

Figure 6.18 Proportion of Direct Reflection of Light

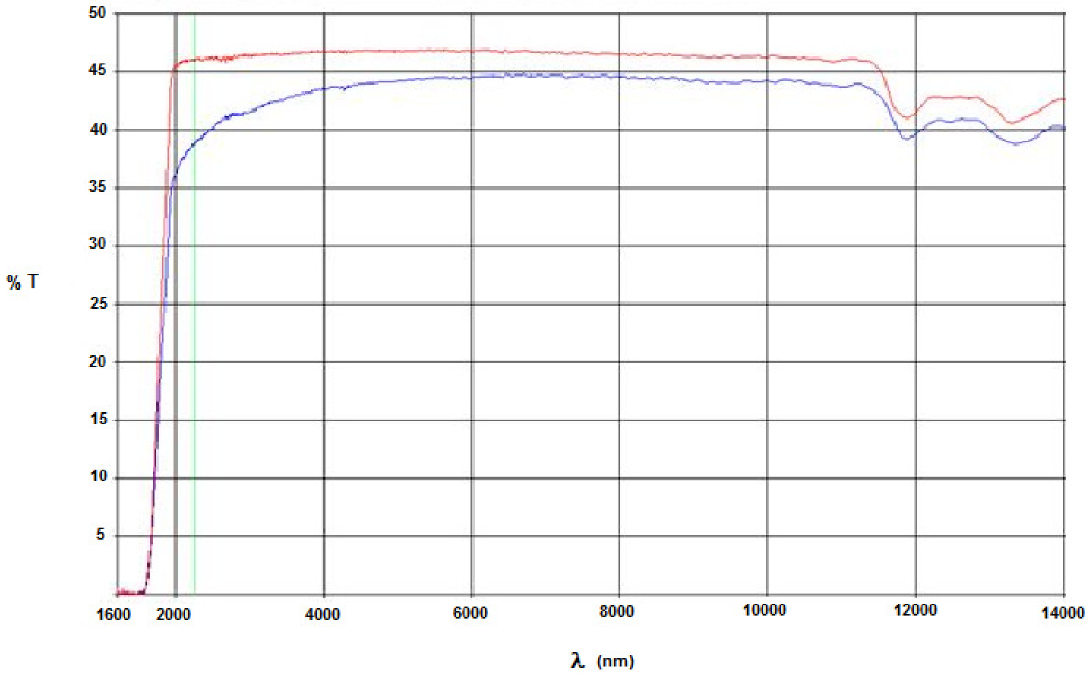

Figure 6.19 Proportion of Transmission of Light

Furthermore, in addition to surface roughness, after machining of convex lens dimensional tolerances of machined surfaces were measured by Taylor Hobson Form Talysurf PGI 1240 Profilometer, shown in Figure 6.20. Dimensional tolerance is generally measured after two finish cutting applications. It is performed to determine the dimensional accuracy and meanwhile, the astigmatism of spherical or aspheric lenses are also measured. Dimensional accuracy is an optical design criteria so it may change form lens to lens. The outer diameter of lens is generally important factor for its dimensional tolerance. For convex lens which has been machined in this thesis study, dimensional tolerance limit can be accepted as maximum 0.316 μm considering its outer diameter according to optical requirements in technical documents of ASELSAN, Inc.

Figure 6.20 Taylor Hobson Form Talysurf PGI 1240

Normally, after rough cutting, dimensional accuracy of lenses was not measured. However since two finish cuttings are performed after rough cutting and depth of cut of finish cutting is generally 4 μm, the dimensional accuracy of machined surface after rough cutting must be less than 8 μm. Therefore, to confirm this, dimensional accuracy of machined surface of convex lens was measured. This lens was machined at high rough cutting conditions as 20 mm/min feed rate, 200 μm depth of cut and 2000 RPM by -25^{o} rake angle PCD tool. As mentioned at Table 5.8, PV, rms and R_a roughness values for that surface was 4150.6 nm, 317.8 nm and 249.9 nm respectively and form of the surface was measured 3.048 μm by the profilometer as shown from Figure 6.21. The high peak part on the right side of graph came up to a spike so it was excluded from the measurement. Therefore, form of the machined surface was convenient for finish cutting since it was less than 8 μm. This result was also confirmed that polycrystalline diamond tools can be used for rough cutting applications.

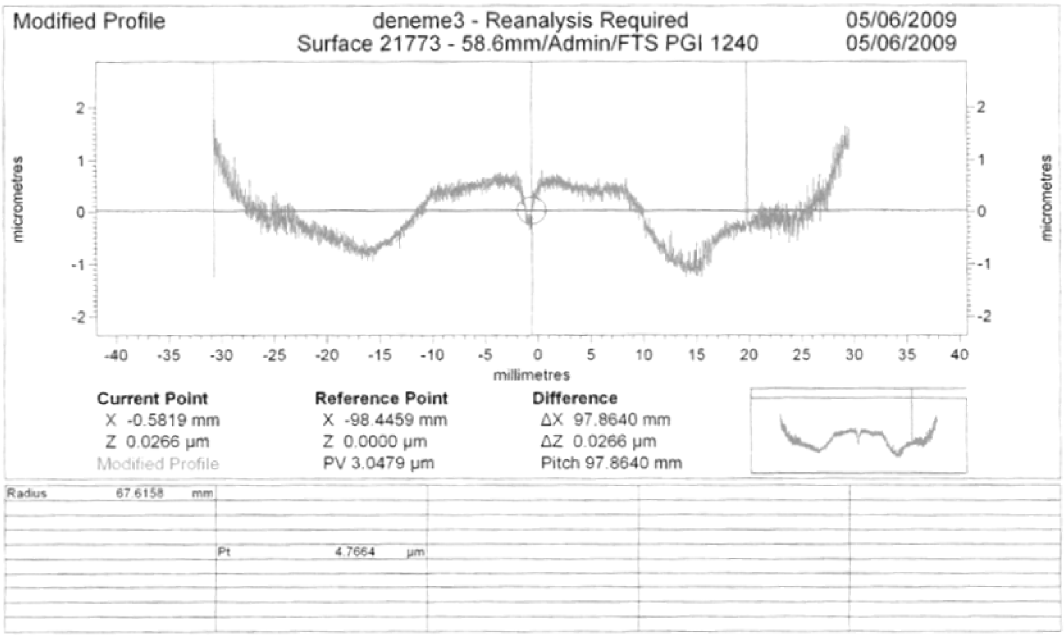

Figure 6.21 Dimensional Accuracy Measurement of Surface After Rough Cutting

Moreover, the form of the surface was also measured after machining at finish cutting conditions by polycrystalline diamond tool. First of all, convex lens was machined at 2.5 mm/min feed rate, 4 µm depth of cut and 5000 RPM spindle speed by -25^o rake angle tool and 1.946 µm dimensional accuracy was measured from surface as shown in Figure 6.22 while PV, rms and R_a roughness were gathered 34.1, 1.3 and 0.9 nm, respectively. Again, the high peak part on right side of graph was excluded since it came up to a spike. Afterwards, convex lens was again machined at 2.5 mm/min feed rate, 4 µm depth of cut and 2000 RPM spindle speed by -25^o rake angle tool and 1.589 µm dimensional accuracy has measured this time as shown in Figure 6.23 while PV, rms and R_a roughness were gathered 50.4, 3.8 and 2.1 nm respectively. Again, the high peak part in the middle of graph was excluded since it came up to a spike. From these two measurements it was realized that polycrystalline diamond tools could not be used for finish cutting applications since dimensional accuracies were highly above 0.316 µm even if rms surface roughness values were below 25.4 nm.

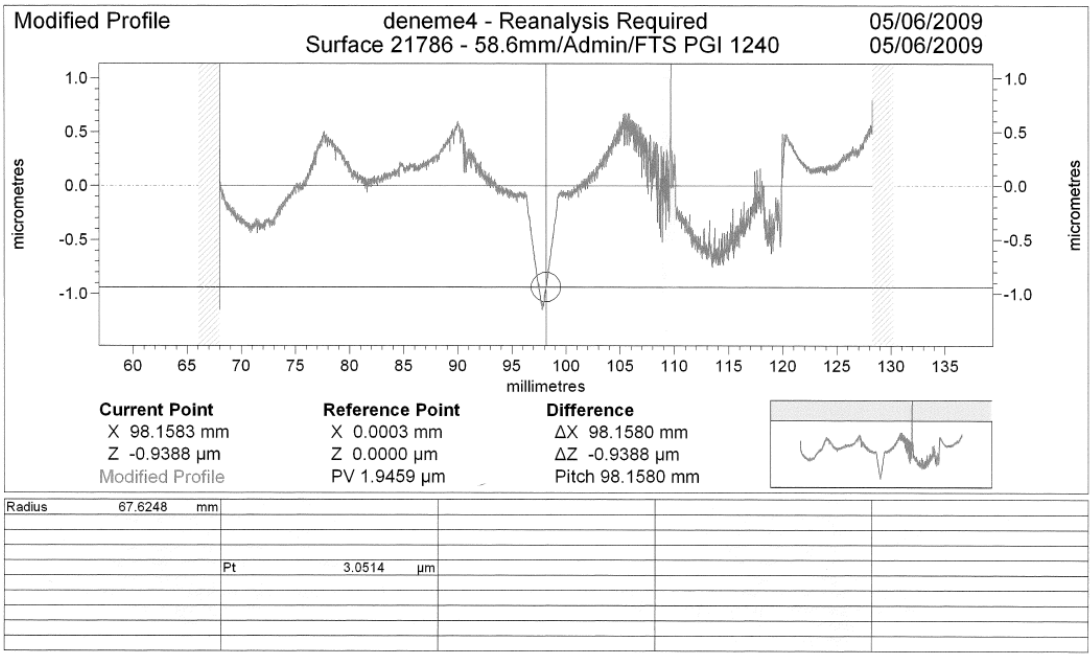

Figure 6.22 Dimensional Accuracy Measurement of Surface After Finish Cutting with 5000 RPM Spindle Speed

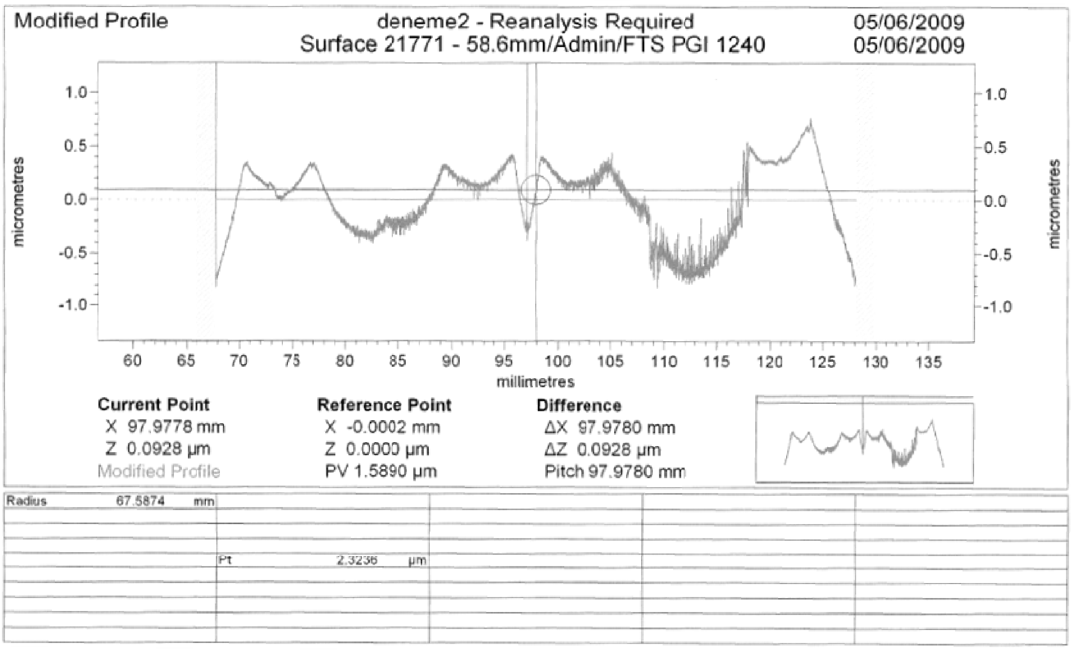

Figure 6.23 Dimensional Accuracy Measurement of Surface After Finish Cutting with 2000 RPM Spindle Speed

6.4 Wear of Polycrystalline Diamond Tool

During experimental studies, tool life of polycrystalline diamond tool has not been investigated however during machining applications, tool wear has been observed. Surface roughness and dimensional tolerance were not affected by tool wear as much extent since rough cutting has been examined during the study so, optical requirements were not as tough as finish cutting. This property of rough cutting has let the usage of polycrystalline diamond tools instead of non-controlled waviness mono-crystalline diamond tools considering their cost advantage and easy supply from market in a more number of sources.

Tool wear of polycrystalline diamond tools were examined with the help of microscopes and video tool set station of Precitech Freeform 700U Diamond Turning Machine. Actually, the purchased polycrystalline diamond inserts, not used any before, have even had much worse waviness when compared with mono-crystalline diamond tools. From Figure 6.24 and 6.25, the waviness difference of mono and polycrystalline diamond tools can be seen. The waviness of non-controlled waviness mono-crystalline diamond tool could not be gathered under 20x magnification while fractures on the edge of polycrystalline diamond insert could be easily identified under same circumstances.

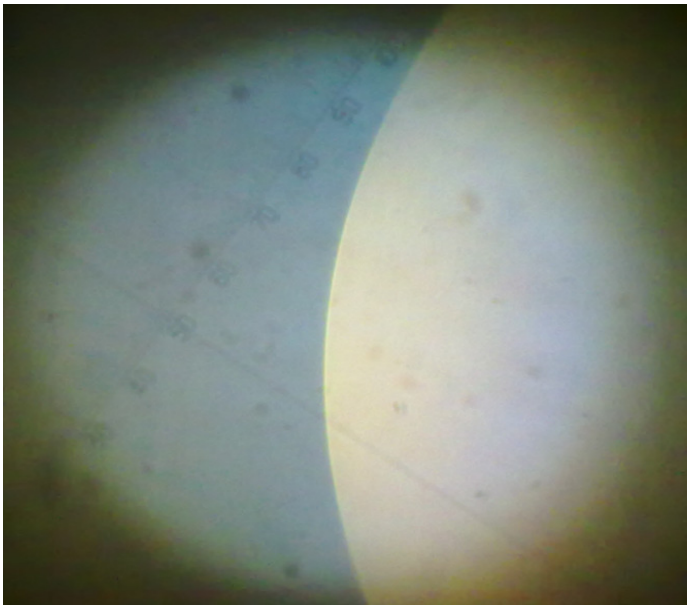

Figure 6.24 MCD Tool under 20x Magnification Microscope

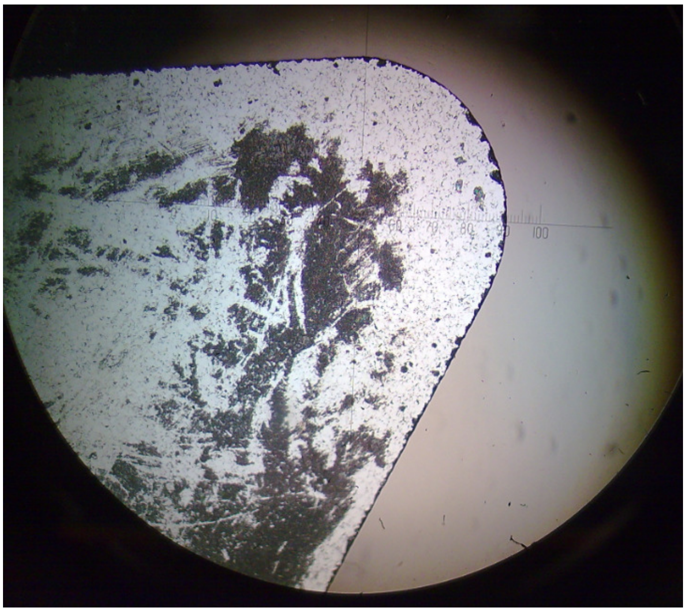

Figure 6.25 PCD Insert under 20x Magnification Microscope Before Machining

After initial trials and 2^4 Full Factorial Design study, for about 35 machining applications have been performed at flat surface of germanium and after that, PCD insert was examined by the 20x microscope again. As shown from Figure 6.26, some diamond particles, sintered under pressure and temperature, have been broken from tip of the insert and also nose radius became flatter. Wear of tool did not affect surface roughness of machined surfaces of germanium at high extent considering rough cutting applications. However, waviness on tip of insert confirms that polycrystalline diamond tools could not be used for finish cutting of lenses because during the machining of lenses always a different point of tool cuts off the surface so, the waviness of tool directly affects the optical quality of surface and this result was actually obtained in Section 6.3 by dimensional accuracy measurements.

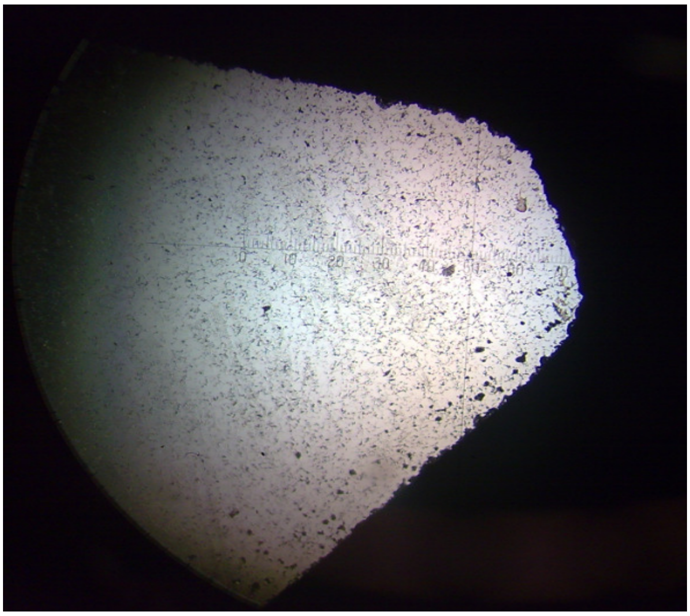

Figure 6.26 20x Magnification Microscope View of Worn PCD Insert

Similar observation was also made after machining of convex lens with a new PCD insert and after initial trials and 2^4 Full Factorial Design study, for about 25 machining applications were performed at convex surface of germanium and after that, insert was examined by the video tool set station, which is the optical microscope of diamond turning machine. As shown from Figure 6.27, similar to insert which has machined flat germanium surface, at the tip of tool breaks were formed. Following cuttings of convex lens by same insert at rough cutting conditions did not change surface roughness dramatically however waviness of tool could not be accepted for finish cutting since as mentioned before, waviness of tool directly affects dimensional accuracy of machined surface.

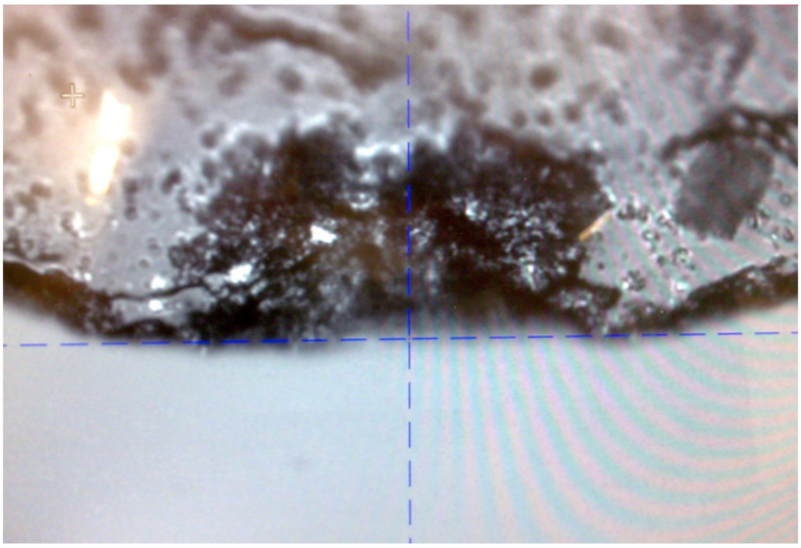

Figure 6.27 Tip of PCD Insert After Machining of Convex Lens

6.5 Recommendations for Future Work

In this thesis study, rough cutting of germanium with polycrystalline diamond tools has been performed. Normally, mono-crystalline diamond tools were used during the machining of germanium in single point diamond turning. So, comparison between these two types of diamond tools were generally mentioned in the thesis. Rough cutting applications have been performed by changing parameters of feed rate, depth of cut, spindle speed and rake angle. However, change of rake angle precipitated change in clearance angle. Therefore, the effect of rake angle could not be obtained directly. Three main experimental studies have been performed in the study and these experiments were realized by 2 and 3 Level Full Factorial and Box-Behnken Design. Hence, mathematical model between surface roughness and selected parameters has been obtained.

During the study, it was found that tool wear was an important problem during the machining of germanium by polycrystalline diamond tools. In addition to high cutting parameters, extreme rake and clearance angles have also triggered tool wear. Therefore, it may be beneficial to study about tool life of polycrystalline diamond tools during the machining of germanium. This can also provide a good economical comparison between mono-crystalline and polycrystalline diamond tools.

In the study, machining studies were performed by -25^{o} and -45^{o} rake angle tools considering previous studies with diamond tools and during experimental studies in this thesis, -25^{o} rake angle tool has resulted better surface finish values. Considering these results, machining can be performed with different rake angle tools to achieve better surface finish results.

As mentioned in the study, surface finish results of machined surfaces were better than the purchased blanks which were generated by the suppliers. Therefore, all surfaces were good enough for rough cutting. However, on some machined germanium surfaces, rainbow effect was seen and as indicated in Section 2.6, vibration of tool may be a result of that. Therefore, tools, which were designed and produced for polycrystalline diamond inserts in this study, may be optimized to suppress vibration and the results of these tools can be compared considering this rainbow effect.

In experimental studies, 2 and 3 Level Full Factorial Design with different number of parameters and Box-Behnken Design with three parameters were performed and mathematical models were obtained between surface roughness and parameters. In another study, different experimental designs can be used for comparison to attain better mathematical models.

In this study, rough cutting of germanium by polycrystalline diamond tools were investigated. However, in different studies, different materials may be searched such as silicon, zinc sulfide and zinc selenide which are also widely used in thermal imaging systems.

Furthermore, polycrystalline diamond inserts used in experiments and the worst case studies were supplied from same manufacturer and these inserts have same coatings. Therefore, it may be beneficial to study polycrystalline diamond inserts with different coatings from same and different producers. Also, different cutting tools such as synthetic diamond, chemical vaporized deposition diamond (CVD-diamond) or cubic boron nitride (CBN), some of which were compared by PCD tool for the machining of different materials as mentioned in Section 2.5, can be experimented for the machining of infrared materials. Moreover, finish cutting performance of polycrystalline diamond tools can be investigated in a detailed way for machining of infrared materials.

REFERENCES

[1] Xiangyang, J., Nebel, J., Siebert, J.P., “3D Thermography Imaging Standardization Technique for Inflammation Diagnosis”, Proceedings of SPIE, Vol. 5640, pp. 266-273, 2005.

[2] Picture My Health, www.picturemyhealth.com, last visited on 2 March 2010.

[3] Msnbc, http://www.msnbc.msn.com/id/30523865, last visited on 15 February 2010.

[4] Inspection Masters, www.inspectmasters.com, last visited on 15 February 2010.

[5] ASELSAN, Inc., www.aselsan.com.tr, last visited on 2 March 2010.

[6] Boothroyd, G., Knight, W.A., “Fundamentals of Machining and Machine Tools”, Third Edition, Taylor & Francis Group, 2006.

[7] Lecture Notes on Mechanics of Metal Cutting, www.me.metu.edu.tr/courses/me535, last visited on 25 February 2010.

[8] Engineers Edge, LLC, www.engineersedge.com, last visited on 21 March 2010.

[9] State Master, www.statemaster.com, last visited on 21 March 2010.

[10] Boeing Consult, www.boeingconsult.com, last visited on 15 February 2010.

[11] Venkatesh, V.C. and Izman, S., “Precision Engineering”, New Delhi, Tata McGraw-Hill Publishing Company Limited, 2007.

[12] Lecture Notes on Cutting Fluids and Surface Roughness, www.me.metu.edu.tr/courses/me535, last visited on 2 March 2010.

[13] Cheung, C.F. and Lee, W.B., “Surface Generation in Ultra-precision Diamond Turning: Modelling and Practices”, Wiltshire, Professional Engineering Publishing, 2003.

[14] Morris, J.C., “Microstructural Analysis of Plasticity in Low-Load Contact Damage of Silicon and Germanium”, Rice University, Houston, Texas 1995.

[15] Smith, K., Winger, R., Lettington, A.H., Stillwell, P.F.T.C., “Diamond Turning of Mirrors and Infrared Optical Components”, Journal of Physics D: Applied Physics, 21, pp. 67-70, 1988.

[16] Blake, P.N. and Scattergood, R.O., “Ductile Regime Machining of Germanium and Silicon”, Journal of the American Ceramic Society, Vol. 73, No. 4, pp.949-957, 1989.

[17] Yu, J. and J. Yan, “Ultra-precision Diamond Turning of Optical Crystals”, SPIE, p. 51-59, 1994.

[18] Çalı, S, “An Experimental Study on Single Crystal Diamond Turning of Optical Quality Silicon”, Middle East Technical University, Ankara, 2008.

[19] Chao, C.L., Ma, K.J., Liu, D.S., Bai, C.Y., Shy, T.L., “Ductile Behaviour of Single Point Diamond Turning of Single-crystal Silicon”, Journals of Materials Processing Technology, 127, pp. 187-190, 2002.

[20] Jasinevicius, R.G., Porto, A.J.V., Pizani, P.S., Duduch, J.G., Santos, F.J., “Characterization of Structural Alteration in Diamond Turned Silicon Crystal by Means of Micro Raman Spectroscopy and Transmission Electron Microscopy”, Vol. 8, No.3, 2005.

[21] Yan, J., Syoji, K., Tamaki, J., “Some Observations on the Wear of Diamond Tools in Ultra-precision Cutting of Single-crystal Silicon”, Wear, 255, pp. 1380-1387, 2003.

[22] Mai, Y.W., Atkins, A.G., “Elastic and Plastic Fracture”, Ellis Horwood/John Wiley, 1985.

[23] O’Connor, B.P., “The Effect of Crystallographic Orientation on Ductile Material Removal in Silicon”, The Pennsylvania State University, 2002.

[24] Blake, P.N., “Ductile-regime Diamond Turning of Germanium and Silicon”, North Carolina State University, Charlotte, 1988.

[25] Patten, J.A., “High Pressure Phase Transformation Analysis and Molecular Dynamics Simulations of Single Point Diamond Turning of Germanium”, North Carolina State University, Charlotte, 1996.

[26] Ohta, T., Yan, J., Yajima, S., Takahashi, Y., Horikawa, N., Kuriyagawa, T., “High-efficiency Machining of Single-crystal Germanium Using Large-radius Diamond Tools”, International Journal of Surface Science and Engineering, Vol. 1, No. 4, 2007.

[27] Patten, J., Cherukuri, H., “Ductile Machining Phenomena of Nominally Brittle Materials at the Nanoscale”, Selected Papers from IPMM-2003 The Fourth International Conference on Intelligent Processing and Manufacturing of Materials, pp. 459-469, 2004.

[28] Yan, J., Syoji, K., Kuriyagawa, T., Suzuki, H., “Ductile Regime Turning at Large Tool Feed”, Journal of Materials Processing Technology, 121, pp. 363-372, 2002.

[29] Hochheimer, H.D., Kuchta, B., Dorhout, P.K., Yarger, J.L., “Frontiers of High Pressure Research II: Application of High Pressure to Low Dimensional Novel Electronic Materials”, Nato Science Series, pp. 291-302, 2001.

[30] Shimomura, O., Minomura, S., Sakai, N., Asaumi, K., Tamura, K., Fukushima, J., Endo, H., “Pressure-induced Semiconductor-metal Transitions in Amorphous Silicon and Germanium”, Philosophical Magazine, Vol. 29, pp. 547-588, 1974.

[31] Morris, J.C., Callahan, D.L., Kulik, J., Patten, J.N., Scattergood, R.O., “Origins of the Ductile Regime in Single Point Diamond Turning of Semiconductors”, Journal of the American Ceramic Society, Vol. 78, No. 8, pp. 2015-2020, 1995.

[32] Jasinevicius, R.G., Porto, A.J.V., Duduch, J.G., Pizani, P.S., Lanciotti Jr., F., dos Santos, F.J., “Multiple Phase Silicon in Sub-micrometer Chips Removed by Diamond Turning”, Journal of the Brazilian Society of Mechanical Sciences and Engineering, Vol. 27, No. 4, pp. 440-448, 2009.

[33] Jasinevicius, R.G., “Influence of Cutting Conditions Scaling in the Machining of Semiconductors Crystals with Single Point Diamond Tool”, Journal of Materials Processing Technology, Vol. 179, pp. 111-116, 2006.

[34] Zhong, Z., Hung, N.P., “Diamond Turning and Grinding of Aluminum-Based Metal Matrix Composites”, Materials and Manufacturing Processes, Vol. 15, No. 6, pp. 853-865, 2000.

[35] D’Errico, G.E., Calzavarini, R., “Turning of Metal Matrix Composites”, Journal of Materials Processing Technology, Vol. 119, pp. 257-260, 2001.

[36] Sreejith, P.S., “Machining Force Studies on Ductile Machining of Silicon Nitride”, Journal of Materials Processing Technology, Vol. 169, pp. 414-417, 2005.

[37] Davim, J.P., Mata, F., “New Machinability Study of Glass Fibre Reinforced Plastics Using Polycrystalline Diamond and Cemented Carbide (K15) Tools”, Materials and Design, Vol. 28, pp. 1050-1054, 2007.

[38] Petropoulos, G., Mata, F., Davim, J.P., “Statistical Study of Surface Roughness in Turning of Peek Composites”, Materials and Design, Vol. 29, pp. 218-223, 2008.

[39] Morgan, C.J., Vallance, R.R., Marsh, E.R., “Micro Machining Glass with Polycrystalline Diamond Tools Shaped by Micro Electro Discharge Machining”, Journal of Micromechanics and Microengineering, Vol. 14, pp. 1687-1692, 2004.

[40] Sreejith, P.S., Krishnamurthy, R., Malhotra, S.K., Narayanasamy, K., “Evaluation of PCD Tool Performance During Machining of Carbon/Phenolic Ablative Composite”, Journal of Materials Processing Technology, Vol. 104, pp. 53-58, 2000.

[41] Nabhani, F., “Wear Mechanism of Ultra-hard Cutting Tools Materials”, Journal of Materials Processing Technology, Vol. 115, pp. 402-412, 2001.

[42] Cheng, X., Wang, Z.G., Nakamoto, K., Yamazaki, K., “Design and Development of a Micro Polycrystalline Diamond Ball End Mill for Micro/nano Freeform Machining of Hard and Brittle Materials”, Journal of Micromechanics

and Microengineering, Vol. 19, pp. 1-10, 2009.

[43] Belmonte, M., Ferro, P., Fernandes, A.J.S., Costa, F.M., Sacramento, J., Silva, R.F., "Wear Resistant CVD Diamond Tools For Turning of Sintered Hardmetals", Diamond and Related Materials, Vol. 12, 738-743, 2003.

[44] Contour Fine Tooling, www.contour-diamonds.com, last visited on 29 April 2008.

[45] Global Contact, www.gclabsite.com, last visited on 21 February 2010.

[46] Sohn, A., Lamonds, L., Garrard, K., "Modeling of Vibration in Single-point Diamond Turning", Proceedings of the Twenty-first Annual Meeting of the ASPE, 39, 2006.

[47] Riedl, M.J. and Izman, "Optical Design Fundamentals for Infrared Systems", Second Edition, SPIE Press, 2001.

[48] Schaefer, J., Scott, S., "Single Point Diamond Turning of Optical Components", Texas Instruments Incorporated, Custom Optics Services, 1991.

[49] 4M Micro-Optical Consortium, www.opticsmanufacturing.net, last visited on 21 March 2010.

[50] Precitech Inc., www.precitech.com, last visited on 4 March 2010.

[51] Yan, J., Maekawa, K., Tamaki, J., Kubo, A., "Experimental Study on the Ultraprecision Ductile Machinability of Single-Crystal Germanium", Japan Society Mechanical Engineering, Series C, Vol. 47, No. 1, 2004.

[52] Asians Metal Inc., www.asianmetal.com, last visited on 7 March 2010.

[53] Matweb, Material Property Data, www.matweb.com, last visited on 22 February 2010.

[54] Askeland, D.R., Phulé, P.P., "The Science and Engineering of Materials", Toronto, Fifth Edition, Thomson Learning, 2006.

[55] Karow, K.H., "Fabrication Methods for Precision Optics", John Wiley & Sons, Inc., 1993.

[56] Michigan Technological University Mechanical Engineering, www.me.mtu.edu, last visited on 23 February 2010.

[57] Technodiamant USA Inc., www.technodiamant.com, last visited on 5 March 2010.

[58] National Institute of Standards and Technology, http://www.itl.nist.gov, last visited on 23 February 2010.

[59] Krulewich, D.A., "Experimental Design for Single Point Diamond Turning of Silicon Optics", UCRL-ID-127385, 1996.

[60] Tooling University, LLC, www.toolingu.com, last visited on 7 March 2010.

[61] Electronics Cooling, www.electronics-cooling.com, last visited on 23 February 2010.

[62] Griffiths, B.J., "Manufacturing Surface Technology Surface Integrity & Functional Performance", New York, Taylor & Francis Books, Inc., 2001.

[63] Anderson Materials Evaluation, www.andersonmaterials.com, last visited on 4 January 2010.

[64] Laser Focus World, www.laserfocusworld.com, last visited on 23 February 2010.

[65] Zygo Corporation, www.zygo.com, last visited on 19 July 2009.

[66] Mitsubishi Material, http://www.mitsubishicarbide.net, last visited on 5 January 2010.

[67] Smith, G.T., "Industrial Metrology Surfaces and Roundness", Southampton, Springer-Verlag London Limited, 2002.

[68] Goupy, J., Creighton, L., "Introduction to Design of Experiments with JMP® Examples", Cary, Third Edition, SAS Institute Inc., 2007.

[69] Department of Physics and Astronomy, Georgia State University, http://hyperphysics.phy-astr.gsu.edu, last visited on 19 May 2010.

[70] Patten, J., Gao, W., Yasuto, K., “Ductile Regime Nanomachining of Single-Crystal Silicon Carbide”, Journal of Manufacturing Science and Engineering, Vol. 127, pp. 522-532, 2005.

[71] Fang, F.Z., Venkatesh, V.C., “Diamond Cutting of Silicon with Nanometric Finish”, Annals of the CIRP, Vol. 47, pp. 45-49, 1998.

[72] Rice University Experimental Biosciences Introductory Laboratory Bios 211, www.ruf.rice.edu, last visited on 3 April 2010.

[73] Jacobson, R.E., Ray, S.F., Attridge, G.G., Axford, N.R., “The Manual of Photography, Photographic and Digital Imaging”, Burlington, Ninth Edition, Focal Press, 2000.

[74] Dorrenberg Edelstahl GmbH, http://www.doerrenberg.de, last visited on 11 June 2010.

APPENDIX A

TECHNICAL SPECIFICATIONS OF SINGLE POINT DIAMOND TURNING MACHINE

Table A.1 Technical Specifications of Precitech Freeform 700U [50]

Machine Property	Description
Base	Sealed natural granite base
Type	Ultra-precision, two, three or four axes CNC contouring machine
Programming Resolution	0.01 nm linear, 0.0000001^{o} rotary
Slideways Position Feedback Resolution	0.032 nm
Slideways X-axis Straightness	Horizontal: 0.30 µm full travel
Slideways Z-axis Straightness	Horizontal: 0.40 µm full travel
Slideways Vertical Straightness	X: 0.75 µm, Z: 0.75 µm
Vibration Isolation	Self leveling dual chamber pneumatic isolation system
Drive System	AC linear motor
Swing Capacity	700 mm
Slide Travel	X- 350 mm, Z- 300 mm
Maximum Feed Rate	4000 mm/min
Workholding Spindle Air Bearing Type	Slot-type thrust bearing
Workholding Spindle Motor	Integral brushness motor
Workholding Spindle Load Capacity	68 kg
Workholding Spindle Maximum Speed	7000 RPM
Workholding Spindle Axial Stiffness	228 N/µm
Workholding Spindle Radial Stiffness	88 N/µm
Workholding Spindle Motion Accuracy	Axial/Radial ≤ 25 nm
Thermal Control	Liquid cooled chiller ± 0.1 ^{o}C accuracy
C-axis Feedback Resolution	0.026 arc-sec
C-axis Position Accuracy	± 2 arc-sec
C-axis Maximum Speed	3000 RPM
B-axis Tabletop Size	380 mm
B-axis Load Capacity	454 kg

Machine Property	Description
B-axis Maximum Speed	10 RPM
B-axis Position Feedback Resolution	0.003 arc-sec
B-axis Radial Stiffness	525 N/μm
B-axis Axial Stiffness	875 N/μm

APPENDIX B

TECHICAL SPECIFICATIONS OF WHITE LIGHT INTERFEROMETRY

Table B.1 Technical Specifications of Zygo NewView 5000 Interferometry [65]

Property	Description
Measurement Technique	Non-contact, 3-D, scanning white-light and optical phase-shifting interferometry
Objectives	Infinite conjugate interferometric objectives; 1X, 2X, 2.5X, 5X, 10X, 20X, 50X, 100X
Measurement Array	Standard, selectable, include: 640x480, 320x240, 160x120
Vertical Resolution	Up to 0.1 nm
Lateral Resolution	0.45 to 11.8 µm, objective dependent
Working Distance	0.55 to 20.5 mm, objective dependent
Focus Depth	± 0.5 to 322.5 µm, objective dependent
Field of View (H x V)	0.070 x 0.053 to 7.00 x 5.30 mm, objective dependent
Maximum Slope	1.41^{o} to 33.25^{o}, objective dependent
Maximum Data Points	307,200; dependent upon sampling array
Test Part Material	Various, opaque and transparent surface; coated and uncoated; specular and nonspecular
Test Part Reflectivity	1-100 %

APPENDIX C

TECHNICAL DRAWINGS OF TOOLS

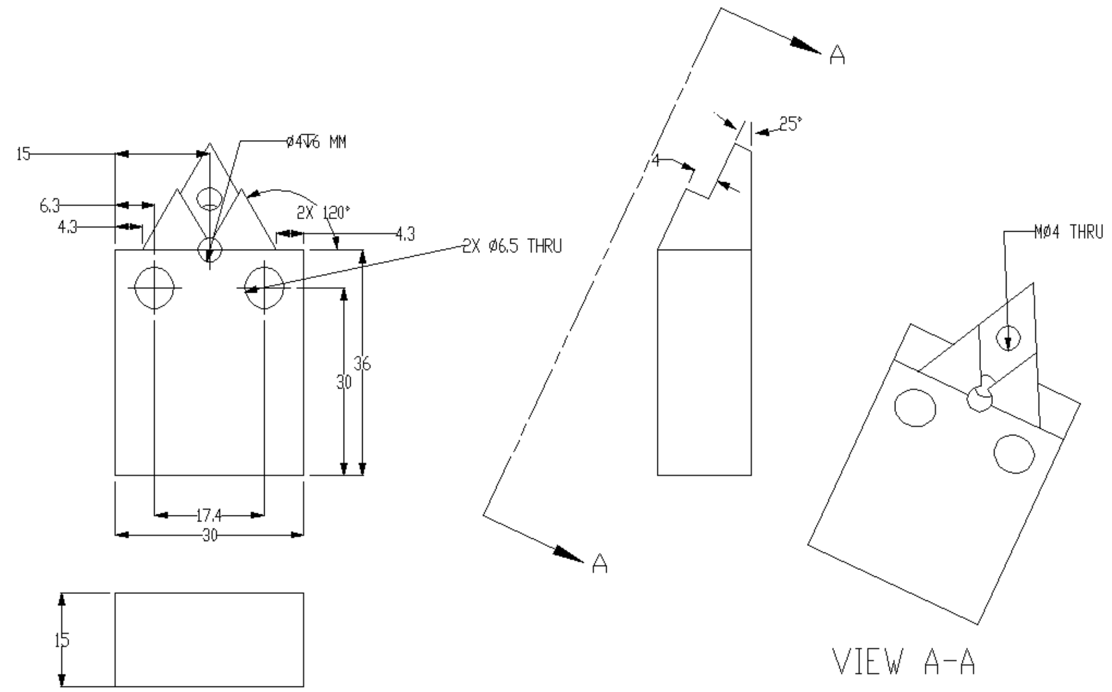

Figure C.1 Technical Drawing of Polycrystalline Diamond Tool with -25^{o} Rake Angle

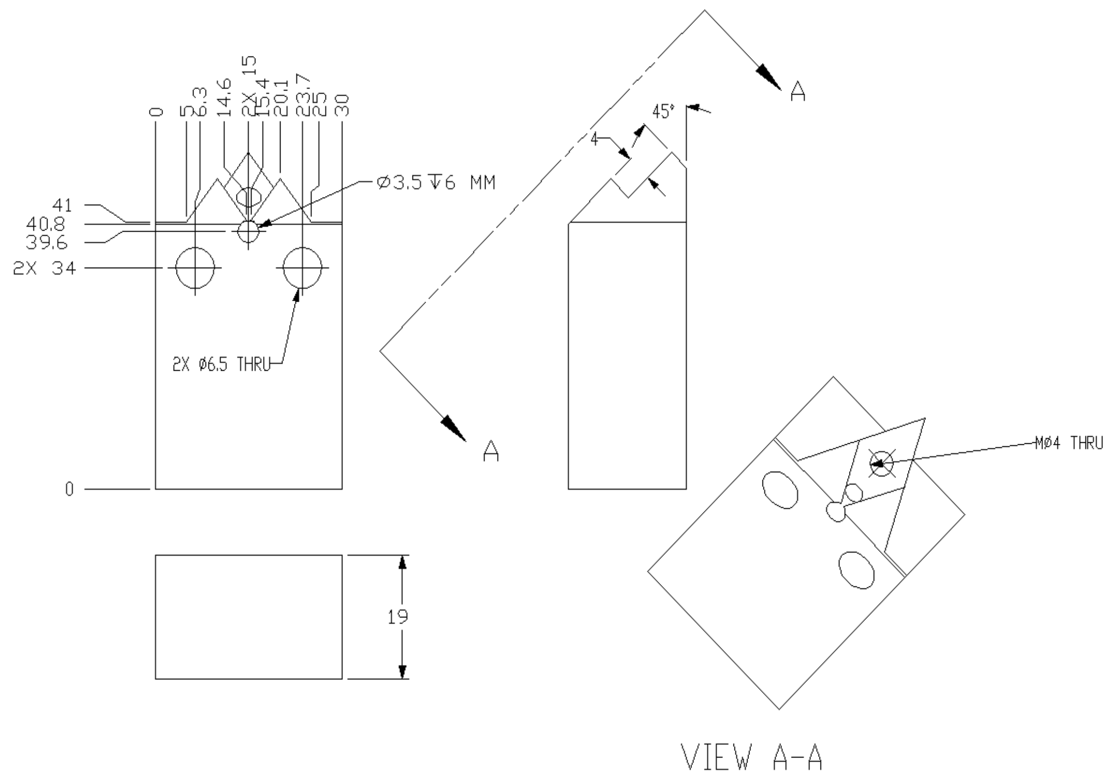

Figure C.2 Technical Drawing of Polycrystalline Diamond Tool with -45^{o} Rake Angle

APPENDIX D

TECHNICAL INFORMATION OF TOOL MATERIAL

Table D.1 Technical Information of CPPU Cold Work Tool Steel [74]

Property	Description
Material Number	1.2379
Code	X153CrMoV12
Chemical Composition (%)	C: 1.55, Cr: 12.00, Mo: 0.80, V: 0.90
Steel Properties	Ledeburitic 12 % chrome steel, very high resistance against abrasive and adhesive wear due to high volume of hard carbides in the steel matrix
Applications	Cutting, punching, stamping tools, shear blades, thread rolling dies, cold extrusion dies, drawing and bending tools, fine cutting tools, deep drawing tools, plastic mould for abrasive polymers, flanging and straightening tools
Conditions of Delivery	Soft annealed to maximum 255 HB

APPENDIX E

SURFACE ROUGHNESS MEASUREMENTS

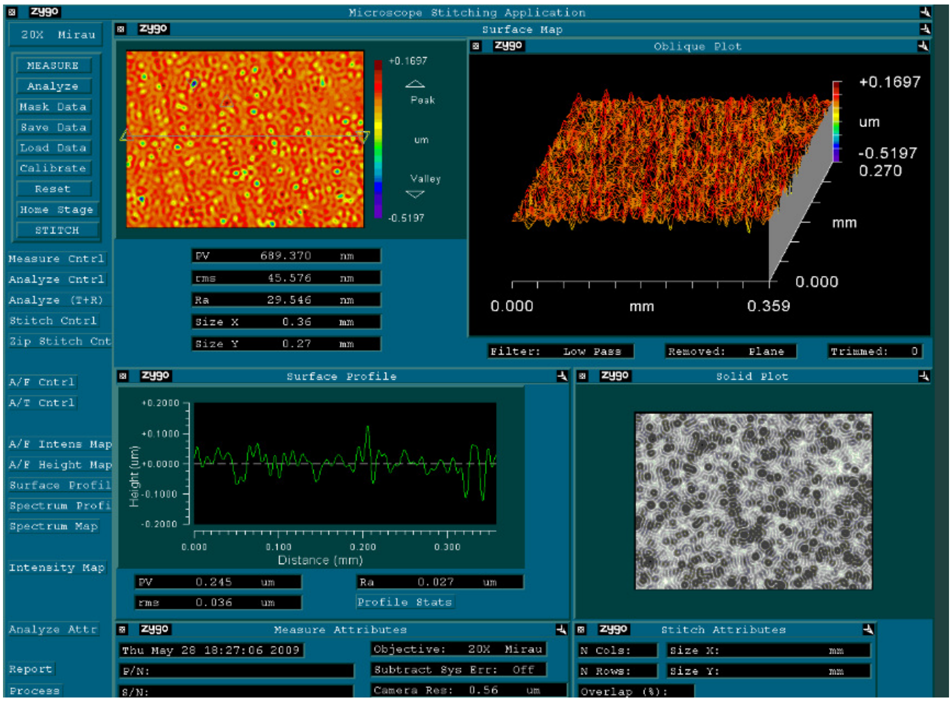

Figure E.1 Run 6 of 2^4 Full Factorial Design of Flat Surface

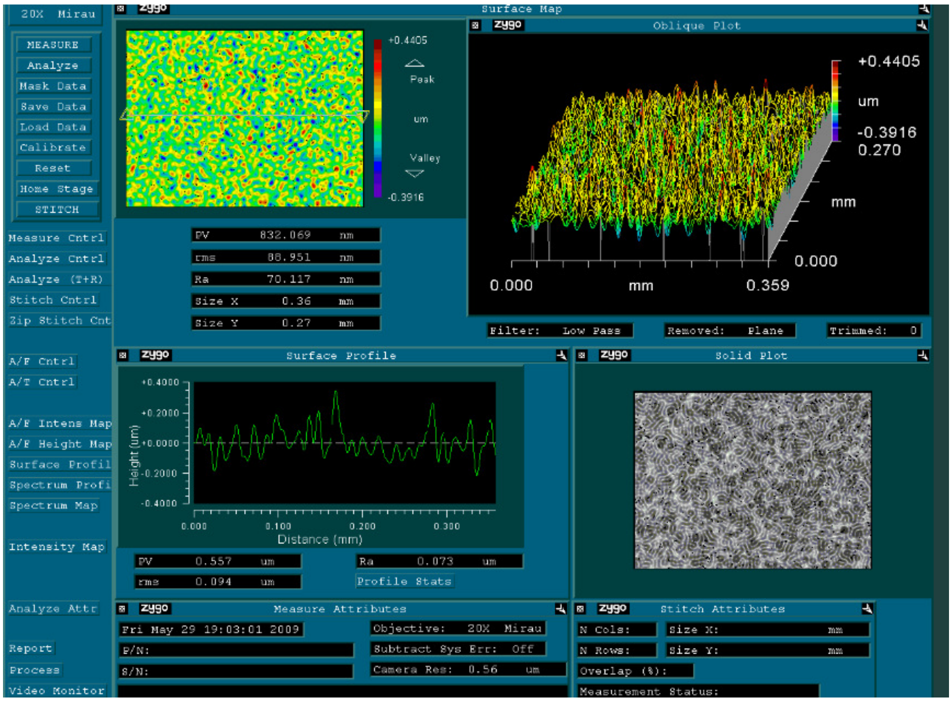

Figure E.2 Run 16 of 2^4 Full Factorial Design of Flat Surface

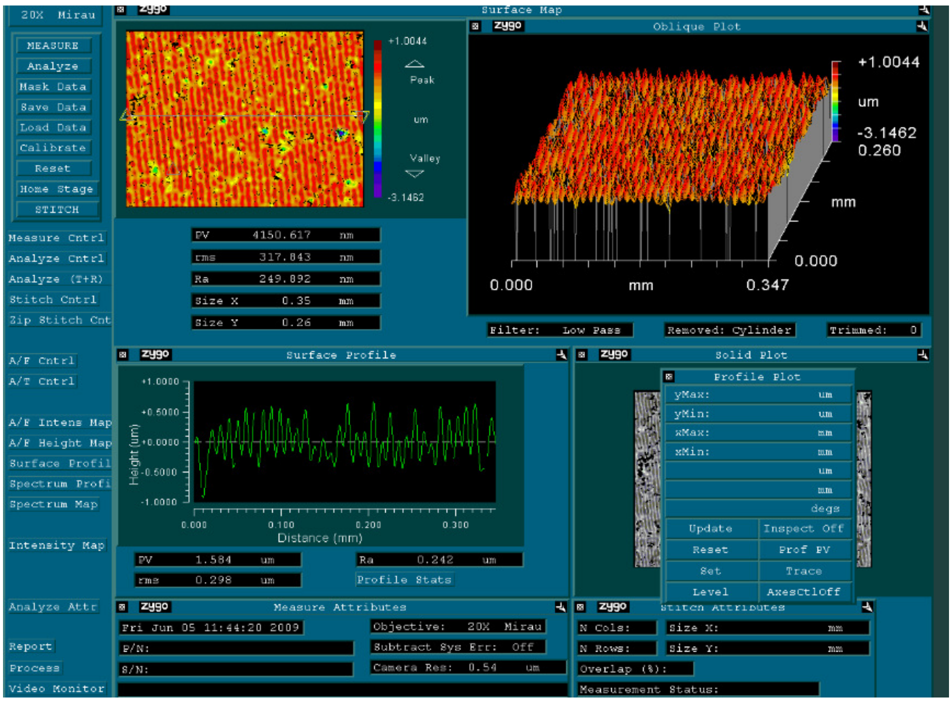

Figure E.3 Run 4 of 2^4 Full Factorial Design of Convex Surface

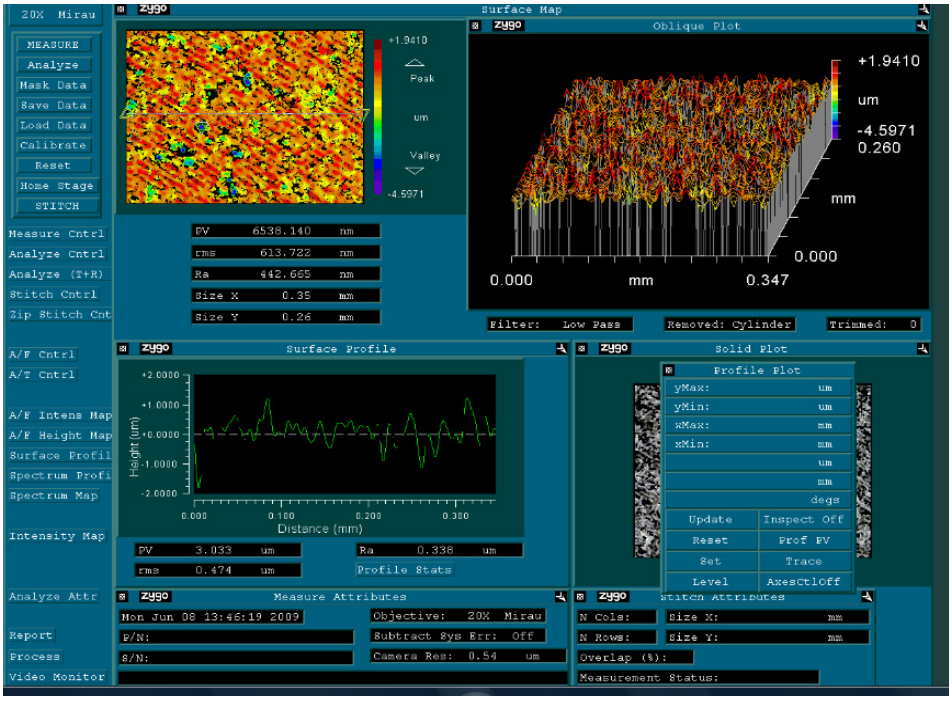

Figure E.4 Run 12 of 2^4 Full Factorial Design of Convex Surface

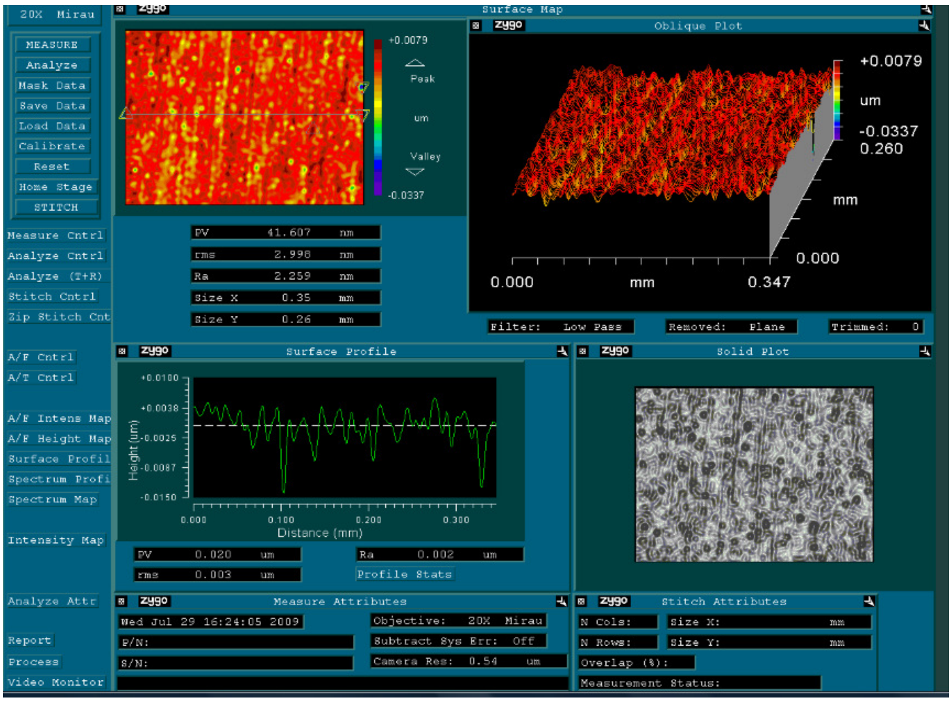

Figure E.5 Run 11 of 3^3 Full Factorial Design of Flat Surface

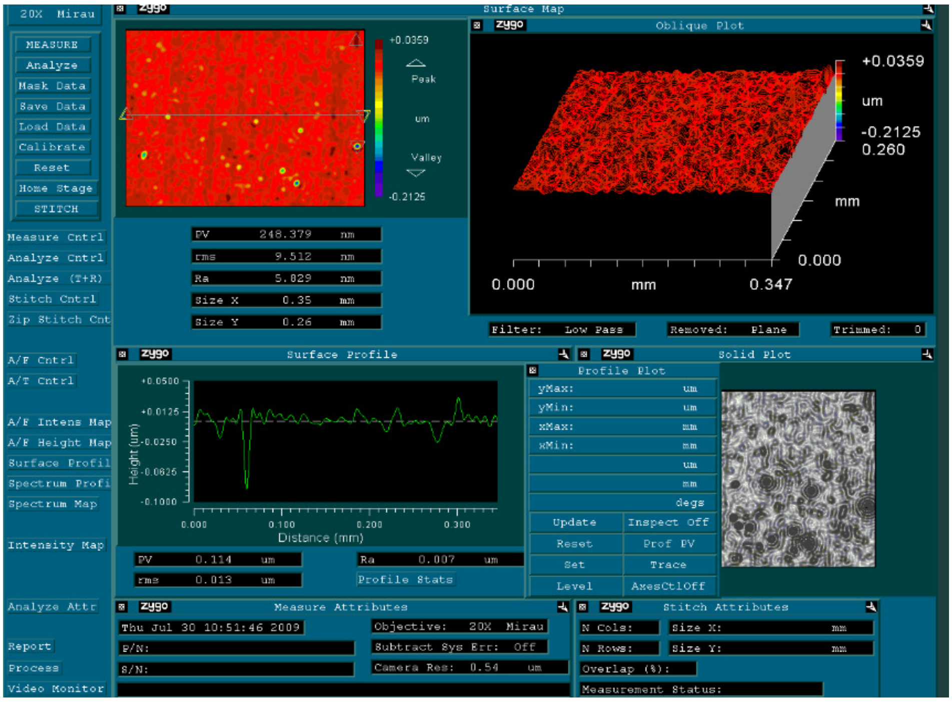

Figure E.6 Run 18 of 3^3 Full Factorial Design of Flat Surface

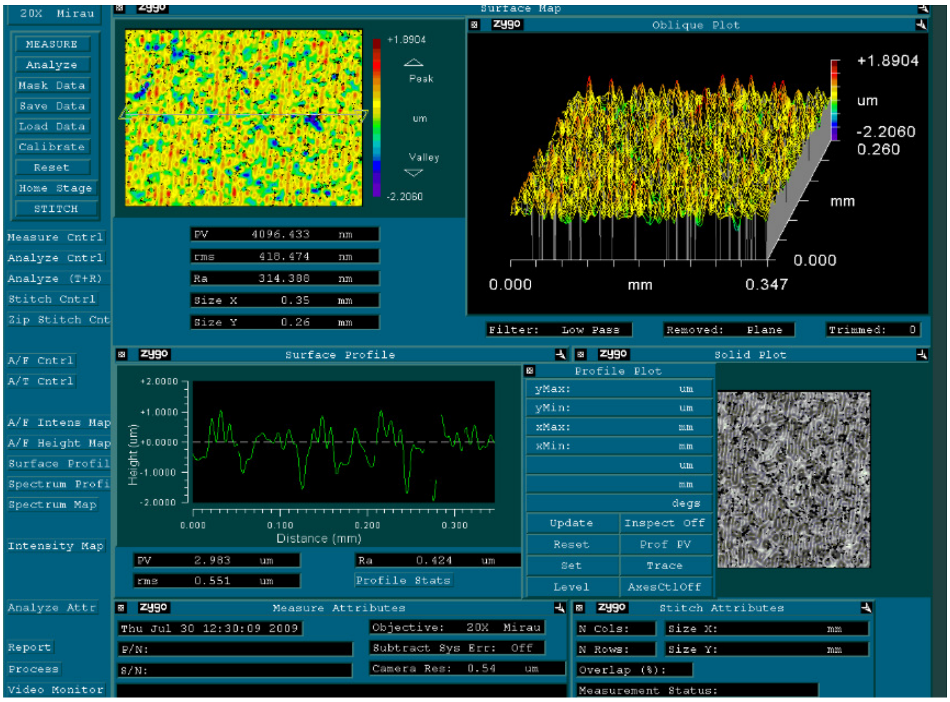

Figure E.7 Run 23 of 3^3 Full Factorial Design of Flat Surface

APPENDIX F

2^2 FULL FACTORIAL DESIGN

Information Extracted from Introduction to Design of Experiments with JMP Examples [67]

F.1 Interpreting the Coefficients

For a 2^2 full factorial design, the postulated model is

$$y = a_0 + a_1 * x_1 + a_2 * x_2 + a_{12} * x_1 * x_2 \tag{F.1}$$

Where

- y is the response.
- x_1 represents the level of factor 1.
- x_2 represents the level of factor 2.
- $x_1 * x_2$ is the product of the levels of factors (i.e. factor 1 × factor 2). Using coded units, this product is equal to –1 ($x1*x2 = -1\times +1 = +1\times -1 = -1$) or +1 ($x1*x2 = -1\times -1 = +1\times +1 = +1$).
- a_0 is the intercept of the model (also called the constant term).
- a_1 is the coefficient of factor 1.
- a_2 is the coefficient of factor 2.

- a_{12} is the coefficient of the x_1*x_2 (the interaction) term.

This model is called the first-degree model with interaction, and we now examine the meaning of each coefficient.

F.2 Interpreting the Intercept

To find the meaning of the intercept, a_0, simply assign the value 0 (in coded units) as the level of both factors. This representative experimental point then corresponds to the center of the study domain in Figure F.1 and the response at this point has a value, denoted y_0.

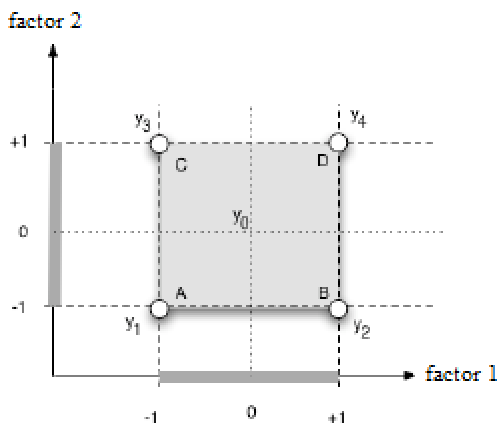

Figure F.1 Response Value

The response value at the intercept is at the center of the domain

Equation (F.1) becomes

$$y_0 = a_0 + a_1 * 0 + a_2 * 0 + a_{12} * 0 * 0 \qquad \text{(F.2)}$$

$y_0 = a_0$

The value of the intercept a_0 is equal to the predicted response at the center of the study domain.

F.3 Interpreting the Coefficient of Factor 1

Consider both points, B and D, which are located at the high level of factor 1, shown in Figure F.1. The coordinates of these points are, in coded units:

$$B \left| \begin{array}{l} x_1 = +1 \\ x_2 = -1 \end{array} \right. , \quad D \left| \begin{array}{l} x_1 = +1 \\ x_2 = +1 \end{array} \right.$$

We can obtain the response at B, denoted y_2, by using corresponding factor levels in their coded units:

$$y_2 = a_0 + a_1 * (+1) + a_2 * (-1) + a_{12} * (+1) * (-1) = a_0 + a_1 - a_2 - a_{12} \qquad \text{(F.3)}$$

Similarly, we can obtain the response at D, denoted by y_4, by using corresponding factor levels in coded units:

$$y_4 = a_0 + a_1 * (+1) + a_2 * (+1) + a_{12} * (+1) * (+1) = a_0 + a_1 + a_2 + a_{12} \qquad \text{(F.4)}$$

Finally, add the two responses y_2 and y_4:

$$y_2 + y_4 = 2 * (a_0 + a_1) \qquad \text{(F.5)}$$

Next, repeat the same calculation for points A and C, the lower levels of the factor 1 where the responses are denoted by y_1 and y_3 respectively. This gives

$$y_1 + y_3 = 2 * (a_0 - a_1) \tag{F.6}$$

Subtracting the second equation from the first one gives

$$4 * a_1 = -y_1 + y_2 - y_3 + y_4 \tag{F.7}$$

which can be written as

$$a_1 = \frac{1}{2} * \left[\frac{y_2 + y_4}{2} - \frac{y_1 + y_3}{2} \right] \tag{F.8}$$

Now note that $\frac{y_2 + y_4}{2}$ is the mean of the responses at the high level of the factor 1. Call this mean $\overline{y_+}$. The expression $\frac{y_1 + y_3}{2}$ is the mean of the responses at the low level of the factor 1, so call it $\overline{y_-}$. For factor 1, write;

$$a_1 = \frac{1}{2} * \left[\overline{y_+} - \overline{y_-} \right] \tag{F.9}$$

The coefficient a_1 is therefore half the difference between the mean of the responses at the high level of the factor 1 and the mean of the responses at the low level of the factor 1.

Changing from the low level to the high level, the response varies, on average, like the difference $\left[\overline{y_+} - \overline{y_-}\right]$. If this difference is large, the response varies a lot. If this difference is small, the response does not vary much. This, therefore, gives us a way to know how the response varies due to factor 1. This is the reason why the coefficient of a_1 is called the factor 1 effect, or the effect of factor 1.

F.4 Interpreting the Coefficient of Factor 2

Using the same reasoning, the coefficient a_2 is equal to the average variation of the response when factor 2 passes from level zero to the high level. It represents the influence of factor 2 in the study domain. This is called "the effect of factor 2."

Generally, when the selected model is a polynomial, the coefficients of the first-degree terms are the effects of the factors.

Knowing the four responses, it is straight forward to calculate the coefficient of a_2:

$$a_2 = \frac{1}{4} * \left[- y_1 - y_2 + y_3 + y_4\right] \tag{F.10}$$

F.5 Interpreting the Coefficient of a_{12}

We calculate the coefficient a_{12} by an analogous method to the one that was used for the coefficients a_1 and a_2. The coefficient a_{12} is found to be equal to

$$a_{12} = \frac{1}{2} * \left[\frac{y_4 - y_3}{2} - \frac{y_2 - y_1}{2}\right] \tag{F.11}$$

However, $\frac{y_4 - y_3}{2}$ is the effect of factor 1 when factor 2 is at its high level. It is half of the variation of the response between y_4 and y_3.

The expression $\frac{y_2 - y_1}{2}$ is the effect of factor 1 when factor 2 is at its low level. It is half of the variation of the response between y_2 and y_1.

The coefficient a_{12} is half of the difference between the two effects. The coefficient a_{12} therefore measures the variation of factor 1 when the level of factor 2 is changed. It can also be shown that the same coefficient (a_{12}) equally measures the variation of the effect of factor 2 when the level of factor 1 is modified in the same way.

The coefficient a_{12} is called the interaction between the factors 1 and 2.

F.6 Transforming Coded Units into Engineering Units

Since the model is in coded units, we must do the calculations in these units and then transform the obtained results into the natural (engineering) units. To use the natural units directly, we need to transform the model in Equation (G.1) itself.

$$x = \frac{A - A_0}{step} \qquad \text{(F.12)}$$

Factor 1

$$x_1 = \frac{A_1 - A_{0,1}}{step_1} \quad \text{(F.13)}$$

Factor 2

$$x_2 = \frac{A_2 - A_{0,2}}{step_2} \quad \text{(F.14)}$$

Where

- $A_{0,1}$ is the average of maximum and minimum of factor 1 in engineering units
- $A_{0,2}$ is the average of maximum and minimum of factor 2 in engineering units
- $Step_1$ is the average of the difference between maximum and minimum of factor 1 in engineering units
- $Step_2$ is the average of the difference between maximum and minimum of factor 2 in engineering units

Therefore, the Equation F.1 becomes

$$y = a_0 + a_1 * (\frac{A_1 - A_{0,1}}{step_1}) + a_2 * (\frac{A_2 - A_{0,2}}{step_2}) + a_{12} * (\frac{A_1 - A_{0,1}}{step_1}) * (\frac{A_2 - A_{0,2}}{step_2}) \quad \text{(F.15)}$$

APPENDIX G

ROUGHNESS MEASUREMENT RESULTS OF 3^3 FULL FACTORIAL DESIGN

Table G.1 Results of Surface Roughness Measurements for Experiment 3

Run	Position (mm)	Feed Rate (mm/min)	Depth of Cut (μm)	Spindle Speed (RPM)	PV (nm)	rms (nm)	R_a (nm)
1	5	12.5	200	5000	2336.5	143.4	87.1
	10				3047.6	100.4	47.7
	15				646.9	31.5	17.2
	Average				2010.3	91.8	50.7
2	5	20	120	2000	4941.4	361.6	244.1
	10				3813.9	299.3	209.3
	15				3791.6	304.2	211.2
	Average				4182.3	321.7	221.5
3	5	12.5	120	5000	1652.0	115.0	82.2
	10				1566.1	100.8	70.3
	15				1139.8	98.1	74.8
	Average				1452.6	104.6	75.8
4	5	20	120	5000	2103.4	150.9	92.5
	10				1655.8	117.4	72.0
	15				1676.6	98.1	58.0
	Average				1812.0	122.1	74.2
5	5	20	40	3500	4114.2	300.0	192.9
	10				2812.9	195.2	127.9
	15				1869.3	156.5	113.7
	Average				2932.1	217.2	144.8
6	5	12.5	40	5000	1494.4	133.2	92.4
	10				1391.6	95.9	64.4
	15				1363.0	99.7	75.6
	Average				1416.3	109.6	77.5

Run	Position (mm)	Feed Rate (mm/min)	Depth of Cut (μm)	Spindle Speed (RPM)	PV (nm)	rms (nm)	R_a (nm)
7	5	5	200	2000	2726.6	166.7	111.8
	10				2657.8	153.2	99.4
	15				2396.2	116.0	80.6
	Average				2593.5	145.3	97.3
8	5	5	40	5000	496.9	27.0	13.6
	10				766.6	27.2	11.1
	15				397.6	16.6	8.0
	Average				553.7	23.6	10.9
9	5	5	200	5000	704.6	34.9	15.9
	10				352.1	12.4	6.0
	15				539.2	11.4	4.5
	Average				532.0	19.6	8.8
10	5	12.5	40	3500	2424.5	171.2	110.6
	10				2743.2	158.0	96.3
	15				2912.3	114.1	70.0
	Average				2693.3	147.7	92.3
11	5	5	120	5000	102.0	4.4	3.2
	10				41.6	3.0	2.3
	15				32.7	2.6	2.0
	Average				58.8	3.3	2.5
12	5	5	200	3500	364.5	12.3	5.9
	10				325.7	9.1	4.0
	15				131.1	3.8	2.4
	Average				273.7	8.4	4.1
13	5	12.5	120	2000	2198.5	132.2	89.0
	10				1329.5	120.4	84.6
	15				1756.9	134.1	90.3
	Average				1761.6	128.9	88.0
14	5	5	40	3500	762.4	34.6	15.5
	10				528.6	19.6	8.8
	15				504.6	16.2	6.5
	Average				598.5	23.5	10.3
15	5	12.5	200	2000	3838.4	184.9	115.9
	10				2497.5	136.0	85.8
	15				1794.6	115.3	80.1
	Average				2710.2	145.4	93.9

Run	Position (mm)	Feed Rate (mm/min)	Depth of Cut (μm)	Spindle Speed (RPM)	PV (nm)	rms (nm)	R_a (nm)
16	5	12.5	40	2000	3258.0	238.8	154.8
	10				2326.5	190.2	121.3
	15				2642.3	214.0	135.3
	Average				2742.3	214.3	137.1
17	5	20	40	2000	4901.8	389.6	266.3
	10				4182.2	327.8	234.2
	15				3218.5	258.5	179.3
	Average				4100.8	325.3	226.6
18	5	5	120	2000	710.7	20.7	11.2
	10				1586.5	35.5	11.5
	15				248.4	9.5	5.8
	Average				848.5	21.9	9.5
19	5	5	40	2000	1172.8	47.7	19.5
	10				1699.1	40.9	14.9
	15				1783.3	64.2	18.6
	Average				1551.8	50.9	17.7
20	5	12.5	120	3500	983.9	41.0	19.8
	10				563.0	26.5	13.1
	15				987.0	36.5	16.8
	Average				844.6	34.7	16.6
21	5	12.5	200	3500	1669.4	53.4	24.8
	10				875.4	30.0	15.1
	15				630.0	29.3	14.9
	Average				1058.3	37.5	18.3
22	5	20	200	5000	2186.4	82.5	48.9
	10				994.1	51.9	34.4
	15				1713.3	57.6	36.8
	Average				1631.3	64.0	40.0
23	5	20	200	2000	4096.4	418.5	314.4
	10				5366.3	422.4	320.9
	15				3142.2	399.3	310.4
	Average				4201.6	413.4	315.2
24	5	5	120	3500	231.5	7.9	5.0
	10				202.8	6.9	4.3
	15				430.5	9.8	4.2
	Average				288.2	8.2	4.5

Run	Position (mm)	Feed Rate (mm/min)	Depth of Cut (μm)	Spindle Speed (RPM)	PV (nm)	rms (nm)	R_a (nm)
25	5	20	200	3500	2319.2	173.4	129.1
	10				1933.5	144.9	107.5
	15				1411.6	118.7	91.8
	Average				1888.1	145.7	109.4
26	5	20	40	5000	1235.1	99.6	74.2
	10				1185.5	81.7	60.6
	15				1620.1	84.9	62.4
	Average				1346.9	88.7	65.7
27	5	20	120	3500	2815.1	168.7	121.6
	10				1649.9	133.6	100.1
	15				1594.1	121.7	93.7
	Average				2019.7	141.3	105.1